
Universidad Nacional Autónoma de México
Posgrado de Astrofísica

# Estudio de modelos extendidos de la gravedad con observaciones del universo tardío

## TESIS

Que para optar por el grado académico de:
Maestro en Ciencias

Presenta:
Rodrigo Sandoval Orozco

**Directora de Tesis:**
Dra. Celia del Carmen Escamilla Rivera
Posgrado de Astrofísica

México, CD. MX., 2023


UNIVERSIDAD NACIONAL AUTÓNOMA DE MÉXICO
POSGRADO DE ASTROFÍSICA

# STUDY OF EXTENDED GRAVITY MODELS WITH LATE-TIME OBSERVATIONS

## DISSERTATION SUBMITTED

FOR THE DEGREE OF
**MASTER IN SCIENCE**

PRESENTED BY:
**RODRIGO SANDOVAL OROZCO**

**SUPERVISOR:**
DR CELIA DEL CARMEN ESCAMILLA RIVERA

MEXICO, MEXICO CITY, 2023

# Agradecimientos


- A Papá y Mamá por su apoyo incondicional independientemente de todo.
- Al Proyecto PAPIIT TA100122 “Confrontación de Observaciones en Cosmología utilizando enfoques de la física fundamental", del cual la Dra. Celia Escamilla Rivera es responsable.
- Al grupo Cosmostatistics National Group (CosmoNag).
- A la Dra. Celia Escamilla Rivera del ICN UNAM
- A Juan Luciano Díaz Gónzalez, de la Unidad de Cómputo del ICN UNAM.

# Artículos realizados durante este trabajo de tesis:

- **R. Sandoval-Orozco**, C. Escamilla-Rivera, R. Briffa and J. Levi Said. *$f(T)$ cosmology in the regime of quasar observations*. 2023. arXiv:2309.03675. Accepted to Physics of the Dark Universe 43 (2024) 101407. *[Main paper].*

- P. Maldonado Alonso, C. Escamilla-Rivera, **R. Sandoval-Orozco**. *Constraining dark energy cosmologies with spatial curvature using Supernovae JWST forecasting*. 2023. arXiv:2309.12292. Submitted to Journal of Cosmology and Astroparticle Physics.

# Contents

# Resumen

El modelo cosmológico estándar ΛCDM es un modelo robusto que permite ajustar grupos de datos cosmológicos de manera precisa que además destaca por su simpleza. Este modelo se compone de la Relatividad General, la hipótesis de homogeneidad e isotropía además de la necesidad de introducir los componentes de *materia oscura* (que nos permite corregir el comportamiento de la gravedad a grandes escalas) y la *energía oscura* (que nos permite explicar la expansión acelerada del universo). Sin embargo, en años recientes el paradigma de dicho modelo se encuentra en constante cuestionamiento. Esto debido a los problemas relacionados con la naturaleza del mencionado *sector oscuro* del que no tenemos confirmación directa, y por la creciente tensión en la determinación de la constante de Hubble $H_0$ que parece tener dos valores diferentes dependiendo de la forma en que sea medido. Estos y otros problemas han abierto la posibilidad a mejoras o generalizaciones al modelo ΛCDM, ya sea usando nuevos grupos de datos (como son los cuasares) o extensiones de la gravedad como candidatos para resolver los mencionados problemas cosmológicos. En este trabajo se analizarán dos muestras de Quasares utilizadas para medir distancias en cosmología que nos permitan realizar constricciones de parámetros de modelos extendidos de la gravedad. La extensión de la gravedad utilizará diferentes modelos $f(T)$ en los cuales la interacción de la gravedad no es la curvatura como en Relatividad General, sino la torsión; que además permiten explicar un universo sin recurrir a la energía oscura para explicar la expansión acelerada. Con estos modelos se encontró, además, que usar datos como cuasares con estos modelos $f(T)$ se puede reducir la tensión de $H_0$.

# Abstract

The ΛCDM standard cosmological model is a robust framework that allows for a highly precise adjustment of the current cosmological datasets and is noteworthy for its simplicity. This model consists of General Relativity, the assumption of homogeneity and isotropy, and the necessity to introduce components of *dark matter* (enabling the correction of gravity's behavior on large scales) and *dark energy* (explaining the late-time accelerated expansion of the universe). However, in recent years, the paradigm of this model has been under constant scrutiny. This is due to issues related to the nature of the mentioned *dark sector*, which lacks direct confirmation, and the growing tension in determining the Hubble constant $H_0$, seemingly having two clear different values depending on the measurement method. These and other problems have opened the possibility for improvements or generalizations to the ΛCDM model, whether by using new datasets (such as Quasars) or extension of the gravity theory that could address the mentioned cosmological issues.

This work analyzes two samples of Quasars used to measure distances in cosmology, allowing for constraints on parameters of extended gravity models. The extension of the gravity used involves different $f(T)$ models where gravity's interaction is based on torsion rather than curvature as in General Relativity. Moreover, these models can explain a universe without resorting to dark energy to account for accelerated expansion. It was found that using Quasar data with these $f(T)$ models can alleviate the tension in $H_0$.

# Introduction

The diminution of the expected brightness coming from the Supernovae Ia (SNIa) was crucial for testing the accelerating universe in 1998 (Riess et al., 1998). We now have more evidence of this acceleration through different late data sets. The cosmological constant $\Lambda$ appears to be the simplest explanation for this phenomenon as we only need to use a fluid with negative pressure in the standard model of cosmology, or so-called $\Lambda$CDM, where $\Lambda$ refers to this constant and CDM means Cold Dark Matter. The $\Lambda$CDM model has been successful in explaining not only the late-time cosmic acceleration but the power spectrum of the Cosmic Microwave Background (CMB) radiation (Aghanim et al., 2020b), and the statistics of the large scale structure (Zhao et al., 2019). The model's success is not only based on the predictive accomplishments but also due to the simple assumptions, including the descriptions of the contents of the universe, and the assumptions of cosmological principle (Perivolaropoulos and Skara, 2022).

But $\Lambda$CDM is not free of issues including the growing difference between the cosmological and astrophysical data in the estimation of the Hubble parameter at current times $H_0$ (the measurement of the present expansion rate of the Universe and it is the basic quantity to infer other cosmological quantities (Riess and Breuval, 2023)) determined using different probes. Other issues of the $\Lambda$CDM model are the ones related to the small scale of the universe, as the missing satellite problem or the baryonic Tully-Fisher relation problem (Perivolaropoulos and Skara, 2022).

Using a distance ladder approach, in which we rely on distance estimators using geometry via parallax and then standard candles like Cepheids and SNIa -which are objects that the luminosity is known independently from the distance- (that is known as late or low redshift), the measurements of $H_0$ are higher than the ones obtained using the CMB using the standard model (known as early or high redshift measurements) in $\sim 5\sigma$ difference. This could be a hint that something in the cosmological model is not working properly as this could be a hint that a revision of the systematics or in the gravitational theory itself needs to be done. In a lesser, the clustering of matter measured by the quantity $S_8 = \sigma_8\sqrt{\Omega_m/0.3}$ has a discrepancy between the measurements from the CMB data with $\Lambda$CDM and the ones measured using statistical techniques with the galaxy distribution in the universe (Abdalla et al., 2022; Philcox and Ivanov, 2022).

One of the proposed solutions for the $H_0$ and $\sigma_8$ tensions is to explain the missing parts of $\Lambda$CDM as a problem in our understanding of gravity leading to an estimate of $H_0$ with Planck larger and therefore, reconciling with the estimates obtained with late time probes (as SNIa) or vice versa, lowering the estimate with low $z$ data sets (Abdalla et al., 2022). However, this is not the only way to attempt a solution to the cosmological tension problems as the modifications or generalizations from the standard $\Lambda$CDM models are not straightforward, which leads us to a degeneracy of the models.

The different proposals to alleviate the cosmological tensions have to take into account both $H_0$

and $S_8$ values, and the observational properties of the cosmic expansion, the growth properties of the Baryonic Acoustic Oscillations (BAO) galaxy power spectrum (Alam et al., 2017), and the void measurements (Contarini et al., 2022), in addition to the already covered local late-time data using the ΛCDM model. Nevertheless, the choice of observational data is crucial to the analysis since the CMB cosmological probes to estimate standard rules sometimes assume the ΛCDM model in the background.

This dependence in some probes on the standard model makes us select three basic cosmological data sets to conform to the *baseline*: The $H(z)$ measurements (or Cosmic Chronometers) (Moresco et al., 2016) that are a direct and model-independent estimation of the Hubble parameter. With this observable, we can use the relation between the scale factor $a(t)$ and the redshift in the homogeneity assumption by measuring the differential age in galaxies, that have extremely homogeneous populations and evolve without being disturbed by interactions, and the differential redshift between them to obtain $H(z)$ (Moresco et al., 2018). Furthermore the SNIa Pantheon compilation that consists of 1049 SNIa data points calibrated using the cosmic ladder via parallax and Cepheid period determination. With this technique we estimate the distance to the supernovae that occur in galaxies where we have already observed Cepheids (Scolnic et al., 2018). Also, we used BAO that are measurement of the three-dimensional distribution of the galaxies influenced by the pattern imprinted in the early universe. These measurements come from four different surveys: Beutler et al. (2011), Jones et al. (2009), Ross et al. (2015) and Alam et al. (2017). As part of these local measurements, high-redshift observables have been used to analyze deviations from the standard cosmological model. On this attempt, it has been considering complementary distance measurements using two different Quasar samples: the xA sample (Negrete et al., 2018) and the nUVX sample (Lusso et al., 2020). On one hand the xA sample is based on the 4DE1 formalism to locate $\sim$ 250 extreme accretors, or the AGNs with the highest accretion rates. These objects could be considered standard candles using the Eddington Luminosity (which is the luminosity at which these objects could emit light) and, therefore, bring extra information to the SNIa trend (Dultzin et al., 2020).

On the other hand, the nUVX sample is based on the empirical relation between the UV and X-ray emission of $\sim$ 2500 Quasars fitted through different redshifts to obtain a relation that could allow us to determine their distance in a model-independent manner (Lusso et al., 2020). As the two Quasar samples have different formalisms, this work will be analyzed separately for the selected models along with the *baseline* data sets.

From the theoretical point of view, modifications to the first principles of the theory of gravity have been gaining popularity in literature. These modifications promise to alleviate the Hubble tension, find the dark matter's nature, and explain the late-cosmic acceleration without dark energy (Di Valentino et al., 2021a). To modify the GR formalism, we must take into account the *Lovelock theorem*. This theorem limits how many theories we can construct using the metric tensor only, as GR is the field involved in the gravitational action. So, the only possible four-dimensional gravitational theory involving the metric tensor and its derivatives will construct field equations that are second-order or less (Clifton et al., 2012). Lovelock's theorem offers us options to construct the theories of gravity, working on Riemannian geometry, that differ from general relativity: *(i)* Other fields instead of the metric tensor, *(ii)* higher order derivatives in the theory, *(iii)* extra dimensions allowed and *(iv)* give up symmetry, locality and divergence-free conditions in the theory (Clifton et al., 2012).

The modified theories of gravity could help in the alleviation of the aforementioned Hubble

tension. Using the example of $f(\mathcal{R})$ theory in which the curvature scalar $\mathring{\mathcal{R}}$ that appears linearly in GR is substituted by a general function to attempt to solve the astrophysical and cosmological issues with ΛCDM. In cosmology, the use of early-time data could raise the value of the $H_0$ constant to values equivalent to the late-time measurements (Di Valentino et al., 2021a). In astrophysics, the $f(\mathcal{R})$ formalism results in a representation of the galactic rotation curves without the introduction of dark matter (Capozziello and De Laurentis, 2011). On the contrary, the disadvantage of using the $f(\mathcal{R})$ theories is that the field equations are in fourth order and, therefore, more complicated than those of GR.

As there is no reason why the curvature scalar result of the Levi-Civita connection $\mathring{\mathcal{R}}$ appears lineally in the theory, there is no reason why the curvature is the interaction mediator in gravity. To have a control on the degeneracy of cosmological models that could arise from first principles in an extension of theories of gravity, in this thesis, we will use the Teleparallel Equivalent Theory of Gravity (TEGR), more specifically a group of $f(T)$ theories in which the curvature scalar $\mathring{\mathcal{R}}$ in the Einstein field equations is replaced by a function of the torsion scalar $T$. This TEGR has the advantage of leaving the field equations in second order in the field equations. This means that in this framework the torsion embraces torsion as the mediator of the gravitational interaction (Abdalla et al., 2022; Di Valentino et al., 2021a) In current times, Teleparallel Gravity (TG) has started to appear in several cosmological and astrophysical analyses, in particular regarding possible solutions to solve or relax the $H_0$ tension. The motivation is a consequence of first principles, where modifications of gravity can explain the late time acceleration using torsion geometries instead of curvature like in General Relativity (GR) description of gravity using a different mathematical element so-called teleparallel connection, in which the Levi-Civita connection is substituted for a space-time curvature-free but with the Weitzenböck connection (Bahamonde et al., 2021) induces torsion results in an equivalent system of differential equations compared to GR (Abdalla et al., 2022). This theory is known as the TEGR. The models derived from this TEGR description leads to an alternative explanation for the late time cosmic acceleration (Bengochea and Ferraro, 2009) and is one of the candidates for lowering the difference between the measurements of $H_0$

This thesis is divided as follows: In Chapter 1 we introduce a general overview of General Relativity and the standard cosmology (1.1). We describe the cosmological quantities involved in the theory and give an overview of the cosmological tensions (1.1.2). By the end of the Chapter, we described the extensions and modifications of gravity theories (1.2,1.3) most discussed in the literature In Chapter 2 the Cosmology using the TEGR is presented along the cosmological viable models for $f(T)$. In Chapter 3 we describe the data sets employed in this work to constrain the cosmological parameters for the $f(T)$ models described Additionally, we include the two Quasar samples. We remark that this analysis has not been treated in the literature so far. The results are part of an original work (Sandoval-Orozco et al., 2023). In Chapter 4 we present the results using the different combinations of the observational data sets. On one hand, we consider the combinations of $H(z)$, SNIa, and separately the two Quasar samples to differentiate the observational methods. On the other hand, we consider the use of BAO measurements to separate the data with ΛCDM dependency. Finally, in Chapter 5 we will point out the most remarkable achievements of having introduced these Quasar samples. Also, we describe the proper mechanism to increase the $H_0$ value in these models without arising systematics issues in the baselines considered. Appendix A includes some extra comments regarding the use of the $H(z)$ measurements covariance matrix. The aim of introducing this matrix is because previously estimated errors for these measurements did not consider the systematics in the age determination of the galaxies (Moresco et al., 2020).

# Chapter 1

# Foundations of Teleparallel Gravity and Cosmology

## 1.1 An overview on General Relativity and its symmetries

General Relativity (GR) is a theory based on the principle that space and time constitute a single structure based on the mathematical principle of Riemann's manifolds (Cai et al., 2016). In this scheme, the GR reproduces the Minkowski geometry in the absence of the influence from massive objects, thus referring to gravity as a geometric consequence of the mass, specifically, the curvature. In the framework of GR, the dynamical behavior of the different systems is imposed by the metric choice $g_{\mu\nu}$ that induces the causal structure and a non-trivial geometric structure of the space-time Additionally, the Levi-Civita connection $\mathring{\Gamma}^{\mu}{}_{\nu\rho}$ defines the geodesic structure (Cai et al., 2016) of space-time. This is the instrument of gravity that the metric quantifies and the quantities related to the metric are the dynamical elements (Hohmann, 2022; Misner et al., 2017). Notice that this is a fundamental difference between the electromagnetic, weak, and strong interactions that currently are described by transformations taking place in space, but themselves are unrelated to the structure of the space in which the transformation takes place (Aldrovandi and Pereira, 2013).

The Levi-Civita derived quantities will be written with a circle on top, meaning that the coefficients can be written as:

$$\mathring{\Gamma}^{\mu}{}_{\nu\rho} = \frac{1}{2}g^{\mu\sigma}(\partial_{\nu}g_{\sigma\rho} + \partial_{\rho}g_{\sigma\nu} - \partial_{\sigma}g_{\nu\rho}), \tag{1.1}$$

which is an important element of the theory, as the metric $g_{\mu\nu}$ is the fundamental element in the GR description of space-time. In this context, the Greek letters $\mu, \nu, \rho, \lambda = 0, 1, 2, 3$ are the space-time coordinates. As we can notice, the connection $\mathring{\Gamma}^{\mu}{}_{\nu\rho}$ is derived from only the metric and, therefore, it determines the causal structure and the geodesic structure. Therefore, space-time is a Riemannian manifold associated with the metric and it is known as a *Metric Affine* formulation of gravity (Cai et al., 2016). Using this connection we can obtain the curvature tensor as (Weinberg, 2008)

$$\mathring{\mathcal{R}}^{\mu}_{\nu\rho\sigma} = \partial_{\rho}\mathring{\Gamma}^{\mu}_{\nu\sigma} - \partial_{\sigma}\mathring{\Gamma}^{\mu}_{\nu\rho} + \mathring{\Gamma}^{\mu}_{\tau\rho}\mathring{\Gamma}^{\tau}_{\nu\sigma} - \mathring{\Gamma}^{\mu}_{\tau\sigma}\mathring{\Gamma}^{\tau}_{\nu\rho}, \tag{1.2}$$

and from the contractions from the latter, we can obtain the Ricci tensor as

$$\mathring{\mathcal{R}}_{\mu\nu} = \mathring{\mathcal{R}}^{\alpha}{}_{\mu\alpha\nu}, \tag{1.3}$$

where the repeated indices represent a sum. The scalar curvature can be represented as

$$\mathring{\mathcal{R}} = g^{\mu\nu}\mathring{\mathcal{R}}_{\mu\nu}. \tag{1.4}$$

This means that we can rewrite the field equations using the symmetries of the curvature tensors using

$$\mathring{\mathcal{R}}_{\mu\nu} - \frac{1}{2}g_{\mu\nu}\mathring{\mathcal{R}} = \kappa^2\mathring{\mathcal{T}}_{\mu\nu}. \tag{1.5}$$

Seeing the previous equations, notice that for the geometrical part of the field equations, the connection fulfills the role of being the information about the curvature in the description of space-time and, therefore, gravity. Finally, to obtain the field equations we need to present the Einstein-Hilbert action

$$\mathcal{S}_{\text{EH}} = \frac{1}{2\kappa^2}\int \mathrm{d}^4x\sqrt{-g}\mathring{\mathcal{R}} + \frac{1}{2\kappa^2}\int \mathrm{d}^4x\sqrt{-g}\mathcal{L}_m, \tag{1.6}$$

where $\mathcal{L}_m$ is the Lagrangian matter and it is a linear equation for the curvature scalar $\mathring{\mathcal{R}}$. The energy-momentum tensor will be defined, in fact, with respect to the Lagrangian density for the matter fields as

$$\mathcal{T}_{\mu\nu} = \frac{-2}{\sqrt{-g}}\frac{\delta\mathcal{L}_m}{\delta g_{\mu\nu}}. \tag{1.7}$$

Varying the action presented in Eq. (1.6) with respect to the metric tensor $g_{\mu\nu}$ we can obtain the Einstein field equations that can be written as

$$\mathring{G}_{\mu\nu} = \kappa^2\mathcal{T}_{\mu\nu}, \tag{1.8}$$

where $\mathring{G}_{\mu\nu} = \mathring{\mathcal{R}}_{\mu\nu} - \frac{1}{2}g_{\mu\nu}\mathring{\mathcal{R}}$ is known as the Einstein tensor and $\kappa^2 = 8\pi G$, where $G$ is the gravitational constant.

In GR the metric tensor $\mathring{\mathcal{R}}^{\mu}_{\alpha\nu\beta}$ acts as a mere container of information from the Levi-Civita connection and only quantifies the amount of geometric deformation (Briffa et al., 2022). This approach has been extremely useful through the different experimental tests in specific systems as the gravitational waves (Abbott et al., 2017b), the shift of the Mercury perihelion (Shankaranarayanan and Johnson, 2022) and the direct evidence of black holes (Wielgus et al., 2020); among other different experiments. This does not mean that GR is the ultimate description of gravity, as more recently several problems have arisen from this framework (Di Valentino et al., 2021c), and some of the propositions to solve these problems are through a new description or generalization of the physics.

- **Schwarzschild symmetry.** GR has been useful to describe the phenomena in the Universe and the cosmos itself. However, some symmetries need to be considered to describe them. On one hand, to study this theory at the astrophysical level the first solution is the Schwarzschild metric. The geometry of spherical, static geometry is described as

$$\mathrm{d}s^2 = \left(1 - \frac{2M}{r}\right)\mathrm{d}t^2 - \left(1 - \frac{2M}{r}\right)^{-1}\mathrm{d}r^2 - r^2\mathrm{d}\theta^2 - r^2\sin^2(\theta)\mathrm{d}\phi^2, \tag{1.9}$$

  where $r, \theta, \phi$ is the description of the space in spherical coordinates and $M$ is the mass of the system, making it a metric spherically symmetric. It is important to note that this system

behaves badly as $r \to 0$ and it is called *Schwarzschild radius*. This radius is associated with the event horizon of a non-rotating black hole (Misner et al., 2017). The Schwarzschild geometry is useful also for calculations like time dilation, and gravitational redshift and because of its spherical symmetry is useful to describe stars and massive systems like neutron stars.

In astrophysical scales, we need only baryons to describe the stars and the black holes, the problem arises when we analyze other systems. We refer as *baryons* to ordinary matter composed by nuclei and electrons (Baumann, 2022). Turns out that is not the only form of matter that is needed to describe the behavior of the universe, as most of the predicted matter of the universe is in the form of *dark matter*. One of the most direct observations of this kind of matter is the measured rotation speed of the objects in galaxies. Instead of this velocity experimenting a diminution as the distance from the center of the galaxy grows as expected in GR, the speed star constant far beyond the extent of the visible disk (Baumann, 2022). This is one of the suggestions that there is an invisible content of matter holding the galaxy together. In bigger scales, it has been detected by gravitational lensing (Jones, 2017) and the statistical effects on the photons of the CMB (Arbey and Mahmoudi, 2021).

From the particle physics perspective, the Standard Model of particle physics does not provide a candidate for cold dark matter as it requires to be massive, weekly interacting, and stable over several billions of years (Arbey and Mahmoudi, 2021). This rules several families of particles. In this direction, propositions like ALPS (Axion-like particles) could be a candidate as the interaction with the rest of the Standard Model particles is negligible and could be generated via the decay of primordial scalar fields. The detection of all light particles is not possible yet, because the interaction would be too tiny and all the efforts are focused on the detection of variations of the electric field (Arbey and Mahmoudi, 2021).

From a theoretical point of view, modifications, and extensions of the GR framework have been proposed. We will talk further but the $f(\mathcal{R})$ formalism is one of the candidates to replace the necessity for dark matter in astrophysical systems (Capozziello and De Laurentis, 2011; Mendoza et al., 2011).

We have been searching for the nature of this dark matter without results, yet. On all scales, the model resumes as *cold dark matter* as it refers to the same pressureless fluid that we have not detected directly.

- **Cosmological Principle symmetry.**

  On the other hand, at cosmological scales, the Cosmological Principle has been useful to describe the universe and its current evolution. This Principle is introduced in the GR formalism through the Friedmann-Lemaître-Robertson-Walker metric. The FLRW spatially flat metric can be represented as (Baumann, 2022)

$$\mathrm{d}s^2 = \mathrm{d}t^2 - \frac{a^2(t)}{1-kr^2}\mathrm{d}r^2 - a^2(t)r^2\mathrm{d}\theta^2 - a^2(t)r^2\sin^2(\theta)\mathrm{d}\phi^2, \tag{1.10}$$

  where $a(t)$ is the scale factor. This solution to the field equations describes an expanding universe quantified precisely in the scale factor $a(t)$. The curvature parameter $k$ describes the geometry of the universe, where if $k = 0$ the universe is flat. If $k = 1$ it is positively

curved and if $k = -1$ it is negatively curved (Schutz, 2009). In this Thesis, we will use only the flat metric with $k = 0$. The metric fulfills the isotropic and homogeneity restrictions as no matter where an observer stands on a three-surface, it will look the same in all directions (Schutz, 2009).

The standard scenario in cosmology is based on the cosmological principle in which the isotropy and homogeneity of the universe at large scales are supported by the CMB observations (Aghanim et al., 2020b). In current times, we realize that matter and radiation are not enough to describe the evolution of the universe since the discovery of the late-time cosmic acceleration (Riess et al., 1998). The source of this acceleration is called *dark energy* and it is distinguished from matter and radiation because it has a negative pressure that counteracts the gravitational force (Amendola and Tsujikawa, 2010). This dark energy is constant in time and the simplest candidate for this is the so-called cosmological constant $\Lambda$.

This energy could be related to the *vacuum* energy predicted by the quantum field theory (Baumann, 2022) but the predictions of the size of this energy are much smaller than the value inferred from cosmological observations in about $10^{121}$ times (Amendola and Tsujikawa, 2010). In this cosmological scale, the search for the nature of the *dark energy* is focused on the parametrization about its origin and the $\Lambda$ vanishes. In general, there are two approaches to the construction of dark energy. The first one includes the *modified matter* models in which the energy-momentum tensor $\mathcal{T}_{\mu\nu}$ contains an exotic matter source with negative pressure. The second one is focused on modifying the geometric part of the field equations (1.8) (Amendola and Tsujikawa, 2010). Examples of the energy-momentum tensor modifications are the Quintessence scalar fields that explain inflation and dark energy (Tsujikawa, 2013) and parametrizations of the fluid like the one proposed by Chevallier and Polarski (2001). Regarding the modifications on the geometry, propositions like $f(T)$ (Abdalla et al., 2022) and $f(\mathcal{R})$ (Capozziello and De Laurentis, 2011) are examples of this approach.

In summary, the description of the universe from the astrophysical level to the cosmological framework needs at least several components:

1. Cosmological principle that induces homogeneity and isotropy.
2. The introduction of dark matter to explain the astrophysical necessities such as the galactic rotation curves, the gravitational lensing and the CMB physics.
3. The use of dark energy to explain the late-time cosmic acceleration.

The final piece of the cosmological model is the introduction of a primordial phase of cosmic inflation to address the horizon and flatness problems of the CMB radiation (Guth, 1981). During this period the fluctuations in the matter distribution are produced by quantum fluctuation in the early universe (Perivolaropoulos and Skara, 2022). All of these elements form the $\Lambda$CDM model of cosmology.

### 1.1.1 Standard Cosmology: the evolution equations

Since the field equations are a group of differential equations, we are required to describe in them the gravitational interactions and the metric as a consequence of the space-time. Therefore, in GR we need to use a specific description of the framework to describe the physical phenomena

involved. In the case of Cosmology, the spatially isotropic and homogeneous FLRW is used as a metric to rewrite the set of field equations onto the special case ones: the Friedmann equations

$$H^2 = \left(\frac{\dot{a}}{a}\right)^2 = \frac{8\pi G}{3}\rho, \tag{1.11}$$

$$\frac{\ddot{a}}{a} = -\frac{4\pi G}{3}(\rho + 3p). \tag{1.12}$$

In these equations, $\rho$ is the total energy density and $p$ is the pressure of the perfect fluid needed for the construction of the previous formalism. The explicit form of the tensor to form a perfect fluid is:

$$\mathcal{T}_{\mu\nu} = (\rho + p)u_\mu u_\nu + p g_{\mu\nu}, \tag{1.13}$$

where $u_\mu$ is the four-velocity. This form of the vector also fulfills the requirements of the cosmological principle as isotropy requires that the mean value of the three-vector $u^i$ vanish and homogeneity requires that the mean value of a three-scalar is only a function of time (Baumann, 2022).

Additionally, the Hubble parameter $H$ is defined as $H \equiv \dot{a}/a$, where the dot denotes derivatives with respect to the cosmic time $t$.

The scale factor $a(t)$ is a function of the cosmic time $t$ where $a(t_0) = a_0 = 1$, where $t_0$ is the present time. Also, the redshift can be defined as $z \equiv a_0/a - 1$, which can be used as a reference to the age or scale of the Universe indistinctly. In the case of the Hubble factor, at current times is defined as $H(t_0) = H_0$, also known as the current Hubble constant. By using the conservation equation $\mathring{\nabla}_\mu \mathcal{T}_{\mu\nu} = 0$ or the derivative with respect to time of the first equation (1.11), we can arrive at the last of the set of Friedmann equations

$$\dot{\rho} + 3\frac{\dot{a}}{a}\rho(1 + w_i) = 0, \tag{1.14}$$

where $w_i$ defined as the Equation-of-State (EoS) when we consider $\mathcal{T}_{\mu\nu}$ as a perfect fluid with components $i$'s. Under this assumption, $p = w_i\rho$, with $w = 0$ denoting matter contributions and $w = 1/3$ denoting radiation. Other cases consider $w = -1$, which denotes a fluid with negative pressure usually associated with the aforementioned cosmological constant $\Lambda$ or an unknown vacuum energy. Defining the critical density as $\rho_{\text{crit}} = 3H_0^2/8\pi G$ (Dodelson, 2002) we can rewrite the first Friedmann equation (1.11) as

$$E^2(z) = \left(\frac{H(z)}{H_0}\right)^2 = \Omega_m(1 + z)^3 + \Omega_r(1 + z)^4 + \Omega_{\text{DE}}, \tag{1.15}$$

where DE denotes Dark Energy. It is important to note that the energy densities are evaluated in current times as $z = 0$. Also, the power expression for the $(1 + z)$ part represents the volumetric expansion for the matter density and additionally the Doppler shift in case of the radiation component. This equation gives the standard cosmological evolution for a flat FLRW space-time in GR. However, while this evolution has been well tested with current observables (Baumann, 2022), there are some issues related to that involve a modification of the standard model of particles to maintain GR as the main framework, by proposing the existence of the *cold dark matter* (CDM) (Di Valentino et al., 2021c) as a particle(s). Moreover, the test of the accelerating universe

(Riess et al., 1998) led to the introduction of another element that is responsible for this effect, the so-called *dark energy*, which is commonly related to $\Lambda$. So far, we have not a unique answer to what can be or which measured component is this dark energy. Combining both dark components, known as the *dark sector*, gives rise to the standard cosmological model $\Lambda$CDM, where the cold dark matter acts on gravitational scales in the GR framework, while the $\Lambda$ is responsible for the cosmological scales interactions and responsible for the cosmic acceleration.

So, $\Lambda$CDM is a well-defined, predictive, and simple cosmological model that has a remarkable success in explaining most of the properties and dynamics of almost all datasets, including the late-time cosmic acceleration (Riess et al., 1998), the power spectrum of the CMB (Aghanim et al., 2020b), the statistical properties of the large scale structure of the universe (Alam et al., 2017) and the observed abundances of different types of elements (Perivolaropoulos and Skara, 2022; Cyburt et al., 2016). The simplicity of the model relies on six base parameters that include the linear perturbations and the homogeneous and isotropic background that cover the aforementioned wide range of cosmological observations (Abdalla et al., 2022).

As $\Lambda$CDM describes well the observational evidence, both the dark matter and dark energy have been questioned as consistency problems arise. We have an important lack of direct detection of the dark matter from the particle perspective and the dark energy formalism is still missing the description of the nature of the late-time cosmic acceleration (Abdalla et al., 2022).

### 1.1.2 On the cosmological tensions

Although GR, and its cosmological-derived model $\Lambda$CDM, can reproduce the current cosmological data sets, we still need to find an explanation for the nature of the dark sector and explain the current cosmological tensions. On average, from available data, the dark energy component is around 70% ($\Omega_\Lambda \approx 0.7$) of the total density of the universe (Aghanim et al., 2020b; Magaña et al., 2018; Riess et al., 2021b; Zhao et al., 2019), and the matter component is around $\Omega_m \approx 0.3$ ($\Omega_b \approx 0.05$) (Aghanim et al., 2020b). These values suggest that only 5% of the universe interacts with baryonic matter via electromagnetic force, and we have not found a unique answer to the nature or the origin of these dark components, yet.

Moreover, the $\Lambda$CDM model, and therefore GR, needs an additional element to explain the evolution of the universe at early stages: *Inflation* (Guth, 1981). This proposition is made to solve the issues regarding the flatness problem and the horizon problem. The observational confirmation of this scenario is still missing as we lack the direct detection using the polarization of the CMB radiation (Kamionkowski and Kovetz, 2016).

Regarding the current cosmic acceleration observed, the dark energy component needs to be identified with a negative pressure EoS $\rho = -p$ (Abdalla et al., 2022), even though its nature per se is still unknown. However, aligned to this issue, dark energy does not explain why the observed value of its related constant $\Lambda$ is 120 orders of magnitude lower compared to the value of the vacuum energy density derived from Particle Physics (Faraoni and Capozziello, 2011).

While the latter issues are still at hand, the standard cosmological model suffers from another problem: statistical tensions in observable parameters. *Tension* is a statistical term used to describe results that appear to be in discrepancy when catalogs from different surveys are employed (Escamilla-Rivera et al., 2011). Currently, in cosmology, we have groups of data in which tension is present. The most remarkable discrepancies come when a comparison between the Planck Satellite measurements of the Cosmic Microwave Background (CMB) (Aghanim et al., 2020b) and the low

redshift probes as the Supernovae $H_0$ Equation State project (SH0ES) (Riess et al., 2022) is done in the calibration of two cosmological parameters: the expansion rate measured through the Hubble constant $H_0$, and the degree of clustering of matter $\sigma_8$ or $S_8$. And, if these discrepancies do not come from systematic errors they could be an indication of a failure in our current standard model $\Lambda$CDM. Is important to mention that these tensions could suggest deviations from a flat universe (Di Valentino et al., 2021b).

We can divide the analysis of cosmological tension into two:

1. **Early measurements (inferred).** We consider *early* measurements of the expansion rate $H_0$ those corresponding to the $z > 1100$, in which we need several assumptions about the neutrinos, particle interactions, and magnetic fields; to mention some of them (Di Valentino et al., 2021a). In this scheme, an expansion history is needed to reconstruct the evolution of the scale parameter to constrain $H_0$ (Bernal et al., 2016). In this context, CMB experiments obtain different values for the expansion rate $H_0$. The most cited late value for $H_0$ is the result from the CMB Planck Collaboration using a $\Lambda$CDM flat universe with $H_0 = 67.36 \pm 0.54$ km s$^{-1}$ Mpc$^{-1}$, including lensing effects (Aghanim et al., 2020b). Other CMB probes give results with somehow less tension, but also with very large uncertainties such as the Atacama Cosmology Telescope (ACT) using the same flat $\Lambda$CDM which obtains $H_0 = 67.9 \pm 1.5$ km s$^{-1}$ Mpc$^{-1}$ (Aiola et al., 2020). The result from the Wilkinson Microwave Anisotropy Probe (WMAP) with $H_0 = 70.2 \pm 2.2$ km s$^{-1}$ Mpc$^{-1}$ (Bennett et al., 2013). The Atacama Cosmology Polarimeter (ACTPol) that obtains $H_0 = 69.72 \pm 1.63$ km s$^{-1}$ Mpc$^{-1}$ (Wang and Huang, 2020), among others that use the same kind of calibration involving an analysis of the power spectrum from the CMB temperature, electric field and if it is possible with polarization. Other examples of early time measurements are the BAO that constrains the product of the sound horizon $r_s$ and the Hubble constant together, estimating $H_0$ dependent on the abundance estimates and the physics of the early universe. The Baryon Acoustic Oscillation Spectroscopic Survey (BOSS) Data Release 12 (DR12) in which the measurement of clustering in galaxies gives a result of $H_0 = 67.9 \pm 1.1$ km s$^{-1}$ Mpc$^{-1}$ (Ivanov et al., 2020). The most recent results in this field are given by the extended BOSS (eBOSS) DR16 data measurements in which $H_0$ is constrained using a priori on $\Omega_m h^2$ as $H_0 = 69.6 \pm 1.8$ km s$^{-1}$ Mpc$^{-1}$(Alam et al., 2021), and the result combining the eBOSS data, the 6-degree Field Galaxy Survey (6dFGS) and the WMAP data obtaining $H_0 = 68.36^{+3.0}_{-5.5}$ km s$^{-1}$ Mpc$^{-1}$ (Zhang and Huang, 2019).

2. **Late measurements (measured).** *Late* measurements are those related to several methods that rely on local measurements of $H_0$ usually employing our capacity to measure progressively bigger distances using different methods, from geometrical in parallax (see for example Vallenari et al. (2022)) to the luminosity and calibration dependent as SNIa (Riess et al., 2021b). Precisely, this approach is used for measuring the pulsating Cepheids in our galaxy to calibrate the SNIa visible to great distances due to its great visibility. Furthermore, these methods can be used to measure the cosmic expansion. The *standard candles* method employs the same luminosity without reference to stellar reference or astrophysics theory (Di Valentino et al., 2021a). The Supernovae $H_0$ Equation of State (SH0ES) project measured uses this method of distance ladder via the Cepheid stars to obtain a value of $H_0 = 73.3 \pm 1.04$ km s$^{-1}$ Mpc$^{-1}$ (Riess et al., 2021b). The value obtained by Early Data Release 3 (ERD3) from Gaia Space Telescope that measured Cepheids results in $H_0 = 74.03 \pm 1.42$ km s$^{-1}$

Mpc$^{-1}$ (Riess et al., 2021a). The measured Cepheids in infrared from the Spitzer Space Telescope conducted by the Carnegie Hubble Program, which is in concordance with other Cepheid measurements, reports $H_0 = 74.3 \pm 2.2$ km s$^{-1}$ Mpc$^{-1}$ (Freedman et al., 2012). We must mention that Cepheids are not the only stars to calibrate the distance ladder and substitutes have been proposed such as the Tip of the Red Giant Branch (TRGB) calibrating $H_0 = 69.8 \pm 0.8$ km s$^{-1}$ Mpc$^{-1}$ (Freedman et al., 2020), the variable red giant stars MIRAS that measured $H_0 = 73.3 \pm 4.0$ km s$^{-1}$ Mpc$^{-1}$ (Huang et al., 2019), and the Tully-Fisher relation (between the rotation rate of spiral galaxies and their absolute luminosity) that found $H_0 = 76.0 \pm 1.1(\text{stat}) \pm 2.2(\text{sys})$ km s$^{-1}$ Mpc$^{-1}$ (Kourkchi et al., 2020). Other forms to determine the Hubble constant via astrophysical methods are the $H_0$ Lenses in COSMOGRAIL's Wellspring (H0LICOW) project that measures $H_0$ through the analysis of different images from the same distant quasar measuring the time-delay path of the light in strong gravitational lensing with $H_0 = 71.9^{+2.4}_{-3.0}$ km s$^{-1}$ Mpc$^{-1}$ (Suyu et al., 2017). Furthermore, the combination between the information contained in electromagnetic and gravitational waves (called *dark standard sirens*) to estimate the luminosity distance to highly energetic events like the GW170817 that constraint the Hubble parameter in $H_0 = 70.0^{+12.0}_{-8.0}$ km s$^{-1}$ Mpc$^{-1}$ (Abbott et al., 2017a; Escamilla-Rivera and Torres Castillejos, 2023).

The summary of these parameters related to the Hubble value tension can be found in Figure 1.1.

Regarding the second kind of tension, the clustering of matter measured by $\sigma_8$ or $S_8 = \sigma_8\left(\frac{\Omega_m}{0.3}\right)^{1/2}$, the direct measurements of the large-scale structure and the inferred by the probes of the early universe, also give some issues. The lower redshift measurements are lower than the ones obtained by the CMB estimations even though the determination of the $S_8$ quantity is in all cases model-dependent (Abdalla et al., 2022). The use of the $S_8$ parameter also correspond with the usefulness of incorporating the matter density in the analyses. This make that the combination measures the amplitude of the matter perturbations and the statistics of the galaxy clusters in the large scale universe (Poulin et al., 2023).

In the case of the CMB-based measurements, the Planck satellite measured $S_8 = 0.834 \pm 0.013$ including all fields and the lensing (Aghanim et al., 2020b). The combination between ACT and WMAP yields $S_8 = 0.840 \pm 0.030$, consistent with the previous Planck result (Aiola et al., 2020). For large-scale measurements such as the galaxy clustering statistics, the $S_8$ parameter is related to the $f\sigma_8(z = 0)$ parameter, where $f = [\Omega_m(z)]^{0.55}$ that approximates the growth rate in GR as a function of the matter density. Results of this kind are the measurements with BOSS DR12 in which the correlation function for the galaxy sample is measured that obtains $S_8 = 0.703 \pm 0.045$ (Ivanov et al., 2020) and the obtained by Kilo-Degree Survey (KiDS-1000) in a similar method arising a result of $S_8 = 0.759^{+0.024}_{-0.021}$ (Asgari et al., 2021).

As we can notice, although Planck measures the CMB with high precision, the results obtained for the $H_0$ and $\sigma_8$ parameters are in a $5\sigma$ (Abdalla et al., 2022) difference from the ones at low $z$ measurements such as SH0ES (Riess et al., 2019, 2021b). Furthermore, there is also a $3\sigma$ tension for the $S_8$ parameter. Moreover, the obtained results in the CMB observations are *indirect*, and therefore they are model-dependent. For example, to constrain $H_0$ it is needed to assume an expansion history model and several early-time physical conditions (Bernal et al., 2016). In this context, the late time measurements for the different parameters only rely on our capacity to calibrate distances up to several megaparsecs (Mpc), and therefore, the uncertainty generated is

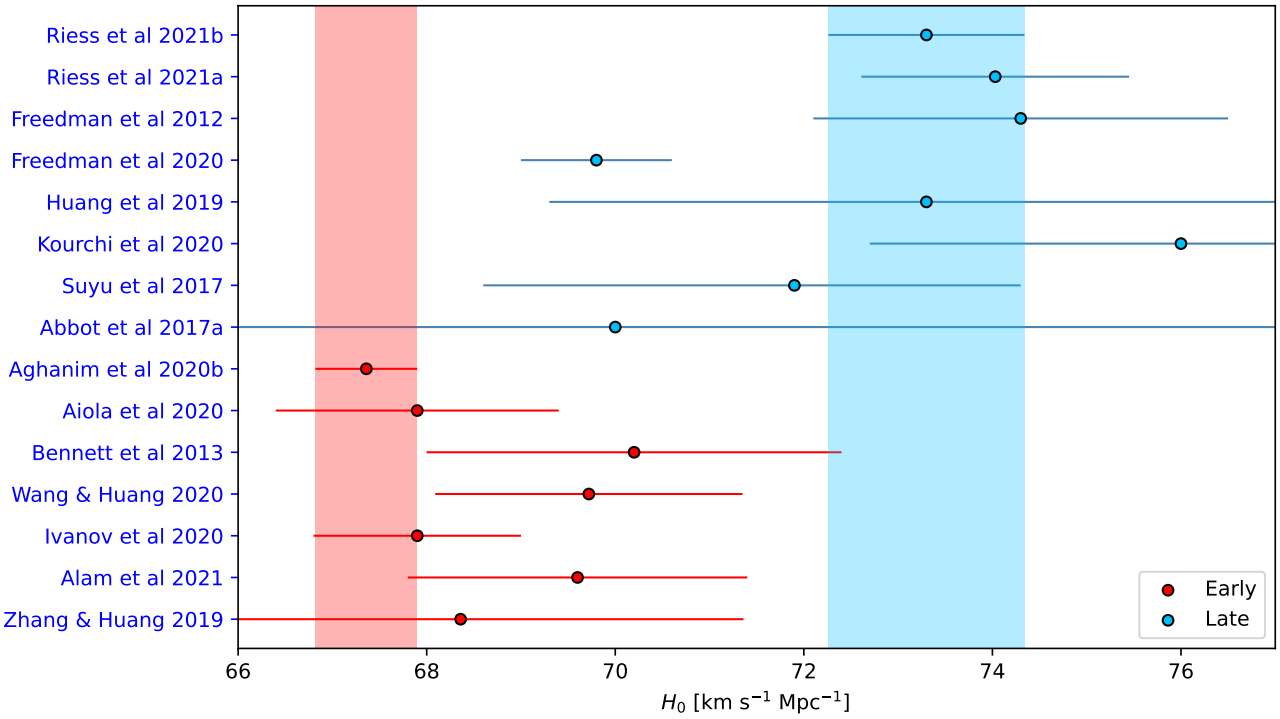


Figure 1.1: Whisker plot for the Hubble parameter values for several projects. The blue dots represent the late-time measurements of $H_0$. The red dots represent the early-time inferences of $H_0$. The blue and red shadowed regions represent the C.L from the SH0ES project Riess et al. (2022) measurement and the Planck 2018 determination Aghanim et al. (2020b), respectively.

larger and depends on other physical assumptions. Despite that, modified and extended gravity have popularity among studies for their potential to alleviate tensions.

As a step further, in this thesis, we consider extended theories of gravity with viable $f(T)$ models and constrain them with new data sets. Some advances in this line of work has been done in Briffa et al. (2022, 2023a), where using late measurements the $H_0$ tension is relaxed between $1-2\sigma$ with the CMB results using different $f(T)$ models preferring values closer to the estimations made with early universe assumptions, obtaining, for example, $H_0 = 68.5 \pm 1.1$ km s$^{-1}$ Mpc$^{-1}$.

## 1.2 Modified and extended theories of gravity

Extensions to the current understanding of gravity from GR have been widely studied in the literature to solve the ΛCDM and GR problems. However, we require that the extended theories fulfill some minimal requirements in the reproduction of the Solar System dynamics including the Newtonian dynamics in the weak field limit, the Galactic dynamics, the large-scale structure formation, and the reproduction of the cosmological parameters (Capozziello and De Laurentis, 2011). This means that a new theory or a generalization must cover the previous test to be a candidate for a generalization.

Some of these solutions for the cosmological problems include the introduction of a scalar field $\phi$ that in his properties could explain the inflationary epoch, and also the presence of a fluid with

negative pressure giving rise to so-called *quintessence* models (Faraoni and Capozziello, 2011). The problem with quintessence is that the the nature of the scalar field is still unknown and the lack of its explanation for the missing dark matter is still an open topic. Therefore, another approach to the problem of late cosmic acceleration is to understand it as a manifestation of some change in the theory of gravity.

- **Modified theories of gravity.** The simplest way to modify gravity is the idea behind $f(\mathcal{R})$. This kind of theory arises from the modification in one of the five postulates in the Lovelock theorem (Clifton et al., 2012). Its derivation came from the fact that we can consider high-order terms in the Lagrangian, e.g. fourth-order, to explain dark energy. Of course, not all the solutions are viable $f(\mathcal{R})$ are the most healthy solutions in this scheme, e.g. without unstable or ghost scenarios. The first ideas in this direction began to appear years after Einstein's first papers on GR and this is an attempt to generalize the Einstein-Hilbert action by adding different scalar curvature functions in the Lagrangian. In this modified version of gravity, we do not assume the linear dependence with the curvature scalar in the Einstein-Hilbert action in Eq. (1.6), and therefore

$$\mathcal{S}_{f(\mathcal{R})} = \frac{1}{2\kappa^2}\int \mathrm{d}x^4\sqrt{-g}f(\mathcal{R}) + \frac{1}{2\kappa^2}\int \mathrm{d}x^4\sqrt{-g}\mathcal{L}_m, \tag{1.16}$$

where $\mathcal{L}_m$ is the matter Lagrangian. In this case, the field equations are (Nojiri et al., 2017)

$$\frac{1}{2}g_{\mu\nu}f(\mathcal{R}) - \mathcal{R}_{\mu\nu}f'(\mathcal{R}) - g_{\mu\nu}\Box f'(\mathcal{R}) + \nabla_\mu\nabla_\nu f'(\mathcal{R}) = -\frac{\kappa^2}{2}\mathcal{T}_{\mu\nu}. \tag{1.17}$$

In this framework, the field equations using a flat FRLW metric (1.10) are

$$\frac{f(\mathcal{R})}{2} = 3\Big(H^2+\dot{H}\Big)f'(\mathcal{R}) - 18\Big(4H^2\dot{H}+H\ddot{H}\Big)f''(\mathcal{R}) + \kappa^2\rho_m, \tag{1.18}$$

$$-\tfrac{f(\mathcal{R})}{2} = -\Big(\dot{H}+3H^2\Big)f'(\mathcal{R}) + 6\Big(8H^2\dot{H}+4\dot{H}^2+6H\ddot{H}+\ddot{H}\Big)f''(\mathcal{R}) + 36\Big(4H\dot{H}+\ddot{H}\Big)^2 f'''(\mathcal{R}) + \kappa^2 p_m, \tag{1.19}$$

where the Hubble parameter adopts the same definition as $H = \dot{a}/a$, and in this case the scalar curvature $\mathcal{R}$ is equal to $\mathcal{R} = 12H^2 + 6\dot{H}$. Additionally, $\rho_m = (3/\kappa^2)H^2$ and $p_m = -1/\kappa^2\Big(3H^2+2\dot{H}\Big)$. So, in this case, the EoS can be given using only the Hubble parameter

$$w_{\text{eff}} = -1 - \frac{2\dot{H}}{3H^2}. \tag{1.20}$$

At first, the problem that we encounter using this kind of theory is that a description for $f(\mathcal{R})$ is needed, leading to a degeneracy of models. Using the arguments that a modified gravity theory must fulfill certain astrophysical and cosmological cutoffs, we must select the functions viable to use in the previous Lagrangian. In the specific case of $f(\mathcal{R})$ the necessary function is the one that unifies the accelerating expansion and the early-time inflation (Nojiri et al., 2017). The details of these procedures to find viable descriptions with this modified gravity can be found in Faraoni and Capozziello (2011), Clifton et al. (2012) and Nojiri et al. (2017), where extra features of the discussed theories are provided.

- **Extended theories of gravity.** The idea behind Teleparallel Gravity (TG) is to allow extension in the core of the connection, allowing instead of curvature, modifications of non-vanishing torsion or nonmetricity. Theories of this type are known as *teleparallel* theories of gravity. In *teleparallelism*, the Levi-Civita connection is substituted by the **Teleparallel** connection, where the torsion $T$ is used as a fundamental dynamical element instead of the Ricci scalar of curvature $\mathring{\mathcal{R}}$. This precisely came from the definition of the Levi-Civita connection. Under this scheme Lagrangian changes and becomes a function of $f(T)$ instead of $f(\mathring{\mathcal{R}})$, as in the previously mentioned modified gravity (Nojiri et al., 2017). But, in GR the curvature is used as a description of the space-time to mediate the gravitational interaction, meanwhile, in teleparallelism, the gravity is related to torsion accounting for the gravity interaction acting as a force. The torsion descriptions depend on the origins to justify the appearance of the geometry and the mechanism in which it modifies all the physical components in the universe as the velocity, acceleration, and dynamics of the expansion. The geometrical meaning of introducing the torsion is that when performing parallel transportation on a vector field the infinitesimal parallelogram breaks (contrary to the case in which the curvature is constructed when the parallel transportation changed the direction of the curve) (Cai et al., 2016). An intuitive way to understand this is to understand that parallel transportation does not return to the original place. The introduction of torsion in the gravitational theory came first from Einstein himself (Unzicker and Case, 2005) as an attempt to create a further generalization for the gravitational theory. The main difference between teleparallelism is the introduction of tetrad fields that can be adopted to define a different tool: the Weitzenböck connection that contains information about the torsion of the space instead of the curvature. This field of tetrads can be used to construct a metric $g_{\mu\nu}$ and this can be done because in the same space-time, the connection can be constructed, and using the field of tetrads both the curvature and teleparallelism formalism can be constructed independently. In the last few years, the attention to teleparallelism, especially to $f(T)$ theories, has been rising originating from the attempts to explain the different acceleration epochs of the universe and contrary to $f(\mathcal{R})$, the paradigm for $f(T)$ arrives to second order differential equations that essentially are the same to the ones in GR, with different features such as apparent solutions to cosmology issues. This topic will be explored carefully in the following sections.

### 1.2.1 Other theories to alleviate the Hubble tension

One of the most basic and direct attempts to alleviate these cosmological tensions is to derive better numerical and, in such cases, analytical solutions to the Friedmann equations (Sandoval-Orozco and Escamilla-Rivera, 2022). However, the results are not competitive with other options that explore new physics or try to reformulate the way we use existing data. Let us remember that this consistency needs to be fully in agreement with the observables and their systematics well-treated. However, involving new models of physics like a new description of gravity would not be so easy, because it involves new degrees of freedom related to new observed parameters contained in the theory. In addition, some proposals allow to explain the $H_0$ tension but fail to explain the $S_8$ tension and vice versa (Abdalla et al., 2022), and for that reason, it is necessary to perform fittings with several groups of data coming from the different cosmic stages to give a more complete overview. Examples of different approaches include the constraints derived from black

hole observations via the luminosity distance and the size of the shadow (Escamilla-Rivera and Torres Castillejos, 2023). Other proposals include the use of statistical tools to explore further the current data like the use of Gaussian processes to address the $S_8$ tension (Reyes and Escamilla-Rivera, 2022), the constraints using $f(\mathcal{R})$ theories that recover a $H_0$ value close to the one obtained with CMB measurements, e.g. $H_0 = 69.5 \pm 2.0$ km s$^{-1}$ Mpc$^{-1}$ and alleviates the tension to $1.5\sigma$ (D'Agostino and Nunes, 2020). Furthermore, works on $f(T, B)$ cosmologies have also been showing some promising development where a cosmographic fit is performed (Escamilla-Rivera et al., 2021) for high redshift to constraint possible implications in the use of a modified gravity.

As problems regarding GR and deviations from the ΛCDM model began to arise, several different attempts to find some more general framework or even a new description of gravity have been brought to our attention.

Another example is the proposal of a theory $f(\mathcal{R}, T)$ in which a function of the curvature scalar and the energy-momentum tensor could solve the Hubble tension down to $2\sigma$ (Myrzakulov et al., 2023). Other ideas include the use of $f(Q)$ gravity in which the non-metricity tensor $Q_{\alpha\mu\nu} = \nabla_\alpha g_{\mu\nu}$ is introduced to generalize assumptions in the construction of gravity theories (Mandal et al., 2020), and that could potentially solve the existing tensions. Constraints on such models have been performed in (Lazkoz et al., 2019) using CMB and BAO, in (Barros et al., 2020) using Large Scale Structure (LSS), and (Nájera et al., 2023) using gravitational waves. Also, we found proposals that consider the replacement of the Newton constant $G$ with a time-varying $G(t)$ proposed by Brans and Dicke (Brans and Dicke, 1961) that solves the Hubble tension using the early-time data to $1\sigma$ (Solà Peracaula et al., 2019), and attempts to introduce quantum effects to gravitation via the non-local gravity that improves the $H_0$ estimation to $2\sigma$ tension with late time estimations (Belgacem et al., 2020).

Although the aforementioned proposals are not the only ones, we mention some examples of alternative ones of different natures to solve the current cosmological issues Perivolaropoulos and Skara (2022). Most complete reviews for the state-of-art in cosmology related to this topic can be found in (Di Valentino et al., 2021a; Abdalla et al., 2022).

## 1.3 Teleparallel Equivalent Theory of Gravity

The proposal of teleparallelism has been gaining momentum in the last decades as one of the extension candidates for GR (Bahamonde et al., 2021). In this theory, the curvature is replaced by torsion as the mechanism in which gravity is produced and it is based on the substitution of the curvature-based Levi-Civita connection by a torsion-based teleparallel connection known as the Weitzenböck connection.

The standard way of working in teleparallel gravity is in terms of tetrads, which are the basis of the tangent space from a point in a manifold (Golovnev, 2023).

### 1.3.1 Tetrads

To start talking about telleparalelism, we need to start with tetrads since they are the dynamic elements of the theory. They are defined as a base of orthonormal vectors $e^A_\mu$ where the Latin capital letters $A, B, C = 0, 1, 2, 3$ are the tangent space-time coordinates. These tetrads fulfill the

relations

$$e^{A}{}_{\mu}E_{B}{}^{\nu} = \delta^{\nu}_{\mu}, \qquad e^{\mu}{}_{A}E^{B}{}_{\nu} = \delta^{B}_{A}, \tag{1.21}$$

where $E^{A}{}_{\mu}$ is the inverse of the tetrad, and the metric can be written as

$$\eta_{AB} = \eta^{AB} = \text{diag}(1, -1, -1, -1); \tag{1.22}$$

and the space-time metric is derived using

$$g_{\mu\nu} = \eta_{AB}e^{A}{}_{\mu}e^{B}{}_{\nu}, \qquad g^{\mu\nu} = \eta^{AB}E_{A}{}^{\mu}E_{B}{}^{\nu}. \tag{1.23}$$

The featured theory of gravity in this thesis is the Teleparallel Equivalent Theory of Gravity (TEGR), in which an alternative to GR is constructed by substituting the curvature for the torsion (Maluf, 2013). In this theory, given a set of tetrad fields it is possible to construct the metric tensor $g_{\mu\nu}$ and the new connection is going to be used: the Teleparallel connection $\Gamma^{\lambda}{}_{\mu\nu} = E^{\lambda}{}_{A}\left(\partial_{\nu}e^{A}{}_{\nu} + \omega^{A}{}_{B\nu}e^{B}{}_{\mu}\right)$. Here the construction is a generalization of the Riemannian geometry. So, in this case, given a nontrivial tetrad, it is possible to construct a connection that involves torsion without curvature (Cai et al., 2016). We can expand the construction of the teleparallel connection as

$$\Gamma^{\sigma}{}_{\mu\nu} = E_{A}{}^{\sigma}\left(\partial_{\nu}e_{\mu}{}^{A} + \omega^{A}{}_{B\nu}e^{B}{}_{\mu}\right), \tag{1.24}$$

where $\omega^{A}{}_{B\mu}$ represents the components of the teleparallel spin connection (Bahamonde et al., 2021). The spin connection represent the Lorentz frame of this new geometric construction, allowing that the covariant derivative present all the necessary properties to transform covariantly under Lorentz transformations (de Andrade et al., 2001).

The connection satisfies the tetrad postulate as

$$\partial_{\mu}e^{A}{}_{\nu} + w^{A}{}_{B\mu}e^{B}{}_{\nu} - \Gamma^{\rho}{}_{\nu\rho}e^{A}{}_{\rho}, \tag{1.25}$$

where the vectors remain parallel, which gives rise to the name *teleparallel* gravity.

Using the spin connection description we can describe the curvature, torsion, and non-metricity tensors that are independent of the choice of the tetrad, and therefore we can define the curvature tensor as

$$R^{\alpha}{}_{\beta\mu\nu} = \partial_{\mu}\omega^{\alpha}{}_{\beta\mu} - \partial_{\nu}\omega^{\alpha}_{\beta\mu} + \omega^{\alpha}_{\gamma\mu}\omega^{\alpha}_{\beta\nu} - \omega^{\alpha}_{\gamma\nu}\omega^{\gamma}_{\beta\mu}, \tag{1.26}$$

with the torsion tensor

$$T^{\alpha}{}_{\mu\nu} = \partial_{\mu}e^{\alpha}{}_{\nu} - \partial_{\nu}e^{\alpha}{}_{\mu} + \omega^{\alpha}{}_{\beta\mu}e^{\beta}{}_{\nu} - \omega^{\alpha}{}_{\beta\nu}e^{\beta}{}_{\mu}, \tag{1.27}$$

and the non-metricity tensor

$$S_{\mu\alpha\beta} = \nabla_{\mu}g_{\alpha\beta} = -\eta_{\alpha\gamma}\omega^{\gamma}{}_{\beta\mu} - \eta_{\gamma\beta}\omega^{\gamma}{}_{\alpha\mu}. \tag{1.28}$$

If the spin connection is zero, the torsion tensor only depends on the tetras as:

$$T^{\lambda}{}_{\mu\nu} = E_{A}{}^{\lambda}\left(e^{A}{}_{\nu,\mu} - e^{A}{}_{\mu,\nu}\right), \tag{1.29}$$

where this connection is known as the Weitzenböck connection.

To explore further the concept of torsion we need to consider two curves $C_1$ parameterized by the $\lambda$ parameter as $x^\mu = x^\mu(\lambda)$ and $C_2$ parameterized by $\tilde{x}^\mu = \tilde{x}^\mu(\lambda)$. So, if we calculate the displacement of a tangent vector $u^\mu$ along $C_2$ and obtain a $u'^\nu$ in first order we will obtain

$$u'^\nu = u^\nu + (\partial_\nu u^\nu)\mathrm{d}\tilde{x}^\nu, \tag{1.30}$$

where $\mathrm{d}\tilde{x}^\mu$ represents the displacement mentioned before. If we recall that $u^\nu$ is a parallel transported vector and

$$\frac{\mathrm{d}\tilde{x}^\mu}{\mathrm{d}\lambda}\nabla u^\nu = 0 = \frac{\mathrm{d}\tilde{x}^\mu}{\mathrm{d}\lambda}\partial_\mu u^\nu + \Gamma^\nu{}_{\beta\mu}\frac{\mathrm{d}\tilde{x}^\mu}{\mathrm{d}\lambda}u^\beta. \tag{1.31}$$

So, separating the terms we obtain:

$$(\partial_\mu u^\nu)\mathrm{d}\tilde{x}^\mu = -\Gamma^\nu{}_{\beta\mu}u^\beta\tilde{u}^\mu\mathrm{d}\lambda. \tag{1.32}$$

Introducing this latter to the expression for $u'^\nu$ we obtain

$$u'^\nu = u^\nu - \Gamma^\nu{}_{\beta\mu}u^\beta\tilde{u}^\mu\mathrm{d}\lambda. \tag{1.33}$$

Performing the same procedure now using the displacement of $\tilde{u}^\mu$ along $C_1$ we arrive at the expression

$$\tilde{u}'^\nu = \tilde{u}^\nu - \Gamma^\nu{}_{\beta\mu}\tilde{u}^\beta u^\mu\mathrm{d}\lambda. \tag{1.34}$$

Finally, we can express the combined previous expressions (1.33) and (1.34) with some index relabeling as:

$$(\tilde{u}^\nu + u'^\nu) - (u^\nu + \tilde{u}'^\nu) = -T^\nu{}_{\mu\beta}\,\tilde{u}^\mu u^\beta\mathrm{d}\lambda. \tag{1.35}$$

If the vectors $(\tilde{u}^\nu + u'^\nu)$ and $(u^\nu + \tilde{u}'^\nu)$ are the same, $T^\nu{}_{\beta\mu} = 0$. So, the torsion tensor $T$ represents the closeness of a curve in the parallel transport of two vectors in different geometries. If we define the vector that shows the deviation from an infinitesimal parallelogram as $V^\alpha\mathrm{d}\lambda = (\tilde{u}^\alpha + u'^\alpha) - (u^\alpha + \tilde{u}'^\alpha)$ we can express the torsion tensor simply as

$$V^\alpha = -T^\alpha{}_{\mu\nu}\,\tilde{u}^\mu u^\nu, \tag{1.36}$$

and this represents the cracked parallelogram that is true for small displacements in the directions of $\tilde{u}^\mu$ and $u^\nu$ computed at the starting point of the path of the transport (Akrami et al., 2021).

The use of the teleparallel geometry causes the parallel transport along a curve to be non-trivial and to change the transported vector making it not symmetric under exchanging the transported vector and the direction of transport (Bahamonde et al., 2021).

### 1.3.2 Teleparallel Equivalent Field Equations

In the direction of the TEGR, we need to introduce the contortion tensor given by

$$K^\alpha{}_{\mu\nu} = \Gamma^\alpha_{\mu\nu} - \mathring{\Gamma}^\alpha_{\mu\nu} = \frac{1}{2}\big(T_\mu{}^\alpha{}_\nu + T_\nu{}^\alpha{}_\mu - T^\alpha{}_{\mu\nu}\big), \tag{1.37}$$

which is defined entirely on the torsion tensor quantities much like the Riemann tensor is defined entirely on the Levi-Civita connection. This tensor takes into account the difference between the teleparallel and the Levi-Civita connections. We can define also

$$L^\mu{}_{\nu\rho} = \frac{1}{2}\big(Q^\mu{}_{\nu\rho} - Q_\mu{}^\mu{}_\rho - Q_\rho{}^\mu{}_\nu\big), \tag{1.38}$$

that quantifies the non-metricity. So, the Riemann curvature tensor can be written in the form

$$R^{\mu}{}_{\nu\rho\sigma} = \mathring{\mathcal{R}}^{\mu}{}_{\nu\rho\sigma} - \nabla_{\rho} D^{\mu}{}_{\nu\rho} - \nabla_{\sigma} D^{\mu}{}_{\nu\rho} + D^{\mu}{}_{\tau\rho} D^{\tau}{}_{\nu\sigma} - D^{\mu}{}_{\tau\sigma} D^{\tau}{}_{\nu\rho} \tag{1.39}$$

where a new distortion tensor is defined as

$$D^{\mu}{}_{\nu\rho} = \Gamma^{\mu}{}_{\nu\rho} - \mathring{\Gamma}^{\mu}{}_{\nu\rho} = K^{\mu}{}_{\nu\rho} + L^{\mu}{}_{\nu\rho}. \tag{1.40}$$

If we chose a vanishing curvature tensor $R^{\mu}{}_{\nu\rho\sigma} = 0$ we can express the Levi-Civita connection Riemann tensor as

$$\mathring{\mathcal{R}}^{\mu}{}_{\nu\rho\sigma} = K^{\mu}{}_{\tau\sigma} K^{\tau}{}_{\nu\rho} - K^{\mu}{}_{\tau\rho} K^{\tau}{}_{\nu\sigma} + \nabla_{\sigma} K^{\mu}{}_{\nu\rho} - \nabla_{\rho} K^{\mu}{}_{\nu\rho}, \tag{1.41}$$

in terms of the contortion tensor. So, the Ricci scalar can be expressed as

$$\mathring{\mathcal{R}} = K^{\mu}{}_{\rho\nu} K^{\rho\nu}{}_{\mu} - K^{\mu}{}_{\rho\mu} K^{\rho\nu}{}_{\nu} - 2\nabla_{\mu} K^{\mu\nu}{}_{\nu}, \tag{1.42}$$

that can be traced to (Bahamonde et al., 2021)

$$R = -T + 2\nabla_{\mu} T_{\nu}{}^{\nu\mu} = -T + B \tag{1.43}$$

where $B$ is the boundary term and $T$ is the torsion scalar that can be defined by multiple forms (Akrami et al., 2021). The boundary term $B$ guarantees the dynamical equivalence between the Einstein-Hilbert and the TEGR action constructed from the torsion scalar (Bahamonde et al., 2021). One of the representations of $T$ can be given by

$$T = \frac{1}{2} T^{\rho}{}_{\mu\nu} S_{\rho}{}^{\mu\nu} = \frac{1}{4} T^{\mu\nu\rho} T_{\mu\nu\rho} + \frac{1}{2} T^{\mu\nu\rho} T_{\rho\nu\mu} - T^{\mu}{}_{\mu\rho} T_{\nu}{}^{\nu\rho}, \tag{1.44}$$

using the superpotential as

$$S^{\mu}{}_{\mu\rho} = K^{\mu\rho}{}_{\rho} - \delta^{\mu}_{\rho} T_{\sigma\sigma\nu} + \delta^{\nu}_{\rho} T_{\sigma}{}^{\sigma\mu}. \tag{1.45}$$

In the boundary, a divergence does not affect the field equations. Assuming a teleparallel geometry one may transform the Einstein-Hilbert action shown (1.6) into alternative formulations (Bahamonde et al., 2021). As the torsion tensor encompasses all the information about the gravitational field (Bengochea and Ferraro, 2009) the dynamical equations for this TEGR can be constructed based on this tensor that can be read as

$$S_{\text{TEGR}} = -\frac{1}{2\kappa^2} \int \mathrm{d}^4x |e| T + \frac{1}{2\kappa^2} \int \mathrm{d}x^4 |e| \mathcal{L}_m. \tag{1.46}$$

Using the notation where $|e| = \det\left(e^A_{\mu}\right) = \sqrt{-g}$, and the variation of this action yields the following field equations

$$\nabla_{\rho} S_{(\mu\nu)}{}^{\rho} - \frac{1}{2} S_{(\mu}{}^{\rho\sigma} T_{\nu)\rho\sigma} + \frac{1}{2} T g_{\mu\nu} = \kappa^2 \mathcal{T}_{\mu\nu}. \tag{1.47}$$

Notice that the *l.h.s* is similar to the ones obtained using the Einstein-Hilbert action, so the equations are completely equivalent to the ones in GR. In this teleparallel context, we are capable of introducing a whole new class of theories known as $f(T)$, where $f$ is the functional of the torsion scalar $T$ in an attempt to generalize further the previously obtained field equations (Akrami et al., 2021) to incorporate the missing observational features like the late time acceleration.

The action describing the modified teleparallel gravity for $f(T)$ is given by

$$\mathcal{S}_{f(T)} = \frac{1}{2\kappa^2}\int \mathrm{d}x^4|e|[-T + f(T)] + \frac{1}{2\kappa^2}\int \mathrm{d}x^4|e|\mathcal{L}_m, \tag{1.48}$$

where again, $\mathcal{L}_m$ is the matter Lagrangian. It is important to notice that the teleparallel connection has been employed only in the gravitational part of the action and the matter action remains unchanged, although is possible to couple the matter and the geometric connection (Bahamonde et al., 2021). Also, using tetrads as dynamical variables of the theory, instead of the metric allows us to obtain second differential equations.

Variation of the action respect to the tetrad $e^A{}_\mu$ give us the field equations

$$\begin{aligned} W^\mu{}_\alpha :=& \frac{1}{e}\partial_\mu\big(eE_\alpha{}^\rho S_\rho{}^{\mu\nu}\big)[f_T - 1] - E_\alpha{}^\lambda T^\rho{}_{\nu\lambda} S_\rho{}^{\nu\mu}[f_T - 1] + \frac{1}{4}E_\alpha{}^\mu[f(T) - T] \\ &+ E_\alpha{}^\rho S_\rho{}^{\mu\nu}\partial_\nu(T) f_{TT} + E_\beta{}^\lambda \omega^\beta{}_{\alpha\nu} S_\lambda{}^{\nu\mu}[f_T - 1] = \kappa^2 E_\alpha{}^\rho \mathcal{T}_\rho{}^\mu; \end{aligned} \tag{1.49}$$

where $f_T = f'(T) = \partial_T f$ just to simplify the notation. The previous field equations can therefore be represented as

$$W_{(\mu\nu)} = \kappa^2 \Theta_{\mu\nu}, \quad \text{and } W_{[\mu\nu]} = 0. \tag{1.50}$$

In the field equations, the tetrad and the spin connection are represented in respectively each of the symmetric and antisymmetric operators upon $W_{\mu\nu}$. Specifically, if we chose that the spin connection vanishes, we have the Weitzenböck gauge (Briffa et al., 2023b). In this specific choice of gauge, the ten tetrad differential equations are the gravitational equations of motions.

So, the next step is to choose a specific tetrad and the function $f(T)$ to describe our physical situation. One of the effects of introducing the teleparallel connection is that the geodesic equation is changed. Originally, using the Levi-Civita connection the geodesic equation was described as:

$$\frac{\mathrm{d}^2x^\mu}{\mathrm{d}\tau^2} + \mathring{\Gamma}^\mu{}_{\alpha\beta}\frac{\mathrm{d}x^\alpha}{\mathrm{d}\tau}\frac{\mathrm{d}x^\beta}{\mathrm{d}\tau} = 0, \tag{1.51}$$

that describes the path of test particles. In the teleparallel geometry, the geodesic equation changes to:

$$\frac{\mathrm{d}^2x^\mu}{\mathrm{d}\tau^2} + \Gamma^\mu{}_{\alpha\beta}\frac{\mathrm{d}x^\alpha}{\mathrm{d}\tau}\frac{\mathrm{d}x^\beta}{\mathrm{d}\tau} = K^\mu{}_{\alpha\beta}\frac{\mathrm{d}x^\alpha}{\mathrm{d}\tau}\frac{\mathrm{d}x^\beta}{\mathrm{d}\tau}, \tag{1.52}$$

which reflects the transformation from the curvature-based connection to the torsion-based based. This equation represents how the equation recovers that the particles are influenced by a force-like contribution (Bahamonde et al., 2021) in the form of the contortion tensor which acts on test particles as a force term.

# Chapter 2

# Precision Cosmology for Teleparallel Gravity

With the fast rate of increasing data overcoming within the new collaborations and missions, we are in the era to attend the standard cosmology as *precision cosmology* (Escamilla Rivera and Vecchyo, 2023). Precision is the main characteristic in which we deal with statistics and probabilistic schemes (Escamilla-Rivera, 2021). While the possibility to constrain cosmological models has been done for several years, we are now capable of classifying and exploring the probability of these models to reproduce the observational data. Furthermore, there have been studies that attempt to break the degeneracy of standard cosmologies to explore a unique scenario that can fulfill all the conditions required at the further sides of the distance ladder. However, the majority of the proposal arrives at the same conclusion: we require a new cosmological model that gives us a first-principle explanation of the dark sector and solves the cosmological tensions at the same time. Even when deviations from the ΛCDM model and modified gravities can explain one or another, there has not been a consensus on which is the right path.

In this line of thought, performing precision cosmology in extended theories of gravity has offered a viable path to tackle these issues from first principles, i.e. from a Lagrangian formulation we can identify naturally if these dark components come from geometry effects and how they can be constrained with data.

The most interesting applications in this direction are $f(T)$ theories, which attempt to describe the late-time cosmic acceleration and fulfill the constraints using SNIa catalogs. Furthermore, the cosmological models derived from these theories allow us to explain the nature of this phenomenon as a merely geometrical consequence without recurring to dark energy (Maluf, 2013). Another interesting characteristic of the $f(T)$ theories is the possibility of relaxing the cosmological tension related to $H_0$ and $f\sigma_8$, the latter by avoiding the dark matter component added as a matter contribution or a scalar field (Akrami et al., 2021). Several $f(T)$ models have been proposed for specific goals to solve cosmological problems, and in this thesis, four different models will be explored, each one proposed with different characteristics as we shall see.

## 2.1 Cosmology for Teleparallel Equivalent Gravity

To develop cosmological treatments in TG, we require the Weitzenböck connection. The problem arises when doing a linear transformation of the tetrads, where the torsion tensor is non-covariant (Bahamonde et al., 2021). In such case, the term *good tetrad* was started using to refer to tetrads and spin connections that preserve the invariance over linear transformations and that led to non-trivial solutions of the field equations of $f(T)$ gravity. In this scheme, the spin connection needs to be different from zero to fulfill the geometric necessities. In TG, one tetrad could have a nonzero spin connection that fulfills the symmetries of the physical problem and also solves the antisymmetric part of the field equations (1.50). So, a good tetrad fulfills being compatible with the choice of spin connection and solves the field equations without constraining the theory itself (Bahamonde et al., 2021).

In TG, the two good tetrads to describe the positive curvature parameter $k = +1$ and the negative curvature parameter $k = -1$, are similar to each other. The case $k = 0$ makes them both coincide with each other (Bahamonde et al., 2021). At this point, we are interested in the tetrad that does not incorporate the curvature effects, so the tetrad used to obtain FLRW cosmologies with $k = 0$ can be written as (see e.g. Eq.1.10)

$$ds^2 = \text{diag}(1, a(t), a(t), a(t)), \tag{2.1}$$

that using the vanishing spin connection and the definition of the torsion scalar and the boundary term becomes

$$T = -6H^2, \quad B = -18H^2 - 6\dot{H}, \tag{2.2}$$

and this becomes the Ricci scalar as

$$\mathring{\mathcal{R}} = -T + B = -12H^2 - 6\dot{H}. \tag{2.3}$$

This means that the Ricci scalar differs by a boundary term which guarantees the dynamical equivalence between the Einstein-Hilbert action (1.6) and the TEGR action (1.46). The boundary term is related to the Lovelock theorem that induces minor modifications in the Einstein-Hilbert action (Bahamonde et al., 2021). This means that in special cases, we can get rid of the boundary term since it does not contribute dynamically to the theory. This means that we are interested only in $f(T)$ theories rather than $f(T, B)$. In this case, the modified FLRW equations are described by

$$H^2 + \frac{f(T)}{3} f_T - \frac{f(T)}{6} = \frac{\kappa^2}{3}\rho, \tag{2.4}$$

$$\dot{H}(1 - f_T - 2T f_{TT}) = -\frac{\kappa^2}{2}(\rho + p), \tag{2.5}$$

where the sub index $T$ refers to partial derivative respect to the torsion scalar $T$ and the dot refers to time derivative as $\dot{f}_T = f_T T \dot{T}$. This equations are obtained by using the tetrad (2.1) in the field equations in (1.50).

In this newly modified Friedmann equation, the accelerated expansion of the universe codified in the dark energy has a gravitational origin, defining

$$\rho_{\text{DE}} = \frac{3}{\kappa^2}\left[-\frac{f}{6} + \frac{T f_T}{3}\right], \tag{2.6}$$

and therefore, a natural introduction of a negative EoS to explain the effect of the accelerated expansion. However, it requires the specification of $f(T)$ form to describe its evolution. In this case, the effective EoS can be written as

$$w_{\rm DE} = -\frac{\frac{f}{T} - f_T + 2T f_{TT}}{(1 + f_T + 2T f_{TT})\left(\frac{f}{T} - 2f_T\right)}, \tag{2.7}$$

and if $f_T = 0$ we recover the ΛCDM model condition in which $w_{\rm DE} = -1$ (Briffa et al., 2023a). By defining the normalized Hubble parameter $E(z) := H(z)/H_0$ we can rewrite the Hubble parameter in a useful manner as

$$E^2(z) = \Omega_m(1+z)^3 + (1-\Omega_m)y(z,b), \tag{2.8}$$

where $\Omega_m$ is the fractional matter density today and $y(z,b)$ is a function that depends on the free parameters introduced with the $f(T)$ functions (Wang and Mota, 2020) as

$$y(z,b) = \frac{1}{6H_0^2(1-\Omega_m)}\left[2T f_T - f\right]. \tag{2.9}$$

As we can notice, for all cosmological models, any deviation from the ΛCDM model is contained in the function $y(z,b)$. This is the first theoretical test to relax the degeneracy of models.

Once with the Friedmann evolution equations, we can explore its observational constraints by rewriting the dynamical quantities in terms of the observational parameters. To perform these calculations, it is necessary to find the relationship between these dynamical parameters and the measurements reported for each observational catalog. On this topic, we can classify the observables as:

- **Standard (Standarizable) candels.**

  To measure the distances in the universe it is necessary to adapt our measurements as the distance grows. With this in mind, we use the so-called cosmic distance ladder. For this method in astrophysics, we use standard candles, which are objects with a well-known luminosity (Weinberg et al., 2013). This is used because one of the only ways we can obtain information from distant objects is through their light. The distance ladder is calibrated locally using the parallax technique in which the distance of several hundred million stars is known as stars (Brown et al., 2021) including the variable Cepheids stars. In cosmology, the Period-Luminosity (PL) relation is well known used to measure distances as we can measure the apparent brightness in the sky ($m$) and we can infer the same quantity at 10 pc ($M$) using the PL relation. For more distant distances where Cepheids can no longer be measured SNIa are used as standard candles as we assume the maximum brightness is equal for all these events (Jones, 2017). This leads to the important distance modulus relation $\mu = m - M$ that will be used later.

  To connect the distance ladder with the cosmological models, we need to use the comoving distance that is the total line-of-sight of a photon traveling at redshift intervals $\mathrm{d}z'$ weighted by the Hubble parameter (Hogg, 2000) written as The luminosity distance can be written as

$$D_c(z) = \frac{c}{H_0}\int_0^z \frac{\mathrm{d}z'}{E(z')}, \tag{2.10}$$

where $c$ is the light speed in km/s and the result of the distance is written in Mpc units. The luminosity distance is the relation between the measured flux and the luminosity of an object in all frequencies across different redshifts (Hogg, 2000). This distance can be written in the following form

$$D_L(z) = (1+z)\frac{c}{H_0}\int_0^z \frac{\mathrm{d}z'}{E(z')} = (1+z)D_c(z), \tag{2.11}$$

and the distance modulus can simply be expressed as:

$$\mu(z) = 5\log_{10}\left(D_L(z)\right) + 25, \tag{2.12}$$

using Mpc units in the logarithm.

- **Standard rulers.** The standard rules rely on the assumption that we know the apparent size and shape of an object independent of the distance. In different studies, one of the most used rulers is the sound horizon at recombination epoch (Alam et al., 2017). This sound scale can be calculated explicitly from the integral

$$r_s(z) = \int_z^\infty \mathrm{d}z' \frac{c_s(z')}{H(z')}, \tag{2.13}$$

where the sound speed $c_s(z)$ can be approximated as $c_s \approx c[3+9/4\rho_b/\rho_\gamma]$ using $\rho_b$ and $\rho_\gamma$ are the baryon and photon densities. This sound horizon is the comoving distance traveled by a sound wave to the point of the last scattering surface of CMB photons (Stevens et al., 2023). It is important to notice that we refer, on one hand to *recombination* to the process when the universe had cooled enough for the first atoms to form. And on the other, at the time when those atoms stopped interacting with the photons is called the *drag epoch*. This is because in the hotter universe the interactions between matter and radiation created oscillations that stopped when the temperature conditions cooled down (Baumann, 2022).

  For the calculations of standard rulers it is also used the angular distance diameter $D_A(z)$ is as

$$D_A(z) = \frac{1}{1+z}\frac{c}{H_0}\int_0^z \frac{\mathrm{d}z'}{E(z')} = \frac{D_c(z)}{1+z}, \tag{2.14}$$

  and this is the derived distance used in standard rulers that depends on the cosmology used. The angular distance has some interesting effects as the apparent angular diameter decreases up to $z \sim 2.5$ where the objects start to grow in the sky due to the expansion of the Universe (Baumann, 2022).

## 2.2 $f(T)$ cosmological models

As we analyzed in the latter section, with Eq.(2.9) we can measure the degeneracy of cosmological models through viable deviations from the standard cosmological model. Once this condition is fulfilled, we can proceed with the selection of $f(T)$ models. In this scheme, several $f(T)$ models have been proposed to solve different astrophysical and cosmological issues, and some of these examples will be reviewed in this section.

### 2.2.1 Power Law model

One of the first $f(T)$ models analyzed at the cosmological level is the power law model. We refer to it as $f_1(T)$ (Bengochea and Ferraro, 2009), which proposes an explanation for the late time cosmic acceleration without invoking dark energy as a fluid component. Explicitly, the model introduces the specific function $f_1(T)$ as

$$f_1(T) = \alpha_1(-T)^{b_1}. \tag{2.15}$$

Evaluating the Friedmann equation (2.5) at late times (meaning the evaluation $T|_0 = T_0$) we obtain

$$\alpha_1 = \left(6H_0^2\right)^{1-b_1} \frac{1-\Omega_m}{1-2b_1}, \tag{2.16}$$

which means that $\alpha_1$ is not a free parameter and depends directly on the choice of $b_1$. So, analogous to ΛCDM we can write the normalized Hubble parameter as

$$E^2(z) = \Omega_m(1+z)^3 + (1-\Omega_m)E^{2b_1}(z), \tag{2.17}$$

which precisely reproduces ΛCDM when $b_1 = 0$. When $b_1 = 1$ the additional component in the Hubble parameter produces a gravitational constant term, and therefore, the $b_1 < 1$ will be a significant upper limit to take into account as a physical limit if we want to reproduce the observations of an accelerating universe (Briffa et al., 2022).

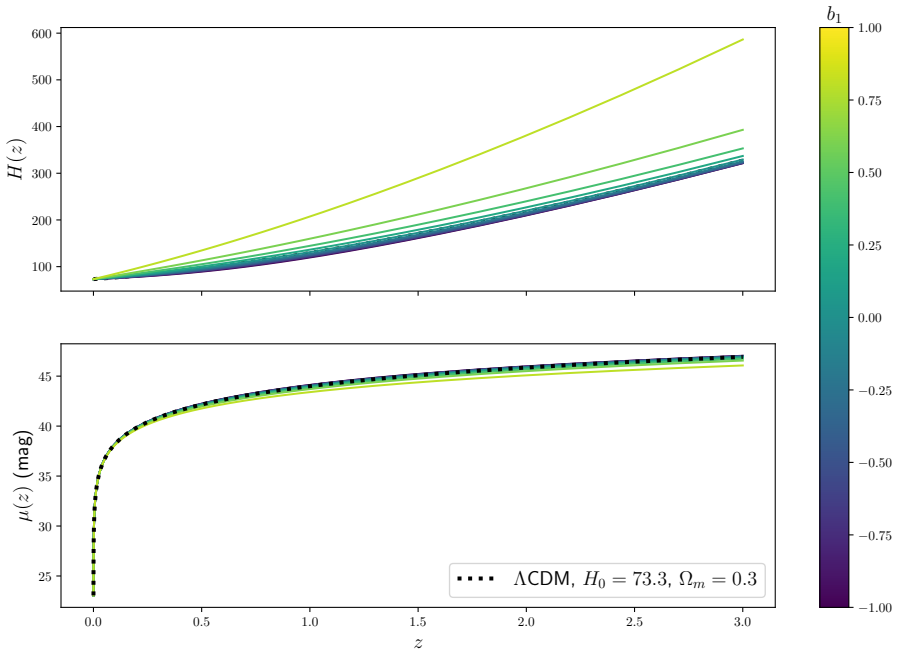


Figure 2.1: *Top:* Evolution of the Hubble parameter $H(z)$ (2.17). *Bottom:* Evolution of the modulus distance $\mu(z)$ (2.12), for the Power Law model (2.15). We denote in a dotted black line the ΛCDM model using conservative priors $H_0 = 73.3$km/s/Mpc and $\Omega_m = 0.3$. Different evolutions for this $f(T)$ are given with $b_1$ values (purple/green/yellow color lines).

### 2.2.2 Linder model

In Linder (2010) was proposed a model for $f(T)$ to *explicitly* avoid the use of an extra component of dark energy as a constant. This case is quite similar to a stable solution in $f(\mathcal{R})$ theories. For such a scheme, it is proposed an exponential dependence in the torsion scalar as

$$f_2(T) = \alpha_2 T_0 \left(1 - \exp\left[-b_2\sqrt{\frac{T}{T_0}}\right]\right), \tag{2.18}$$

where $\alpha_2$ and $b_2$ are constants and $T_0 = T|_{t=t_0} = 6H_0^2$. The introduction of the quotient $T/T_0$ is to avoid dealing with units in the exponential expression.

If we evaluate this function at current times we can reach an expression for the $b_2$ parameter given by

$$\alpha_2 = \frac{1-\Omega_m}{(1+b_2)e^{-b_2} - 1}. \tag{2.19}$$

Analogous to the previous model, notice that this function has only a free parameter $b_2$. We can rewrite the Friedmann equation for this case as

$$E^2(z) = \Omega_m(1+z)^3 + \frac{1-\Omega_m}{(b_2+1)e^{-b_2} - 1}\left[(1 + b_2 E(z)e^{-b_2 E(z)} - 1\right]. \tag{2.20}$$

The $f_2(T)$ model reduces to ΛCDM for $b_2 \to \infty$. For this model, it is usual to perform analyses using instead $1/b_2$ as the free parameter to achieve convergence, so that $1/b_2^+ \to 0$ turns into ΛCDM (Briffa et al., 2022).

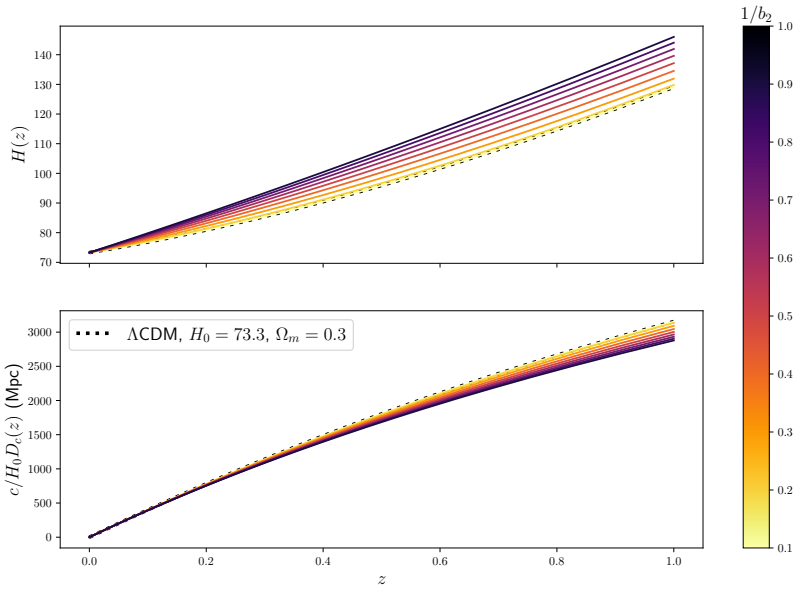


Figure 2.2: *Top:* Evolution of the Hubble parameter $H(z)$ (2.20). *Bottom:* Evolution of the total line-of-sight distance $\frac{c}{H_0}D_c(z)$ (2.10), for the Linder model (2.18). We denote in a dotted black line the ΛCDM model using conservative priors $H_0 = 73.3$km/s/Mpc and $\Omega_m = 0.3$. Different evolutions for this $f(T)$ are given with $b_1$ values (yellow/red/purple color lines).

### 2.2.3 Modified Linder model

Proposed in Nesseris et al. (2013) the modified Linder model takes into consideration not only the exponential factor, like in $f(\mathcal{R})$, but also considers another interpretation of new parameters in a $f_3(T)$ function to include corrections in these terms. This model is given by

$$f_3(T) = \alpha_3 T_0 \Big(1 - e^{-b_3 \frac{T}{T_0}}\Big), \tag{2.21}$$

where $\alpha_3$ and $b_3$ are constants. Evaluating this function at current times we obtain

$$\alpha_3 = \frac{1 - \Omega_m}{(1 + 2b_3)e^{-b_3} - 1}. \tag{2.22}$$

The Friedmann equation can be written in terms of the free parameters including $b_3$ as

$$E^2(z) = \Omega_m (1+z)^3 + \frac{1 - \Omega_m}{(1 + 2b_3)e^{-b_3} - 1}\Big[(1 + 2b_3 E^2(z))e^{-b_3 E^2(z)} - 1\Big]. \tag{2.23}$$

This behavior is similar to the one shown in $f_2(T)$, where for $b_3 \to \infty$ the model recovers $\Lambda$CDM, implying that again for the sake of analyses, $1/b_3$ is going to be the subject of the studies. In this case $1/b_3^+ \to 0$ recovers $\Lambda$CDM.

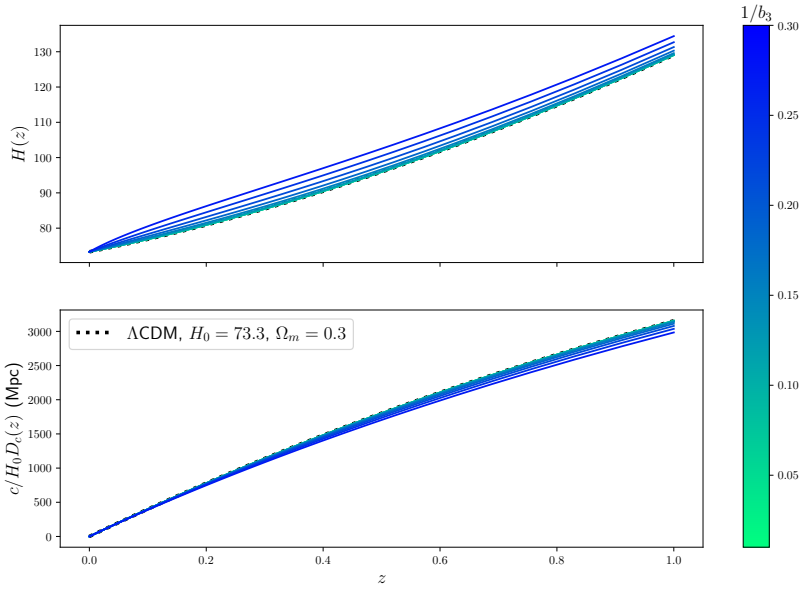


Figure 2.3: *Top:* Evolution of the Hubble parameter $H(z)$ (2.23). *Bottom:* Evolution of the total line-of-sight distance $\frac{c}{H_0} D_c(z)$ (2.10), for the Modified Linder model (2.21). We denote in a dotted black line the $\Lambda$CDM model using conservative priors $H_0 = 73.3$km/s/Mpc and $\Omega_m = 0.3$. Different evolutions for this $f(T)$ are given with $b_1$ values (green/blue color lines).

### 2.2.4 Logarithmic model

The logarithmic model was proposed in Bamba et al. (2011) and is described as

$$f_4(T) = \alpha_4 T_0 \sqrt{\frac{T}{b_4 T_0} \log\left(\frac{b_4 T_0}{T}\right)}, \tag{2.24}$$

where $\alpha_4$ and $b_4$ are constants. It is important to mention that in this model we have no set of specific values that recover the ΛCDM model. Using the same argument from the previous models and evaluating for $t = t_0$, only one free parameter is obtained

$$\alpha_4 = -\frac{(1-\Omega_m)\sqrt{b_4}}{2}, \tag{2.25}$$

and this reduces the Friedmann equation as

$$E^2(z) = \Omega_m(1+z)^3 + (1-\Omega_m)E(z). \tag{2.26}$$

This means that there is no additional free parameter apart from the ones related to the ΛCDM model, and therefore, in this case, we have no bias that recovers the standard cosmology.

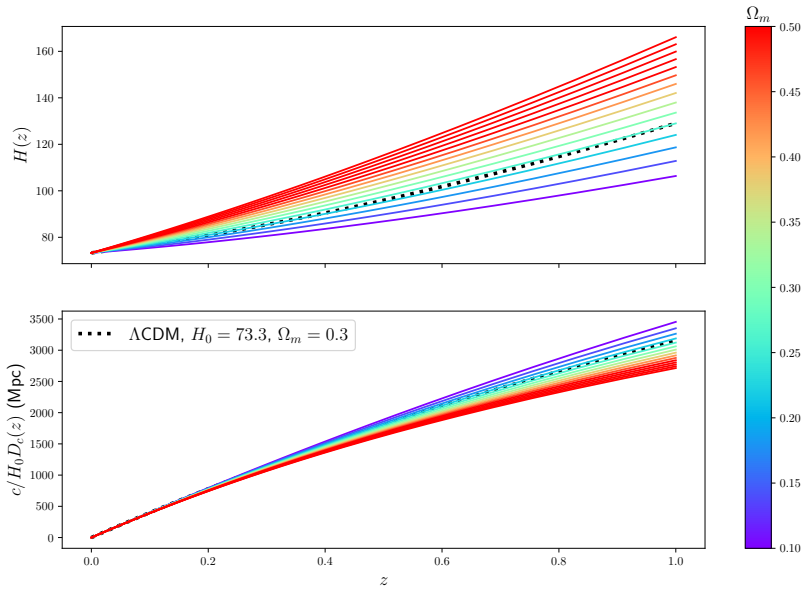


Figure 2.4: *Top:* Evolution of the Hubble parameter $H(z)$ (2.26). *Bottom:* Evolution of the total line-of-sight distance $\frac{c}{H_0} D_c(z)$ (2.10), for the Logarithmic model (2.24). We denote in a dotted black line the ΛCDM model using conservative priors $H_0 = 73.3$km/s/Mpc and $\Omega_m = 0.3$. Different evolutions for this $f(T)$ are given with $b_1$ values (purple/green/yellow/red color lines).

## 2.3 Precision cosmology for Teleparallel Gravity

After describing a well-behaved gravitational theory, it is important to confront its viability and predictions with the available observational data. From a purely gravitational point of view,

the first test should be at Solar System scales, in which our current GR understanding seems to be working well (Akrami et al., 2021). The formal approach to this is using the weak-field approximation that has to be essentially the Newton approximation to gravity. In the case of $f(T)$, is different because the dynamical element is the tetrads instead of the metric (Chen et al., 2015). $f(T)$ has tested successfully at Solar System scales (Iorio et al., 2015) and via orbital motions for the Power Law model (Iorio and Saridakis, 2012). Other observational bounds that need to be fulfilled are the detection of Gravitational Waves (Abbott et al., 2016), which constrain the speed of propagation for $f(T)$ predictions with the speed of light $c$, analogous to GR. In the experiments we obtain $|c/c_{\rm GW} - 1| \lesssim 2 \times 10^{-5}$ (Akrami et al., 2021) and the polarization modes are similar in both GR and $f(T)$ theories. At this point, we remember that at this level it is impossible to distinguish GR from TEGR, as we saw theoretically. More recently, the shadow of the Sgr A* black hole in the center of our galaxy (Akiyama et al., 2019, 2022) was used to test $f(T)$ theories Jusufi et al. (2022) and in the future, new kinds of probes like primordial black holes could give us insight about the early universe El Bourakadi et al. (2022).

Due to these tests, most of the TEGR models have been made at cosmological scales, where a deviation from GR and the ΛCDM model can be studied. We described some approaches as follows (Akrami et al., 2021):

- *Explaining the late acceleration of the universe without the cosmological constant.* As seen before, the $f(T)$ cosmology obtains naturally the result of an effective *dark energy* sector from gravitational nature as $w_{\rm DE} = \frac{3}{\kappa^2}\left[-\frac{f}{6} + \frac{T f_T}{3}\right]$, so the viability of the model is reduced to find meaningful physical models (Bahamonde et al., 2021). For example, the Power Law model (Bengochea and Ferraro, 2009) was developed to explain the cosmic late acceleration through a $T$ function that becomes important at $H \to H_0$.

- *Solving the cosmological tensions.* We have mentioned that TG could help to solve the $H_0$ tension. For example, using the Power Law model we can demonstrate that $f(T)$ could alleviate the tension down to $2.2\sigma$ using the early universe data Nunes (2018). Other examples use the Exponential function of $T$ to reduce the tension to $1.4\sigma$ through a Gaussian prior on $H_0$ (Hashim et al., 2021a), and calculations at a perturbative level reduce tension at $1\sigma$ using early data (Hashim et al., 2021b). A recent proposal on $f(T)$ shows a diminution of the Hubble tension (Briffa et al., 2023a). This thesis is focused in this direction.

- *Avoiding dark matter to describe galactic dynamics.* Although TG is not the only extension of gravity to introduce corrections to alleviate the galactic dynamics observed, this theory introduces only cosmological dark matter responsible for the structure formation in the early universe. This leaves the galactic rotation curves (Weinberg et al., 2013) to an explanation from within the same extension of the theory. Using $f(T)$ gravity as in Finch and Said (2018) we obtained successful rotation curves for the Milky Way using only the disk and the bulge in agreement with the data.

- *Solutions involving the early universe to describe inflation.* Cosmic inflation was proposed to solve the flatness, magnetic monopole, and horizon problems (Guth, 1981), where scalar fields have been proposed as the mechanism that led to that process. TG could be a good candidate to induce natural inflation from $f(T)$ models in a Born-Infeld context Ferraro and Fiorini (2008), and a Higgs inflation mechanism in a teleparallel context Raatikainen and Rasanen (2019). This is obtained naturally using an scalar field in the teleparallel theory.

### 2.3.1 Bayesian cosmology: numerical implementation

One of the goals of this thesis is to find cosmological constraints by analyzing the available observational data. The most popular methodology to perform these constraint analyses is the Bayesian method (Hobson, 2009; Trotta, 2017). The idea of using data to constrain cosmological parameters in different theories is to generate a deeper understatement of the physics that led to those measurements. This is in fact, the inverse problem of cosmology (Munõz and Escamilla-Rivera, 2020) in which we want to extract from the available data all the information we can have about the nature of a cosmological model, and from a theory of gravity.

The advantage of the Bayes method over other algorithms to constraint parameters is that the optimization algorithms take into account extra or *nuissance* parameters, e.g. the signal in background noise in an astrophysical image, the incorporation of a priori information about the parameters, the best performance in finding the *truth* value in robust models and the simplicity to incorporate several data sets to constraints the same set of parameters.

In this context, the Bayes theorem can be seen as (Hobson, 2009; Trotta, 2017)

$$\mathrm{P}(\theta|d) = \frac{\mathrm{P}(d|\theta)\mathrm{P}(\theta)}{\mathrm{P}(d)}, \tag{2.27}$$

where $\mathrm{P}(\theta|d)$ is the posterior probability for $\theta$ (or the cosmological parameters) that represents our degree of belief about the value of $\theta$ after the algorithm has seen the data $d$; $\mathrm{P}(d|\theta)$ is the likelihood or the probability of the data given a certain value of the parameters $\theta$, and finally $\mathrm{P}(d)$ is the prior probability distribution. The degree of belief in the parameter for the values of $\theta$ before the data is usually dominated by the physical conditions that determine the *real* or possible solutions. For example, as we shall see in our analysis, in the case of a power law model in $f(T)$ gravities, its free parameter is labeled $b_1 < 0$ for accelerating universe, and therefore the prior should be written to fulfill this condition.

The algorithms to perform Bayesian analyses take different approaches, but specifically for our analysis the used method is the Markov Chain Monte Carlo (MCMC). This MCMC process consists of a sequence of points in the parameters (*sample*) that is proportional to the density of the samples. Using some kind of generation of a new sample, we obtain that the final dataset depends only on the last position of the $n$ points. After several new generations of points, the distribution of these points converges to a distribution centered on the real value of the parameters. The generation of the new sample in computational methods usually relies on random number generation to generate the points, and it is decided in a process of maximizing the likelihood or closeness of the model to the data. In this thesis, we will quantify the values using the $\chi^2$ that will be described for each observational data set.

Finally, the computational version of MCMC used in our analyses is going to be a modified version of `emcee` (Foreman-Mackey et al., 2013). This is a code that implements a version of the affine-invariant ensemble sampler for the MCMC routine and it is one of the most used algorithms for both Astrophysics and Cosmology. Now, we will describe how to write the necessary code for an `emcee` routine in the context of $f(T)$ cosmologies.

We created a specific section of code dedicated to the theoretical calculations needed. As seen before, the free parameters will be $\Omega_m$, $H_0$ and the additional for every model named $b_i$, meaning that $\Theta = (\Omega_m, H_0, b_i)$. The mentioned free parameters are due to the fact that we are working in the late universe where radiation is no longer a notable contributor to the total energy density

(Aghanim et al., 2020b). So, for the cosmology part of the code, the calculations are done the following way:

1. Write the Friedmann equations in terms of the normalized Hubble parameter $E^2(z)$ as seen in Equations (2.17), (2.20), (2.23) and (2.26). As seen in those Equations, the parameter $E(z)$ is present in a polynomial form that we need to solve for every set of parameters.

2. Solve the polynomial for $E(z)$ using a root finder for each set of values for $\Theta$. In the case that the Hubble parameter $H(z)$ is needed, we perform $H(z) = H_0 E(z)$ to obtain the desired quantity.

3. Use this normalized parameter $E(z)$ value to perform the integral done in Equation (2.10). All the other distances to calculate come from this expression, so the rest of the theoretical quantities are calculated trivially.

We decided to put all the theoretical parts of the Hubble parameter calculations and the distances into one program so that we could use the results in the rest of the necessary steps. The next step is the calculation of the likelihood and the generation of the MCMC routine.

Almost all the likelihoods will be written as:

$$\mathcal{L} \propto -\frac{1}{2}\frac{(y_{\text{teor}} - y_{\text{obs}})^2}{\sigma_y^2}, \tag{2.28}$$

with $y^2_{\text{teor}}$ the modeled quantity for the desired model, $y^2_{\text{obs}}$ the observed or measured quantities and $\sigma_y$ the error associated to the measurements. This will be adapted depending on the details of each set.

For the MCMC routine, we will consider the following:

1. Select several steps required for the MCMC routine. This is the number of variations of the vector parameter $p$ that is going to be random varying.

2. Using the `EnsembleSampler` function we will construct the vector with dimension equivalent to the free parameters in $\Theta$. This is the vector that is going to vary freely to find the best fit.

3. We suggest using some kind of correlation check to quantify if the code is achieving convergence. This is imposed to avoid the code having to go through all of the steps and therefore make the code more efficient.

4. Use the likelihood functions and the derivated quantities to maximize the likelihood function to obtain the best fit using the `run_mcmc` function in the package.

5. We suggest using the `backend` function to save the progress for posterior analyses, in which the chains and the calculated likelihood will be stored.

   Finally, for the chains analyses, we suggest different public packages like `chainconsumer` (Hinton, 2016) and `getdist` (Lewis, 2019).

# Chapter 3

# Late-time observations: theory and constraints

To learn more about the aforementioned issues in the ΛCDM model it is important to keep using the available datasets and to continue to generate new ones. New datasets are crucial to learn about the systematic errors in the previous and to create a new playground to test alternative models. If this new data reaches bigger redshifts could help us to check if deviations from the standard model and to obtain more refined parameter estimations.

In this direction, for example, the Joint Light-Curve Analyses (JLA) sample of SNIa was upgraded by the Pantheon project (Scolnic et al., 2018) and the last one likewise improved by the Pantheon+ catalog (Riess et al., 2021b). The use of upgraded SNIa samples improved the estimations of $\Omega_m$ through time as $\Omega_m = 0.295 \pm 0.034$ for JLA to $\Omega_m = 0.298 \pm 0.022$ with Pantheon and finally to $\Omega_m = 0.334 \pm 0.018$ with Pantheon+. A similar effect had the update in the CMB observations from WMAP DR9 (Bennett et al., 2013) to the Planck Space Telescope (Aghanim et al., 2020a). Recently, the use of new observation instruments could bring new light to the calibration of parameters and explore areas that currently are not observed. The use of the cosmic distance ladder has its limits if we can detect brightness from events dimmer than the operative limits of telescopes like the Hubble Space Telescope (HST) (Scolnic et al., 2018). In this context, the use of the new James Webb Space Telescope (JWST) or the Euclid spectroscopic survey (Jelic-Cizmek et al., 2023) could bring a more and farther dataset than the previous instruments (Riess et al., 2023). The use of datasets obtained with these new instruments could bring light about the behavior of the universe at higher redshifts like the analyses done in Alonso et al. (2023).

Improvement in the cosmological measurements could help us to do a better calibration of the cosmological parameters. Additionally could also test the accuracy of the previous measurements and show us new issues with the parameters.

To perform the analyses for cosmological models, and tests for gravity theories, in certain regions of cosmic evolution, we divide the measurements as follows:

- **Late measurements (low redshift)**. We consider these as the ones that are independent of the standard ΛCDM model. From the cosmological tension issue, all of these measurements are in agreement with a higher $H_0$ value and are in tension with the CMB measurements. To treat models with these measurements we require the empirical method of the distance ladder, which allows us to measure $H_0$ locally, measuring the distance-redshift relation. One of the techniques used within this method is the parallax, which is used to calibrate the

luminosities of star types. Supernovae calibrated by Cepheids, as has been done by the SH0ES collaboration (Riess et al., 2022) belong to this division.

- **Early measurements (high redshift).** These are based on several assumptions, such as the model used to describe the evolution of the universe, i.e. the standard ΛCDM scenario, neutrino properties, or the dark energy. Also, we can consider initial values from the inflationary epoch, the number of relativistic particles, and dark matter properties. Since we are considering s fixed cosmology, the $H_0$ tension could be the indication of a failure of this model. All of these measurements are in agreement with a lower value for the $H_0$.

For completeness, we should mention that the ΛCDM model reproduces the majority of catalogs available in the literature. However, some issues arise in the mentioned $H_0$ and $\sigma_8$ tensions, and the aforementioned incomplete description regarding the nature of the dark matter and dark energy.

Dark energy, related to the late-time cosmic expansion, can be detected in the late universe, so the search for an answer in this sector will be using data available for the late universe. To distinguish the nature of this phenomenon between the standard cosmological constant $\Lambda$ and the propositions made using $f(T)$ gravity, in this work, we use low redshift data which can be crucial to study deviations from the standard model and possibly to find a solution to the cosmological tension. In this line of thought, we consider a set containing the samples of Cosmic Chronometers to measure $H(z)$, Supernovae Ia (SNIa), and two different quasars (QSO) samples. Additionally, we will use the BAO data set from different surveys to add at least one viewpoint from the early universe physics without the need to calculate the cosmological perturbations. This last data set will be used separately to contrast the different results taking into account that the surveys are sensitive to the theory and the dynamics that led to the growth of structure (Bahamonde et al., 2021; Zhao et al., 2019). Meanwhile, the late time data is more likely to be sensitive to the numerical analyses and the systematic errors of the data extraction. Therefore the BAO data set will have an impact on the $H_0$ estimation.

The different data sets each have their peculiarities that must be taken into account when analyzing them to contrast different cosmological models, so in this regard, we will describe each of the sets to be used in a Bayesian analysis.

## 3.1 Constraining cosmological models with measurements

In the cosmological parameter estimation, we have dataset D with a model with free parameter vector $\Theta$ from which the data will generate the set of best parameters in the form of likelihood $\mathcal{L}$. We usually have a prior distribution for those parameters that represent the previous knowledge about the parameters or the physical limits of the numerical values can take (Liddle, 2009).

Bayesian inference works by updating our state of knowledge about a parameter as new data is processed in every iteration of the numerical process (Trotta, 2017). In this direction, every iteration becomes the next information that the code updates in the space parameter provided depending on the cosmological model.

MCMC methods based on Bayesian statistics are known as the most important tool for cosmologists to work with. Other methods include the techniques of *deep learning* (Pan et al., 2020) in which machine learning techniques are used to estimate cosmological parameters from datasets that are very big for an MCMC routine to perform in a reasonable time.

In the next subsections, we are going to describe the observational catalogs and baseline used to constrain our $f(T)$ cosmologies from Chapter 2. In this Thesis, we will focus on late-time observations to study deviations from the ΛCDM model using the empirical distance ladder method.

## 3.2 Cosmic Chronometers measurements

The method called *Cosmic Clocks* or *Cosmic Chronometers* was first introduced by (Jimenez and Loeb, 2002). In this method, the Hubble parameter is measured using cosmology-independent methods starting from the definition

$$H(z) = \frac{\dot{a}}{a} = -\frac{1}{1+z}\frac{\mathrm{d}z}{\mathrm{d}t}, \tag{3.1}$$

where we need to measure the difference between two galaxy ages (to obtain $\Delta t$) that passively evolve and were formed roughly at the same time separated by a small redshift separation $\Delta z$. For a found pair of galaxies that match the requirements in redshift, the challenge is to measure the age difference to determine the observational Hubble parameter. As we can determine the redshift with a precision of $\delta z/z \lesssim 0.0001$ (Moresco et al., 2020) using spectroscopic techniques we now have to find an efficient and robust method to rely on the determination of the time difference using ages.

In this work, we used the 31 points obtained in (Moresco et al., 2016) that cover up to a redshift $z \leq 2$. The data for this sample was obtained from BOSS Data Release 9 (DR9) survey (Dawson et al., 2012) that originally was going to map the BAO and select a sample of passively evolving populations. The evolution of the stars in those galaxies only depends on nuclear processes, therefore we do not need to include any kind of cosmological assumption that makes the data sample model-dependent. This population of stars also contains a constant number density to avoid contamination while the stellar masses, emission lines, and velocity dispersion were already measured by the survey considered. The passive evolving galaxies are among the largest $M_{\mathrm{stars}} > 10^{11} M_{\odot}$, the earlier in age –most of them formed in redshift $z \gtrsim 2$– have not encountered a boost in star formation. Previous works have shown that instead of introducing the evolutionary stellar population synthesis models, the direct observation of the galaxy spectra, especially the break at 4000 Å was more effective and introduced less uncertainty for age estimation (Moresco et al., 2012).

The break at 4000 Å (D4000) is a good indicator of the metal absorption in the stellar contribution that can be related to the metallicity and therefore can be employed as an age indicator for the galaxy. For the selected objects this break is calculated by measuring the flux of the continuum between two bands: 3850-3950 Å and 4000-4100 Å as

$$\mathrm{D4000} = \frac{\left(\lambda_2^{\mathrm{blue}} - \lambda_1^{\mathrm{blue}}\right)\int_{\mathrm{red}} F_\nu d\lambda}{\left(\lambda_2^{\mathrm{red}} - \lambda_1^{\mathrm{red}}\right)\int_{\mathrm{blue}} F_\nu d\lambda}, \tag{3.2}$$

where $\int_{\mathrm{blue}} F_\nu d\lambda$ and $\int_{\mathrm{red}} F_\nu d\lambda$ are the integrals between the $\lambda_1$ and $\lambda_2$ limits for each continuum blue or red part. To use this relation, according to (Balogh et al., 1999) the D4000 break and the age of the galaxy are linear in the form D4000$= A \cdot \mathrm{age} + B$, where $A$ is the slope and $B$ is the normalization. Therefore we can express the Hubble parameter as:

$$H(z) = -\frac{1}{1+z} A \frac{\mathrm{d}z}{\mathrm{d(D4000)}}. \tag{3.3}$$

The factor $A$ represents the slope and includes the possible effects of metallicity and the star formation history. After analyzing the survey results, in (Moresco et al., 2016) was obtained the mentioned 31 points including $z, H(z)$, and a Covariance Matrix, which is a combination of uncertainties based on the different methods applied to calculate the age, includes the different stellar evolution models, the assumed star formation history, metallicity and statistical errors (Moresco et al., 2018, 2020).

Involving all, the $\chi^2$ for Cosmic Clocks is given as:

$$\chi^2_{H(z)} = \Delta H(z_i, \Theta)^T C^{-1}_{H(z)} \Delta H(z_i, \Theta), \tag{3.4}$$

where $\Delta H(z_i, \Theta) = H(z_i, \Theta) - H_{\mathrm{obs}}(z_i)$ comparing both the observed Hubble parameter and the theoretically calculated. $C^{-1}_{H(z)}$ is the covariance matrix mentioned before. One of the advantages of using the $H(z)$ measurements is that we do not need additional parameters to obtain the cosmological quantity.

More details about the usage of the matrix and the descriptions of the effect of using these systematic errors compared to the previous estimations are given in Appendix A.

## 3.3 Supernovae Ia

Supernovae Ia (SNIa) classification is based on spectra properties. In comparison to SN Type II features hydrogen emission lines, SN Type I does not have the same characteristic lines. This latter SN shows absorption due to ionized silicon at 6355 Å (Krisciunas, 2012). The standard scenario for the SNIa consists of a binary system where an explosion happens and a carbon-oxygen dwarf star (WD) approaches the Chandrasekhar limit of 1.4 $M_\odot$ by either gas gains from its main-sequence neighbor or from the merging of white dwarf stars. This means that SNIa represents some of the most energetic explosions of the entire Universe producing a luminosity $\sim 10^{43}$ erg s$^{-1}$ (Livio and Mazzali, 2018) and they occur in all types of galaxies.

SNIa exhibits a relation between the peak luminosity and both the rate of the decline after the maximum brightness and the color at the maximum (Livio and Mazzali, 2018) which can be expressed in the B-band as $M_{\max}(B) = \langle M^0_B \rangle + b\Delta m_{15}(B)$, where $\Delta m_{15}(B)$ represents the change in B-band magnitude 15 days after the peak of intensity and $b$ a quantity to be adjusted from the observations. This variation is about $\lesssim 2$ (Phillips, 1993) where we can find that the weighted average value $\langle M^0_B \rangle$ is obtained from the Cepheid-calibrated SNIa (Tripp and Branch, 1999). This specific trend in the luminosity curve has to do with the amount of Ni formed in the explosion as a result of the sudden change in temperature and ionization (Kasen and Woosley, 2007). The observed brightness can be linked to a progenitor with a mass between $0.1M_\odot \lesssim M \lesssim 1M_\odot$ (Wygoda et al., 2019) and understanding the physical conditions is the key to using them as standard candles. Additionally, the SNIa curve of luminosity is corrected by color complementing the relation shown previously, by adding the color correction for every detection, and the reddening caused by dust as

$$M_B = \langle M^0_B \rangle - b(\Delta m_{15} - 1.05) - R(B - V), \tag{3.5}$$

where $B$ and $V$ are the apparent blue and visual magnitudes, and in this case the $\Delta m_{15}$ is normalized to 1.05 (Tripp and Branch, 1999) as known as the Tripp calibration.

The calibration process for SNIa also uses the measured distance to a galaxy via the well-known Period-Luminosity (PL) relation for the Cepheid stars (Ngeow and Kanbur, 2006). This calibration is done when an explosion occurs in a galaxy where we have previously measured the distance using Cepheids (Mortsell et al., 2022). These variable stars have a very well-studied and fitted relation as $M = -5.93 - 3.96(\log P - 1)$ using their well-behaved aforementioned relation (Riess et al., 2018).

Fitting both $\langle M_B^0 \rangle$ for the measured Cepheids and SNIa in the same galaxy host we can obtain a calibration for the measured SN (Tripp and Branch, 1999; Mortsell et al., 2022). Cepheids also need calibration with a known working distance estimator as parallax (Riess et al., 2018). Therefore, in the host of this event, the calibration for the apparent magnitude can be expressed as $m_H = m_{\mathrm{F160W}} - 0.386(m_{\mathrm{F555W}} - m_{\mathrm{F814W}})$, using $m_{\mathrm{F555W}}$, $m_{\mathrm{F814W}}$, and $m_{\mathrm{F160W}}$ as the fibers used to measure the magnitude (Riess et al., 2018).

The sample that we use for our analysis with SNIa is the current *Pantheon* sample (Scolnic et al., 2018), which uses SN as standardizable candles by calibrating the apparent magnitude of the explosion measuring not only the $m$ but a correction for dust extinction, bias, and color. The calibration to obtain the light curves is expressed as

$$\mu = m_B - M + \alpha x_1 - \beta c + \Delta_M + \Delta_B, \tag{3.6}$$

where $\mu$ is the distance modulus, $\Delta_M$ is the correction in the distance based on the host-galaxy mass, $\alpha$ is the relation between luminosity and stretch, and $\beta$ is the relation between luminosity and color. The $\Delta_B$ is the correction for the distance accounting for the predicted biases from simulations and finally, $m_B$ is the apparent magnitude in the B-Band and $M$ is the absolute magnitude.

SNIa Pantheon sample consists of 1048 data points that measure the apparent magnitude for several explosion events of this type in a redshift range from $0.01 < z < 2.3$, and also provides the factors to reproduce the correction by the stretch, color, brightness of the host galaxy, position bias and so to reproduce the data. The aforementioned 1048 points are necessary to represent the cosmological quantity $\mu = m - M$, where the absolute magnitude $M$ is going to be calibrated for every $H_0$ value as a degeneracy between these two values is present (Zhang et al., 2021). The $\chi^2$ for this sample is

$$\chi^2_{\mathrm{SNIa}} = \Delta\mu(z_i, \Theta)^T C^{-1}_{\mathrm{SNIa}} \Delta\mu(z_i, \Theta) + \ln\left(\frac{S}{2\pi}\right), \tag{3.7}$$

where $C^{-1}_{\mathrm{SNIa}}$ is the inverse of the covariance matrix for the data sample, $S$ is the sum of all components of the inverse of the matrix and $\Delta\mu(z_i, \Theta)$ is the difference between the data and the calculated theoretically distance modulus

$$\mu(z_i, \Theta) = 5 \log_{10}(D_L) + 25, \tag{3.8}$$

when using the units in Mpc and $D_L$ is the luminosity distance.

## 3.4 Baryon Acoustic Oscillations

The Baryon Acoustic Oscillation (BAO) method is based on the relics left behind by the sound waves in the early cosmic times that caused a statistical imprint on the clustering of galaxies and matter distribution in the late Universe (Weinberg et al., 2013). To calculate BAO the so-called Statistical Standard Rule (SSR) is used. The waves were caused by the early plasma of coupled baryons to photons oscillating between the gravitational attraction and the perturbation from the photon pressure, so eventually when electrons and protons form hydrogen the photons escape freely leaving the sound wave shells of baryon frozen in the imprint of galaxy power spectrum (Perivolaropoulos and Skara, 2022). These techniques are distinct three-dimensional clustering patterns imprinted in the spatial distribution of galaxies that map the expansion history and the structure growth of the universe (Zhao et al., 2019).

The BAO technique measures distances using this *standard rule* (see Chapter 2), which means we need an object of known size at a known distance (or redshift $z$) whose change in size as it gets further in distance. This method is very well understood so we can keep track of how the universe is changing through different redshift $z$ bins. For that we measure separations on the transverse line of sight measured by changes in the angle of vision that depend on the angular diameter distance and the comoving sound horizon at the baryon drag epoch $D_A(z)/r_s$ (Bassett and Hlozek, 2009). The needed quantities to use the BAO measurements include this distance, and several other physical quantities (Weinberg et al., 2013; Bargiacchi et al., 2022; Bassett and Hlozek, 2009) and calculated as

$$D_A(z) = \frac{c}{H_0(1+z)\sqrt{-\Omega_k}} \sin\left(\sqrt{-\Omega_k}\int_0^z \frac{\mathrm{d}z'}{E(z')}\right), \tag{3.9}$$

where $\Omega_k = 0$ for a flat universe and the angular diameter distance is simply calculated as $D_A(z) = \frac{c}{H_0}(1+z)\int_0^z \frac{\mathrm{d}z'}{E(z')}$. The sound horizon at the baryon drag epoch

$$r_s(z_d) = \int_{z_d}^{\infty} \frac{c_s(z')}{H(z')}\mathrm{d}z', \tag{3.10}$$

using $c_s$ is the sound speed will be calculated from cosmological fixed parameters as

$$c_s(z) = \frac{c}{\sqrt{3\left[1+\frac{3\Omega_{b,0}}{\Omega_{\gamma,0}}\frac{1}{1+z}\right]}}, \tag{3.11}$$

and the redshift at the baryon drag epoch $z_d$ can be calculated in several ways (Aizpuru et al., 2021), one of them as

$$z_d = \frac{1291(\Omega_m h^2)^{0.251}}{1+0.659(\Omega_m h^2)^{0.828}}\left[1+b_1\left(\Omega_{b,0}h^2\right)^{b_2}\right], \tag{3.12}$$

with

$$b_1 = 0.313\left(\Omega_m h^2\right)^{-0.419}\left[1+b_1\left(\Omega_{b,0}h^2\right)^{b_2}\right], \tag{3.13}$$

$$b_2 = 0.238\left(\Omega_m h^2\right)^{0.223}. \tag{3.14}$$

In these mentioned relations, $\Omega_{\gamma,0}$ and $\Omega_{b,0}$ are the density parameters of photon and baryon respectively. The quantities are going to be fixed for the analysis as $\Omega_{b,0}h^2 = 0.0224$ and $\Omega_{\gamma,0}h^2 = 2.469 \times 10^{-5}$ in agreement with Planck 2018 (Aghanim et al., 2020b). The radius $r_s$ of the sound horizon at last scattering can be calculated using the distance that the wave can travel from the origin of the universe $t = 0, z \to \infty$ to time $t_d, z_d$ at the drag epoch when photons can no longer prevent the gravitational interaction of baryons and that is why the integral (3.10) is calculated (Perivolaropoulos and Skara, 2022).

The considered BAO data comes from different independent surveys:

1. *The result obtained from the Six-degree Field Galaxy Survey measurement (6dFGS) at redshift* $z = 0.106$ *(Beutler et al., 2011).* The 6dFGS is a survey of 136,304 extragalactic sources that covers almost the entire southern sky up to redshift $z = 0.92$ (Jones et al., 2009). From a subsample of 75,117 galaxies at redshift $z = 0.106$ a two-point correlation function is calculated to estimate the BAO signal at these scales, using the Hubble parameter $H(z)$ and the angular diameter distance $D_A(z)$. Performing analyses to the data points between $10h^{-1}$ Mpc and $190h^{-1}$ Mpc the best fit of the $D_V(z) = 456 \pm 27$ Mpc is obtained. Although, the constant $r_s(z_d)/D_V(z)$ is measured and found a result of $0.336 \pm 0.015$. This is the value used in this Thesis.

2. *The result from Sloan Digital Sky Survey (SDSS) Main Galaxy Sample Measurement (MGS) from Data Release 7 (DR7) at redshift* $z = 0.15$ *(Ross et al., 2015).* The Sloan Digital Sky Survey (SDSS) (York et al., 2000) is a project to measure spectroscopic and spectrometric characteristics for extra-galactic sources. Included in the complete survey, there is a flux-limited low-redshift sample known as the Main Galaxy Sample (MGS) that is used to constrain the BAO scale at 4% using the density field finding a consensus at $z = 0.105$. For this sample, the $r_s^{\text{fid}} = 148.69$ Mpc. The results for the volume-averaged distance weighted over the sound horizon at drag epoch was $D_V(z)r_s^{\text{fid}}/r_s(z_d)$ was $664 \pm 25$ Mpc.

3. *The data points from Baryon Acoustic Oscillation from Spectroscopic Survey (BOSS) contained in SDSS DR12 at* $z = 0.38, 0.51, 0.61$ *(Alam et al., 2017).* For this sample, the BAO scale is measured anisotropically in redshift space using the correlation function and the power spectrum. Computing the shift from the BAO peak position and the expected value for a fiducial cosmology gives the angular diameter distance $D_M(z)$. In this case, the fiducial cosmological model $r_s^{\text{fid}} = 147.78$ Mpc. The final results are the ones presented in Table 3.1.

| Measurement | Redshift | Result |
|---|---|---|
| $D_M(z)\left(\frac{r_s^{\rm fid}}{r_s}\right)$ [Mpc] | $z = 0.38$ | 1512.39 |
| $D_M(z)\left(\frac{r_s^{\rm fid}}{r_s}\right)$ [Mpc] | $z = 0.51$ | 1975.22 |
| $D_M(z)\left(\frac{r_s^{\rm fid}}{r_s}\right)$ [Mpc] | $z = 0.61$ | 2306.68 |
| $H(z)\left(\frac{r_s}{r_s^{\rm fid}}\right)$ [km s$^{-1}$ Mpc$^{-1}$] | $z = 0.38$ | 81.2087 |
| $H(z)\left(\frac{r_s}{r_s^{\rm fid}}\right)$ [km s$^{-1}$ Mpc$^{-1}$] | $z = 0.51$ | 90.9029 |
| $H(z)\left(\frac{r_s}{r_s^{\rm fid}}\right)$ [km s$^{-1}$ Mpc$^{-1}$] | $z = 0.61$ | 98.9647 |

Table 3.1: Results from BOSS from SDSS DR12 clustering analysis to obtain the standard rule at different redshifts (Alam et al., 2017).

4. *The data points from Baryon Acoustic Oscillation from Spectroscopic Survey (BOSS) located in SDSS DR14 at* $z = 0.978, 1.23, 1.526, 1.944$ *(Zhao et al., 2019).* Similar to the previous point, this BAO measurement quantifies the space distribution of galaxies at different redshift bins computing the BAO peak position compared to the expected value using a fiducial cosmology. Notice that there slight differences in the computational procedure and the calculated quantity. In this case, the averaged angular distance $D_A(z)$. The results are summarized in table 3.2.

| Measurement | Redshift | Result |
|---|---|---|
| $D_A(z)\left(\frac{r_s^{\rm fid}}{r_s}\right)$ [Mpc] | $z = 0.98$ | 1586.18 |
| $D_A(z)\left(\frac{r_s^{\rm fid}}{r_s}\right)$ [Mpc] | $z = 1.23$ | 1769.08 |
| $D_A(z)\left(\frac{r_s^{\rm fid}}{r_s}\right)$ [Mpc] | $z = 1.52$ | 1768.77 |
| $D_A(z)\left(\frac{r_s^{\rm fid}}{r_s}\right)$ [Mpc] | $z = 1.94$ | 1807.98 |
| $H(z)\left(\frac{r_s}{r_s^{\rm fid}}\right)$ [km s$^{-1}$ Mpc$^{-1}$] | $z = 0.98$ | 113.72 |
| $H(z)\left(\frac{r_s}{r_s^{\rm fid}}\right)$ [km s$^{-1}$ Mpc$^{-1}$] | $z = 1.23$ | 131.44 |
| $H(z)\left(\frac{r_s}{r_s^{\rm fid}}\right)$ [km s$^{-1}$ Mpc$^{-1}$] | $z = 1.52$ | 148.11 |
| $H(z)\left(\frac{r_s}{r_s^{\rm fid}}\right)$ [km s$^{-1}$ Mpc$^{-1}$] | $z = 1.94$ | 172.63 |

Table 3.2: Results from BOSS from SDSS DR14 clustering analysis to obtain the standard rule at different redshifts (Zhao et al., 2019).

Concerning the $\chi^2$ for the BAO sample, the data from both SDSS DR12 and DR14 from BOSS are going to be treated with a $6\times6$ and $8\times8$ covariance matrix, respectively. The data extraction was done with partially overlapped redshift slices (Alam et al., 2017; Zhao et al., 2019) as

$$\chi^2_{\rm BOSS} = -\frac{1}{2}\Big[(y(\Theta)-\phi)^T C^{-1}_{\rm BOSS}(y(\Theta)-\phi)\Big], \tag{3.15}$$

where $\phi$ is the vector where the modeled quantities are represented (see table 3.1 and 3.2) and $y(\Theta)$ is the theoretically calculated equivalent parameter. The rest of the Surveys are going to be considered as usual

$$\chi^2_{\rm SS} = -\frac{1}{2}\sum_i \left[\frac{(y_i - y(\Theta))^2}{\sigma_i^2}\right], \tag{3.16}$$

where $y_i$ is the measured parameter and $y(\Theta)$ is the modeled quantity. For the complete BAO sample, the corresponding $\chi^2_{\rm BAO}$ is

$$\chi^2_{\rm BAO} = \chi^2_{\rm BOSS-DR12} + \chi^2_{\rm BOSS-DR14} + \chi^2_{\rm 6dFGS} + \chi^2_{\rm SDSS-DR7}, \tag{3.17}$$

where all the surveys are included in the $\chi^2$ expression above.

## 3.5 Quasars

The basis for this observable is our current understanding of the Active Galactic Nuclei galaxies (AGN) which are one of the most luminous objects in the Universe. The term refers to the existence of an energetic source that cannot be attributed directly to stellar activity (Peterson, 1997) in the core region of galaxies. Nowadays, an AGN is defined as a galaxy containing a massive $M > 10^5 M_\odot$ accreting black hole (BH) with several components (Netzer, 2015):

- Rotational dominated accretion flow usually labeled simply as *accretion disk*.
- High-density gas clouds moving in orbits around the black hole between a tenth to a parsec (pc) known as *Broad Line Region* (BLR) whose luminosity depends on their accretion rate.
- Low-density gas clouds moving in orbits farther away from the black hole known as *Narrow Line Region* (NLR).
- Disk and dusty structure up to 10 pc away from the BH simply known as *torus*.
- A thin molecular disk and finally,in around one thousand of the objects, a *jet* associated with higher energy emission.

The study of AGNs has been influenced by the history in which they have been discovered. In the '60s, the compilation of the third Cambridge Catalogue (3C) discovered a large number of galaxies that were highly emitting in radio and in optical images appeared to be blue stars (Beckmann and Shrader, 2012). This led to the fact that similar objects were labeled as *Quasi Stellar Objects* (QSO) or Quasars. This is one of the two largest subclasses of AGNs and the distinction of different categories is only a matter of the historical and observational properties.

Quasars have the following observational features (Peterson, 1997): *(i)* High emission in UV and radio, *(ii)* broad emission lines, *(iii)* large cover in redshift, and *(iv)* variable flux in time in all wavelengths. However, Quasars properties have to be analyzed by their broad *Spectral Energy Distribution* (SED). The UV and optical spectra of Quasars can be distinguished by strong and broad emission lines in particular the hydrogen Balmer-series lines, hydrogen Ly$\alpha$ and ions like Mg II and C IV, whose emergence depends heavily in the redshift of the object (Beckmann and

Shrader, 2012). Other objects in the AGN family are the Seyfert galaxies, radio galaxies, Blazars and several others that depend on their physical features (Padovani et al., 2017).

The differences between the several groups of AGN can be explained by the *standard model*, where was proposed to describe all observational properties in one framework being a small number of physical parameters depending on diverse factors, e.g. accretion rate, change of line of sight, and size dust absorption (Netzer, 2015).

The basic mechanism for this unified model is the accretion occurring near the BH: matter falling into a compact object leading to conversion between mass and gravitational potential energy into electromagnetic energy (Beckmann and Shrader, 2012; Peterson, 1997). Intrinsically, the light Quasars are variable objects. However, at the highest accretion rates (meaured using the $L_{\rm Edd}$ for a Massive Black Hole) the luminosity can be considered constant or *saturated*. This is despite the possible variations in the accretion rate. So, this result is important for its cosmological use as one of the approaches for observables is through the standard candles rule. In such a case, we will rely on the use of Eddington's luminosity (Dultzin et al., 2020) defined by accretion parameters.

Our interest in using Quasars to constrain the cosmological models derived from extended theories of gravity, resides in the fact that its high luminosity could help us reach up to $z \sim 7$ in the Hubble diagram, e.g. as the analyses in (Banados et al., 2021, 2018). This is a redshift that SNIa and Cosmic Chronometers have not reached yet and where we could start to see deviations in the physical conditions that would allow us to explore different cosmologies.

As we described above, we are going to focus on two samples of QSO:

- **Extreme Acretors (xA) sample.** The fundamental criteria to do a selection of Quasars for this sample is that these objects feature in their spectrum lots of different lines, profiles, and intensities that come from multiple ionic species (Dultzin et al., 2020). These varieties of observational properties could be a hint of highly dynamic physical conditions that are producing the phenomena we are seeing and could be chosen to provide a link to physical relations. To obtain a luminosity related to the BH mass via the $L - M_{\rm BH}$ relation (Marziani and Sulentic, 2014), we can find a model-independent luminosity with an estimation of the cosmological distance modulus $\mu(z)$. The method employed is the quasar optical Eigenvector 1, which is composed of two fundamental properties: *(i)* the parameter $R_{\rm Fe\,II}$ that is defined as the ratio between the integrated flux of Fe II$\lambda$4570 blend of multiplets (which means we have a lot of very close lines in the spectra) and *(ii)* the H$\beta$ broad component. This means that the parameter can be written as (Marziani et al., 2018)

$$R_{\rm Fe\,II} = \frac{\rm I(Fe\,II\lambda 4570)}{\rm I(H\beta)}, \tag{3.18}$$

  where I denote the intensity of each line in the spectra. According to (Marziani and Sulentic, 2014) the 4DE1 parameters measure the:

  1. FWHM H$\beta$: The dispersion in low ionization broad-line region (BLR) gas velocity and, therefore, can be used as a virial estimator for low $z$ objects. This is a fundamental parameter in the Quasar study because is linked to the orientation angle compared to our sight of the vision, the BH mass, and the Eddington radio.

2. $R_{\rm Fe\,II}$: Measure the intensity ratio between the Fe emission and the H$\beta$ and it is more likely to be driven by the numerical density of hydrogen $n_{\rm H}$, ionization and metallicity. The ratios can be used even though Fe II emission maintains the same relative intensity, with respect to H$\beta$ changes from object to object.
3. $\Gamma_{\rm soft}$: Excess of soft X-ray can be seen as a thermal indication of accretion in BH systems.
4. C IV$\lambda$1549: Radial motions in high ionization BLR gas driven by accretion phenomena very near the center of the Quasar.

The first two observed characteristics of the 4DE1 formalism are usually presented in the so-called optical plane (Dultzin et al., 2020). The distribution of the data in this plane traces the main sequence of quasars, and if we define a grid of bins with size $\Delta R_{\rm Fe\,II} = 0.5$ in one axis, and in the other in terms of increasing $\Delta$FWHM= 4000 km s$^{-1}$ we found distinctive populations of objects. The sources that belong to the same group show similar spectroscopic characteristics for cosmological use. In this case, we are interested in one particular group: Population A. On one hand, Population A shows FWHM H$\beta < 4000$ km s$^{-1}$, a stronger $R_{\rm Fe\,II}$, a soft X-ray excess and C IV$\lambda$1549 with blue asymmetry (Marziani and Sulentic, 2014). On the other hand, Population B shows FWHM H$\beta > 400$ km s$^{-1}$ with weaker $R_{\rm Fe\,II}$ with no X-ray excess and no indications of asymmetry or blueshift in C IV$\lambda$1549. The whole previous analysis is valid for objects with $z < 1.0$ where the spectra components are visible in the visible spectrum. The problem comes with objects where infrared is not available (Marziani and Sulentic, 2014), in such cases we need to find another candidate to measure the 4DE1 formalism. One alternative is the high-$z$ selector that contains the blend of Al III $\lambda$1860, Si III] $\lambda$1892 and C III] $\lambda$1909 that contains same the physical conditions that the Fe blend measures in optical spectra.

The selection criteria for xA objects will be denoted by two UV line ratios:

(i). Al III $\lambda$1860 / Si III] $\lambda$1892 $\geq 0.5$, and

(ii). Si III] $\lambda$1892 / C III] $\lambda$1909 $\geq 1.0$.

For the objects in the sample with $z > 1$, the selection criteria were the mentioned quotients. The conditions satisfied for xA objects are the following (Dultzin et al., 2020):

(a) Constant highly Eddington ratio $L/L_{\rm Edd} = \lambda_{\rm Edd} \lesssim 1$, which means xA objects radiate near to the Eddington limit.

(b) Virial motion of the BLR. We can express the BH mass as a virial relation

$$M_{\rm BH} = \frac{r_{\rm BLR}(\delta v)^2}{G}, \tag{3.19}$$

where $G$ is the gravitational constant.

(c) The ionization parameter $U$ can be written as

$$U = \frac{Q({\rm H})}{4\pi r_{\rm BLR}^2 n_{\rm H} c} \propto \frac{L}{r^2 n_{\rm H}}, \tag{3.20}$$

where $Q$(H) is the number of hydrogen ionizing photons.

The mentioned luminosity-BH mass ratio relation can be expressed in combination with the necessary conditions for xA objects as

$$\frac{L}{M} \approx 10^{4.53}\lambda_{\rm Edd}\left(\frac{L}{M_{\rm BH}}\right)_{\odot} \approx 10^{4.81}\lambda_{\rm Edd}\ {\rm erg\ s^{-1}\ g^{-1}}, \tag{3.21}$$

where $M_{\rm BH}$ is the BH mass and $L$ the luminosity. This luminosity can be rewritten as

$$L \approx \xi\lambda_{\rm Edd}M \approx \xi\lambda_{\rm Edd}f_s\frac{r_{\rm BLR}(\delta v)^2}{G}, \tag{3.22}$$

using $f_s$ as a structure factor (Marziani and Sulentic, 2014), $\delta v$ the virial velocity dispersion and $r_{\rm BLR}$ the BLR radius. For this analysis the factor $\xi \approx 10^{4.81}$erg s$^{-1}$ g$^{-1}$ (Marziani et al., 2018; Dultzin et al., 2020; Marziani and Sulentic, 2014). The ionization parameter, using spherical symmetry, can be written as

$$U = \frac{\int_{\nu_0}^{\infty}\frac{L_\nu}{h\nu}d\nu}{4\pi n_{\rm H}cr_{\rm BLR}^2}, \tag{3.23}$$

where $L_\mu$ is the luminosity per unit frequency, $h$ is the Planck constant and $\nu_0$ the Rydberg frequency, in addition to $c$ the speed of light, and $n_{\rm H}$ the hydrogen number density. For our analysis, the $r_{\rm BLR}$ can be used as the distance between the source of ionization to the emitting region (Marziani and Sulentic, 2014) – analogous to the reverberation mapping (Peterson et al., 1998)– and we can use another way to estimate this radius as

$$r_{\rm BLR} = \left[\frac{\int_{\nu_0}^{\infty}\frac{L_\nu}{h\nu}d\nu}{4\pi U n_{\rm H}c}\right]^{1/2} = \left(\frac{\kappa L}{2\pi U n_{\rm H}ch\bar{\nu}_i}\right)^{1/2}, \tag{3.24}$$

with $\kappa = 0.5$ and $L_{\rm ion} = \kappa L$. Using the previous relations we finally find an expression for the luminosity that depends on the quantities that we can measure as

$$L \approx 7.8\times10^{44}\frac{\lambda_{\rm Edd}^2\kappa_{0.5}f_{s,2}^2}{h\bar{\nu}_{i,100\rm ev}}\frac{1}{(n_{\rm H}U)_{10^{9.6}}}(\delta v)^4\ {\rm erg\ s^{-1}}. \tag{3.25}$$

Therefore, the normalized virial luminosity relation can be written as

$$L({\rm FWHM}) = 7.88\times10^{44}({\rm FWHM})^4_{1000}, \tag{3.26}$$

where the FWHM is expressed in units of 1000 km/s and using that is related to the virial estimation $\delta v$. Now, using the luminosity we can calculate the distance modulus written as (Negrete et al., 2018)

$$\mu = 2.5[\log L - \log(f_\lambda\lambda)] - 100.19 + 5\log(1+z), \tag{3.27}$$

where we use that $f_\lambda\lambda$ is the rest-frame flux measured in 5100 Å. The mentioned ∼250 points is going to use a $\chi^2$ expressed as

$$\chi^2_{\rm xA} = -\frac{1}{2}\left[\frac{(\mu_i - \mu(z_i,\Theta))^2}{\delta\mu_i^2} + \ln\left(\delta\mu_i^2\right)\right], \tag{3.28}$$

where similar to the $\chi^2$ for the SNIa sample, we will compare the data points distance modulus and the theoretically calculated $\mu(z_i, \Theta)$, using also the error $\delta\mu_i$ for every data point. Most of the data points in this sample are in the redshift range $z < 1$ and in $z \sim 2.5$ due to the characteristics in the spectroscopic analyses as the necessary lines are not visible for all the redshifts in the SDSS ranges of observations.

- **X-UV (nUVX) sample.** The basis of this sample is the non-linear relation between the ultraviolet-measured flux at 2500 Å and the X-ray flux measured at 2 keV to obtain model-independent luminosity distance to contribute to the Hubble diagram at higher redshift than the SNIa limit $z \sim 2$ (Lusso et al., 2020). The objects used to calculate this sample were taken mainly from Sloan Digital Sky Survey (SDSS) DR14 (Pâris et al., 2018). This observable passed through a cross-match with other optical and X-ray surveys including a cross-match between XMM-XXL spectroscopic North Quasar sample (Menzel et al., 2016) and the XMM-Newton source catalog in its DR19 (Webb et al., 2020) to select the objects with the better and most complete observations. The reason behind the relation between the X-ray and the UV measurements is not fully well understood (Lusso et al., 2020), but some possible explanations are the global emission of the accretion disk combined with nuclear emission. More recent studies suggest that this may be about the hot X-ray emitted by the corona of the accretion disk (Risaliti et al., 2023). The attempt to make Quasars sources as standard candles in this approach is to use the relation

$$\log(\mathrm{L_X}) = \beta + \gamma \log(\mathrm{L_X}), \tag{3.29}$$

where the slope $\gamma$ is constant and is the same for every $z$ (Risaliti et al., 2023; Lusso et al., 2020). Meanwhile, the parameter $\beta'$ depends on the source distance and therefore the cosmological distance as

$$\beta = \beta' + (\gamma - 1)\log(4\pi) + 2(\gamma - 1)\log(d_\mathrm{L}). \tag{3.30}$$

The $F_\mathrm{X} - F_\mathrm{UV}$ relation was tested in different redshift intervals to make sure that the relation was correct for every different cosmic epoch, and in every interval, the slope, interception, and dispersion using MCMC techniques (Lusso et al., 2020). The slope and dispersion did not show a correlation with the redshift intervals taken and both of them adjusted very similar values along the calculated intervals. However, at $z > 4$ there was not a clear relation in the values and therefore, to use the high $z$ data we need to use the non-adjusted slope and interception values in the cosmological inference. As the name suggests from the fitted X-ray and UV observable, we will call the sample nUVX from now on. Using the relation for slow redshifts between the X-ray and the UV-flux, we can obtain the Hubble diagram for those objects calculating the luminosity distance as

$$\log d_\mathrm{L} = \frac{[\log F_\mathrm{X} - \gamma F_\mathrm{UV}]}{2(\gamma - 1)} + \beta', \tag{3.31}$$

where $F_\mathrm{X}$ and $F_\mathrm{UV}$ are the measured fluxes densities normalized to the 27.5 in the case of UV. In this example, $d_\mathrm{L}$ is in cm and normalized to 28.5 so this has to be converted if we want to obtain modulus distance compatible with Mpc units. The intercept $\beta'$ is considered

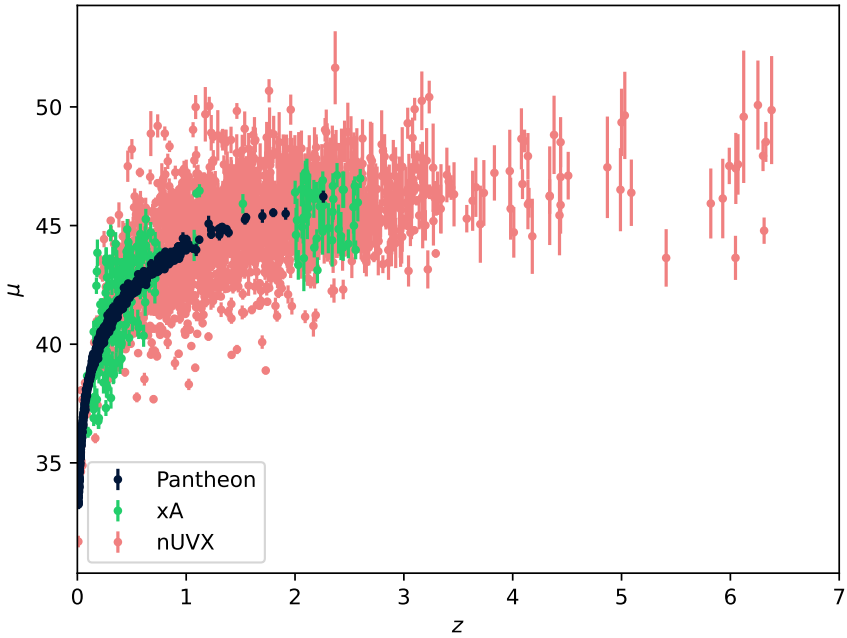


Figure 3.1: Evolution of the $\mu(z)$ and their uncertainties using the xA (green color dots) and nUVX (pink color dots) QSO samples and SNIa Pantheon sample (black color dots).

a free nuisance parameter that will be fitted in posterior analyses. Finally, the $\chi^2$ we will use for the use of this sample is

$$\chi^2_{\rm nUVX} = -\frac{1}{2}\sum_i^N \left( \frac{[y_i - \Psi_i(\Theta)]^2}{s_i^2} - \ln s_i^2 \right), \tag{3.32}$$

where $N$ is the number of data points, $s_i^2 = (\mathrm{d}\log F_{\rm X})^2 + \gamma^2(\mathrm{d}\log F_{\rm UV})^2 + \exp(2\ln\delta)$ with $\delta = 0.21$ and $\gamma = 0.702$ fixed and taking into account data uncertainties.

Finally, $y_i$ is the calculated distance modulus $\mu(z_i, \theta)$ and $y_i$ is the direct measurements calculated as

$$\mu(z_i, \theta) = \frac{5}{2(\gamma - 1)}(\log F_{\rm X} - \gamma F_{\rm UV}) + 5\beta'. \tag{3.33}$$

The use of this data set requires only the calculation of the luminosity distance but will have to take into account the dispersion of the data, and the changes in the relation between the fluxes and their errors.

### 3.5.1 Comment: Quasars in Cosmology

Currently, Quasar samples are gradually becoming important in cosmological model analyses. The most popular sample in literature is the nUVX catalog, which trend deviates from the flat ΛCDM

model in objects higher than $z \sim 3$ in more than $4\sigma$ (Lusso et al., 2019). Doing a follow-up on this result (Bargiacchi et al., 2022), we redo new analyses that are carried out with other cosmological models confirming the existing cosmological tension. A more conservative analysis in this Thesis might suggest that it is also due to the decision to set a value for $H_0$ fixed since the beginning.

In general, the two samples can be seen represented in Figure 3.1, where is clear that the information that they will bring to the analyses is from $z \geq 1$, in which the samples of SNIa are the statistically dominant.

The most recent results obtained using the Quasar nUVX sample have been obtained in (Dainotti et al., 2023), where with an $H_0 = 70$ km s$^{-1}$ Mpc$^{-1}$ fixed the $\Lambda$CDM model is tested through different redshift bins. Meanwhile, in (Bargiacchi et al., 2023) the sample is also explored in combination with other cosmological probes to test calibrations and implications for the geometry in the $\Lambda$CDM context.

- **QSO sample to constraint standard flat cosmologies**: Bargiacchi et al. (2022) analyzed the nUVX QSO sample with SNIa and BAO datasets testing the flat-$\Lambda$CDM model in different combinations with a fixed $H_0 = 70$ km s$^{-1}$ Mpc$^{-1}$. The only free parameter in the analyses is $\Omega_m$ when using the flat $\Lambda$CDM. That is why, additionally dark energy parametrizations are tested including $w$CDM, CPL, JBP, Exponential, and BA. In this framework, some extra parameters are added to the behavior of the dark energy in an attempt to investigate the nature of the late-time cosmic acceleration.

- **QSO sample to constraint standard non-flat cosmologies**: The authors in Du et al. (2023) the standard $\Lambda$CDM model is studied constraining also the curvature component $\Omega_k$ to test the nUVX sample, GRB data detection, and Lensing data. For this analysis, a cosmographic fit is used over the $\Lambda$CDM model, which could be misleading about the promising results regarding the $H_0$ values obtained. In terms of curvature, the QSO sample prefers small negative curvature densities $\Omega_k \leq 0$ in combination with Lensing.

  Again, Bargiacchi et al. (2022) complemented the results for the flat models adding the non-flat versions for $\Lambda$CDM, $w$CDM, and CPL to test the effect of curvature in the combinations of datasets including the nUVX QSO sample. The results are that QSO strongly disagrees with flat the $\Lambda$CDM model at high redshifts at more than $2\sigma$ with a $\Omega_k < 0$.

- **QSO sample to constraint cosmologies from modified theories of gravity**: Shi (2023) performed analyses using the extended covariant $f(Q)$ cosmology using $H(z)$ measurements, SNIa, BAO and a reduced nUVX sample. The results seem promising solving the Hubble tension to $2.5\sigma$ using different affine Connections $\Gamma$ and two different non-metricity models. Just for completeness $f(Q)$ is part of extensions of gravity called *Symmetric Teleparallel Equivalent of GR* (STEGR) in which the gravitational interaction is described by a non-metricity quantity $Q$ without torsion and curvature (Bahamonde et al., 2021). In this case the action used is $S = \int \mathrm{d}^4x\sqrt{-g}f(Q)$(Aggarwal et al., 2022). Using again $f(Q)$ models, the analyses in Aggarwal et al. (2022) the action $S = \int \mathrm{d}^4x\sqrt{-g}[f_1(Q)/2\kappa^2 + f_2(Q)\mathcal{L}_m]$ is tested using $H(z)$ measurements and the nUVX QSO sample fixing $H_0 = 67.76$ km s$^{-1}$ Mpc$^{-1}$.

The clearest disadvantage in all the previous studies is that usually, the QSO samples involve a fixed $H_0$ value. This heavily influences the parameter determination as an expansion parameter is fixed and therefore the fractional densities can not vary as freely in numerical analyses. However,

the fixed $H_0$ value tends to make the numerical codes faster for big samples like the nUVX dataset. In this thesis, we try to remediate the problems with $H_0$ leaving it as a free parameter in all our numerical analyses.

Another of the problems regarding the nUVX QSO sample is the notorious dispersion that is present in the data. In this direction, efforts to better understand the nature of the non-linear relation between the fluxes are being made, including the recalibration of the luminosity distances estimated using other distance determination methods like reverberation mapping (Khadka et al., 2023).

It is important to mention that the previously mentioned analyses did not take into account the xA QSO. We decided to use the two different samples to contrast the physical approaches to construct the Hubble diagram using those objects. This will give this analysis a wider approach than those done using only the nUVX sample. The analyses done in literature so far only include the $\Lambda$CDM model and different dark energy parametrizations, as well as some counted examples of $f(Q)$ test using only the nUVX sample. Accordingly, we decided to use the two samples to perform analyses using the TEGR to test higher redshift regions via the nUVX sample and to explore different approaches to the QSO Hubble diagram.

Finally, according to the mentioned latter studies, our goal is to find better constraints in the local universe for $f(T)$ cosmologies that can help to understand the systematics and the $H_0$ tension.

# Chapter 4

# Constraining $f(T)$ cosmologies: analyses and results

In this Chapter, we present the analyses and results published in (Sandoval-Orozco et al., 2023). The main goal is to explore possible deviations from the standard ΛCDM model that can explain the current $H_0$ tension. To achieve this we use the current local observables described in Chapter 3 and combine them with two new calibrated Quasars (QSO) datasets using ultraviolet, x-ray, and optical plane techniques. As we discussed, these observables can be identified as part of the high-redshift standardizable candels since the main characteristic is based on fluxes distributions calibrated up to $z \sim 7$. This is an advantage, as previous analyses using $f(T)$ cosmologies as Briffa et al. (2022) and Briffa et al. (2023a) uses low redshift data up to $z \sim 2$ with only SNIa samples.

The cosmological models considered for this statistical test were described in Chapter 2, also we will consider five $H_0$ prior scenarios to develop the calibrations for the samples. Our second goal is to find possible estimations that can provide the possibility to relax the $H_0$ tension at $2\sigma$ using these new QSO samples.

Is important to remark that our results can be an initial start for more serious treatments in the quasars physics from ultraviolet, x-ray, and optical plane techniques on local observations as cosmological tests to relax, and even find a solution, to the cosmological tensions issues.

## 4.1 Settings: cosmological priors and baselines

We will use several combinations for the described data sets (see Chapter 3) to compare the $f(T)$ cosmologies and their constraints. We based our analysis on the $\chi^2$-statistics, where the total $\chi^2_{\rm T}$ is the sum of each data set, e.g. $\chi^2_{H(z)+\rm SNIa} = \chi^2_{H(z)} + \chi^2_{\rm SNIa}$, and the same for each data sample.

We will consider the following two groups of baselines:

1. First group baselines:
   - $H(z)$ measurements + Pantheon Supernovae (SNIa).
   - $H(z)$ measurements + SNIa + QSO xA.
   - $H(z)$ measurements + SNIa + QSO nUVX.
2. Second group baselines:

- $H(z)$ measurements + SNIa + BAO.
- $H(z)$ measurements + SNIa + BAO + QSO xA.
- $H(z)$ measurements + SNIa + BAO + QSO nUVX.

The subdivision for the two different Quasar samples is made to compare the different methodologies to obtain them using the 4DE1 formalism and the non-linear relation between UV and X-rays.

Additionally, we will use the following $H_0$ priors:

- R21: $H_0 = 73.3 \pm 1.04$ km s$^{-1}$ Mpc$^{-1}$ from the most recent SH0ES collaboration (Riess et al., 2021b). [Color code: R21]
- P18: $H_0 = 67.36 \pm 0.54$ km s$^{-1}$ Mpc$^{-1}$ from the results from the Planck Space Telescope (Aghanim et al., 2020b) using TT+TE+EE+lowE+Lensing. [Color code: P18]
- GD3: $H_0 = 74.03 \pm 1.42$ km s$^{-1}$ Mpc$^{-1}$ from the EDR3 GAIA Mission (Di Valentino et al., 2021c; Brown et al., 2021). [Color code: GD3]
- F20: $H_0 = 69.8 \pm 0.8$ km s$^{-1}$ Mpc$^{-1}$ from the most recent calibration of the Tip of the Red Giant Branch (Freedman et al., 2020). [Color code: F20]
- ACT: $H_0 = 67.9 \pm 1.5$ km s$^{-1}$ Mpc$^{-1}$ from the latest results of the Atacama Cosmology Telescope (Aiola et al., 2020). [Color code: ACT]

To compare, we will present each model without any assumption on the $H_0$ prior. For the rest of the cosmological parameters, a flat (uninformative) prior represented by $[\theta_{\min}, \theta_{\max}]$ will be used as

$$\mathrm{P}(\theta) = \begin{cases} \frac{1}{\theta_{\max} - \theta_{\min}} & \theta_{\max} \leq \theta \leq \theta_{\min}, \\ 0 & \text{otherwise}, \end{cases} \tag{4.1}$$

in which $\Omega_m \in [0.1, 0.9]$, $M \in [-30, 0]$, $\beta' \in [-20, 20]$ and for the specific parameters for each $f(T)$ model $b_1 \in [-5, 1]$ and $1/b_2, 1/b_3 \in (0, 1]$. The value of $\chi^2_{\min}$ is calculated as using $\chi^2_{\min} = -2 \ln L_{\max}$.

Notice that in our results we remark on the importance of adding BAO survey measurements to the combinations, resulting in a lower value of $H_0$. This result is due to the assumptions of the early universe, similar to what Planck Collaboration results have done, and therefore preferring an $H_0$ much closer to the estimated $H_0 \sim 67$ km s$^{-1}$ Mpc $^{-1}$. This is the reason why we considered using the BAO sample separately from the others in the baselines.

Finally, before showing the results it is important to mention that the absolute magnitude $M$ value is degenerated with $H_0$, and therefore the estimation depends on the priors used on the Hubble parameter.

## 4.2 ΛCDM model

The test on this standard model will provide the perspective of the results obtained through other cosmologies. Furthermore, it will show how the data sets estimate the results with an expected convergence on the MCMC runs that occur faster and result in a Gaussian for almost every

combination. The results using $H(z)$ + SNIa baseline with and without BAO sample are shown in Table 4.1 and in both Figures 4.1.

Notice that the use of $H(z)$ and SNIa samples without a prior gives almost no constraint to $H_0$ resulting in a lower value for $H_0 = 69.6^{+3.0}_{-4.1}$ km s$^{-1}$ Mpc$^{-1}$ but with high uncertainty. Meanwhile, as mentioned above the use of BAO observable, reduces the $H_0$ value to $H_0 = 67.3^{+0.7}_{-0.6}$ km s$^{-1}$ Mpc$^{-1}$, which is consistent with the Planck prior at the expense of using an early universe assumption.

| Data set | $H_0$ [km s$^{-1}$ Mpc$^{-1}$] | $\Omega_m$ | $M$ | $\chi^2_{\rm min}$ |
|---|---|---|---|---|
| $H(z)$ + SNIa | $69.6^{+3.0}_{-4.1}$ | $0.299 \pm 0.021$ | $-19.37^{+0.10}_{-0.12}$ | 949.41 |
| & R21 | $73.1^{+0.7}_{-0.8}$ | $0.289^{+0.020}_{-0.017}$ | $-19.26 \pm 0.02$ | 950.72 |
| & P18 | $67.4 \pm 0.4$ | $0.305^{+0.018}_{-0.020}$ | $-19.43^{+0.02}_{-0.01}$ | 949.65 |
| & F20 | $69.8^{+0.6}_{-0.5}$ | $0.298^{+0.020}_{-0.018}$ | $-19.36 \pm 0.02$ | 949.45 |
| & GD3 | $73.6^{+1.0}_{-0.9}$ | $0.289^{+0.018}_{-0.02}$ | $-19.24 \pm 0.03$ | 951.15 |
| & ACT | $68.0^{+1.0}_{-1.1}$ | $0.301^{+0.021}_{-0.019}$ | $-19.42^{+0.04}_{-0.03}$ | 949.52 |
| $H(z)$ + SNIa + BAO | $67.3^{+0.7}_{-0.6}$ | $0.318 \pm 0.013$ | $-19.43 \pm 0.02$ | 960.30 |
| & R21 | $70.2 \pm 0.5$ | $\left(293.5^{+10.4}_{-9.6}\right) \times 10^{-3}$ | $-19.35 \pm 0.02$ | 995.28 |
| & P18 | $67.4^{+0.3}_{-0.4}$ | $0.317 \pm 0.010$ | $-19.43 \pm 0.01$ | 960.29 |
| & F20 | $68.8^{+0.4}_{-0.5}$ | $\left(305.7^{+9.6}_{-10.3}\right) \times 10^{-3}$ | $-19.38^{+0.01}_{-0.02}$ | 968.01 |
| & GD3 | $69.5 \pm 0.6$ | $\left(299.2^{+10.9}_{-10.0}\right) \times 10^{-3}$ | $-19.37 \pm 0.02$ | 998.59 |
| & ACT | $67.5 \pm 0.6$ | $\left(315.3^{+11.9}_{-9.8}\right) \times 10^{-3}$ | $-19.42 \pm 0.02$ | 960.49 |

Table 4.1: ΛCDM model constraints for the combinations of $H(z)$ measurements, Pantheon SNIa compilation and BAO catalogs. At the top of the table are the results without the BAO sample, while at the bottom are the results including this latter sample with different results corresponding to the priors imposed on $H_0$. The color codes are indicated in the description for each before consideration.

Using $H(z)$ + SNIa baseline the highest value for $H_0$ is the one obtained with the GD3 prior $H_0 = 73.6^{+1.0}_{-0.9}$ km s$^{-1}$ Mpc$^{-1}$, also this is the lowest estimation for the fractional matter density at $\Omega_m = 0.289^{+0.018}_{-0.020}$. Similar to the one obtained using the R21 prior, where the lowest value for $H_0$ is given using the P18 prior with $H_0 = 67.4 \pm 0.4$ km s$^{-1}$ Mpc$^{-1}$ with the highest $\Omega_m = 0.305^{+0.018}_{-0.020}$. As mentioned, the introduction of the BAO sample modifies the result in lowering the $H_0$ value for example to $H_0 = 70.2 \pm 0.5$ km s$^{-1}$ Mpc$^{-1}$. Using the R21 prior leads to the lowest estimation in $\Omega_m \approx 0.293$, which means that all the estimations for $H_0$ are lower than this value. Even the estimation using the GD3 prior gives $H_0 = 69.5 \pm 0.6$ probably due to the higher error compared to the R21 prior. Both ACT and P18 priors behave similarly for the values of $\Omega_m$ and $H_0$. Meanwhile, F20 prior preferrs some *intermediate* values as $H_0 = 69.8^{+0.6}_{-0.5}$ km s$^{-1}$ Mpc$^{-1}$.

It is important to notice that using this combination of data sets the value for $H_0$ is not reduced, except when using the BAO sample which is not a surprise considering the early universe assumptions.

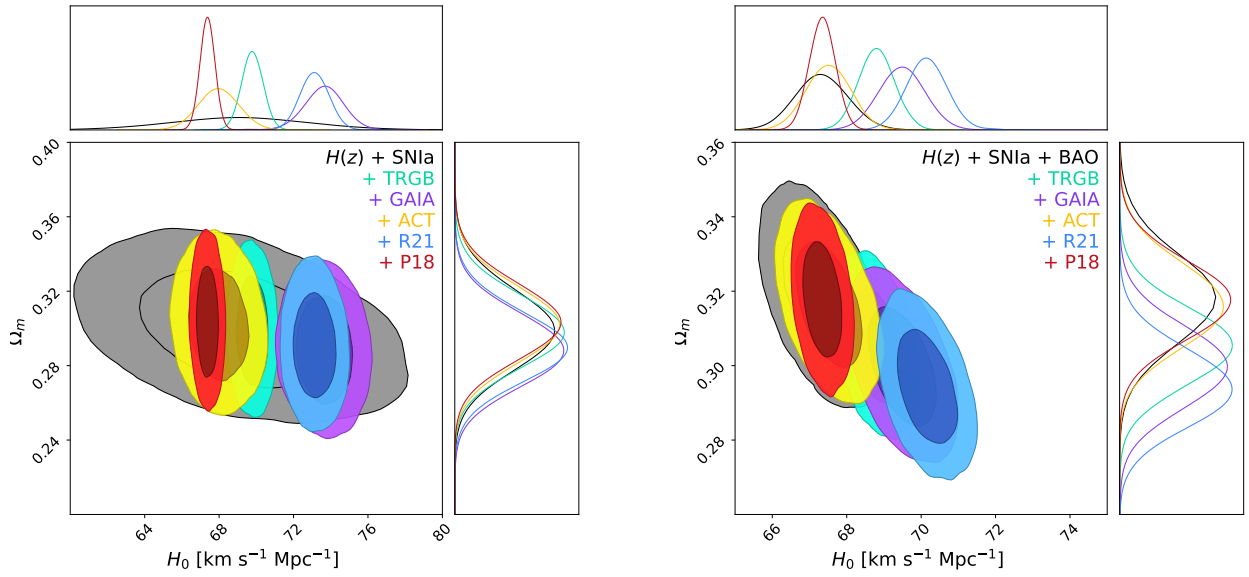


(a) (b)

Figure 4.1: C.L posterior results for the *(a)* $H(z)$ and SNIa Pantheon compilation. *(b)* Combination including the BAO sample. The shadowed regions correspond to $1\sigma$ and $2\sigma$, respectively. We use the color code blue for R21 prior, purple for GAIA, red for P18, green for F20, and yellow for ACT. Additionally, the model that was tested with flat prior is represented in black color.

The first improvements for the ΛCDM model are shown using the xA quasar sample. This can be seen in both Figures 4.2 and in Table 4.2. Using the $H(z)$ + SNIa + xA baseline without prior results in a $H_0$ consistent with the P18 prior and with the Planck results as $H_0 = 67.4 \pm 1.0$ km s$^{-1}$ Mpc$^{-1}$. However, this result gives a higher uncertainty. Adding the BAO sample to this combination maintains the value of $H_0 = 67.2^{+0.6}_{-0.5}$ km s$^{-1}$ Mpc$^{-1}$. This means that only adding the xA sample can result in a diminution of the Hubble tension down to $2\sigma$. This has consequences also in the use of other priors, e.g. R21 and GD3, which reduces the value to $H_0 = 71.2 \pm 0.6$ km s$^{-1}$ Mpc$^{-1}$, and $H_0 = 70.6 \pm 0.7$ km s$^{-1}$ Mpc$^{-1}$, respectively. Using the combination without the BAO sample the values go lower to $2\sigma$ for the P18 prior. Similar effects to the previous results occur in the fractional matter density for the results as $\Omega_m$ tends to be higher for the lower values of $H_0$, fulfilling the physical Friedmann constraint equation.

| Data set | $H_0$ [km s$^{-1}$ Mpc$^{-1}$] | $\Omega_m$ | $M$ | $\chi^2_{\rm min}$ |
|---|---|---|---|---|
| $H(z)$ + SNIa + xA | $67.4 \pm 1.0$ | $0.299 \pm 0.021$ | $-19.43 \pm 0.03$ | 2616.59 |
| & R21 | $71.2 \pm 0.6$ | $0.265^{+0.016}_{-0.015}$ | $-19.33 \pm 0.02$ | 2639.99 |
| & P18 | $67.4^{+0.3}_{-0.4}$ | $0.299^{+0.018}_{-0.017}$ | $-19.43 \pm 0.01$ | 2617.00 |
| & F20 | $69.2 \pm 0.5$ | $0.283^{+0.016}_{-0.017}$ | $-19.38 \pm 0.02$ | 2621.45 |
| & GD3 | $70.6 \pm 0.7$ | $0.269^{+0.019}_{-0.017}$ | $-19.34 \pm 0.02$ | 2639.22 |
| & ACT | $67.6 \pm 0.7$ | $0.297^{+0.018}_{-0.019}$ | $-19.42 \pm 0.02$ | 2617.09 |
| $H(z)$ + SNIa + BAO + xA | $67.2^{+0.6}_{-0.5}$ | $0.316^{+0.012}_{-0.010}$ | $-19.43 \pm 0.02$ | 2628.24 |
| & R21 | $69.6 \pm 0.5$ | $\left(292.5^{+11.2}_{-9.7}\right) \times 10^{-3}$ | $-19.37^{+0.02}_{-0.01}$ | 2670.17 |
| & P18 | $67.3^{+0.4}_{-0.3}$ | $\left(315.2^{+10.0}_{-9.8}\right) \times 10^{-3}$ | $-19.43 \pm 0.01$ | 2628.27 |
| & F20 | $68.6^{+0.4}_{-0.5}$ | $\left(303.7^{+9.2}_{-10.3}\right) \times 10^{-3}$ | $-19.39^{+0.01}_{-0.02}$ | 2638.32 |
| & GD3 | $69.0^{+0.5}_{-0.6}$ | $\left(298.1^{+11.4}_{-9.0}\right) \times 10^{-3}$ | $-19.38 \pm 0.02$ | 2662.63 |
| & ACT | $67.4 \pm 0.5$ | $0.314^{+0.011}_{-0.010}$ | $-19.43 \pm 0.02$ | 2628.53 |

Table 4.2: ΛCDM model constraints for the combination $H(z)$ measurements, SNIa compilation, and with both BAO surveys. We include the QSO xA sample.

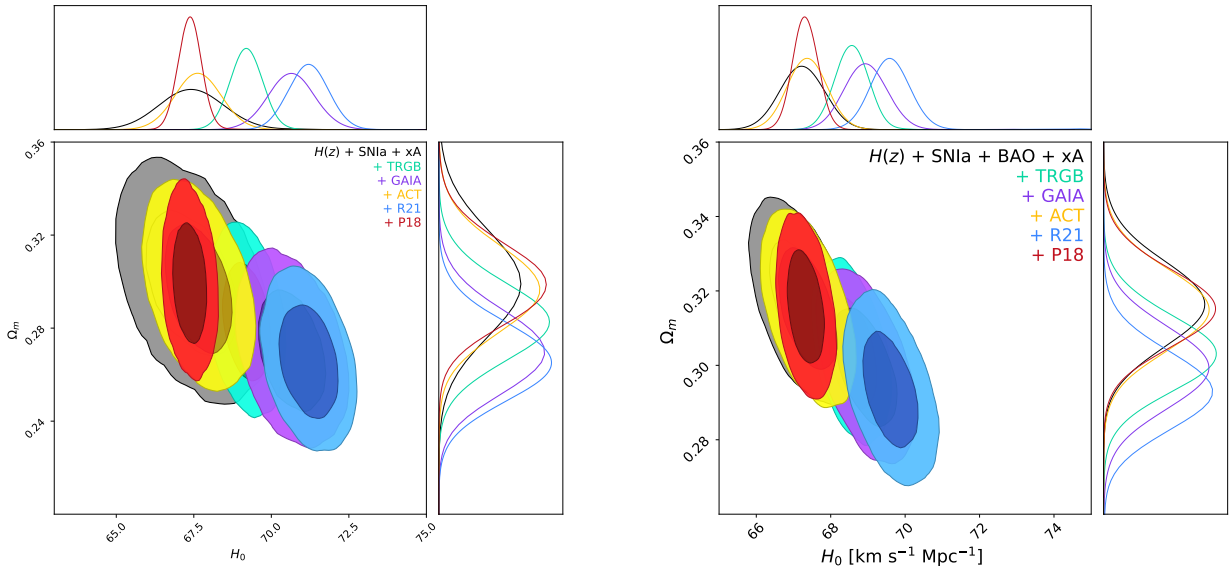


(a) (b)

Figure 4.2: C.L posterior results for the *(a)* $H(z)$ and SNIa Pantheon compilation with the QSO xA sample, and *(b)* the combination including the BAO sample. The shadowed regions correspond to $1\sigma$ and $2\sigma$, respectively. We use the color code blue for R21 prior, purple for GAIA, red for P18, green for F20, and yellow for ACT. Additionally, the model that was tested with flat prior is represented in black color.

| Data set | $H_0$ [km s$^{-1}$ Mpc$^{-1}$] | $\Omega_m$ | $M$ | $\beta'$ | $\chi^2_{\rm min}$ |
|---|---|---|---|---|---|
| $H(z)$ + SNIa + nUVX | $69.0^{+3.6}_{-3.5}$ | $0.300^{+0.020}_{-0.022}$ | $-19.37 \pm 0.11$ | $-11.42^{+6.6}_{-7.7}$ | 2993.82 |
| & R21 | $73.2^{+0.7}_{-0.8}$ | $0.308 \pm 0.011$ | $-19.25 \pm 0.02$ | $-11.429^{+0.095}_{-0.094}$ | 3044.75 |
| & P18 | $67.4 \pm 0.4$ | $0.309 \pm 0.011$ | $-19.43 \pm 0.01$ | $-11.39^{+0.15}_{-0.16}$ | 3068.76 |
| & F20 | $69.7^{+0.7}_{-0.5}$ | $\left(308.5^{+10.0}_{-9.9}\right) \times 10^{-3}$ | $-19.35 \pm 0.02$ | $-11.40 \pm 0.14$ | 3067.97 |
| & GD3 | $73.5^{+2.2}_{-2.0}$ | $0.307 \pm 0.012$ | $-19.24 \pm 0.06$ | $-11.42 \pm 0.12$ | 3047.23 |
| & ACT | $67.9^{+1.6}_{-1.4}$ | $0.308 \pm 0.011$ | $-19.41 \pm 0.05$ | $-11.40 \pm 0.12$ | 3068.20 |
| $H(z)$ + SNIa + BAO + nUVX | $67.3 \pm 0.7$ | $0.317^{+0.012}_{-0.011}$ | $-19.43 \pm 0.02$ | $-11.03^{+1.69}_{-1.75}$ | 3117.92 |
| & R21 | $70.2 \pm 0.5$ | $\left(293.8^{+9.9}_{-9.8}\right) \times 10^{-3}$ | $-19.35 \pm 0.02$ | $-11.46 \pm 1.78$ | 3152.89 |
| & P18 | $67.3 \pm 0.3$ | $\left(318.1^{+9.7}_{-10.9}\right) \times 10^{-3}$ | $-19.43 \pm 0.01$ | $-11.12^{+1.54}_{-1.91}$ | 3117.91 |
| & F20 | $68.8^{+0.5}_{-0.4}$ | $\left(305.4^{+9.7}_{-10.3}\right) \times 10^{-3}$ | $-19.384^{+0.013}_{-0.014}$ | $-11.46^{+1.62}_{-1.77}$ | 3125.63 |
| & GD3 | $69.5 \pm 0.6$ | $0.299 \pm 0.010$ | $-19.37 \pm 0.02$ | $-11.49^{+1.77}_{-1.65}$ | 3148.20 |
| & ACT | $67.5 \pm 0.6$ | $0.317^{+0.010}_{-0.012}$ | $-19.42 \pm 0.02$ | $-11.47^{+1.64}_{-1.86}$ | 3118.18 |

Table 4.3: ΛCDM model constraints for the baseline $H(z)$ measurements, SNIa compilation, and BAO sample. We include the QSO nUVX sample.

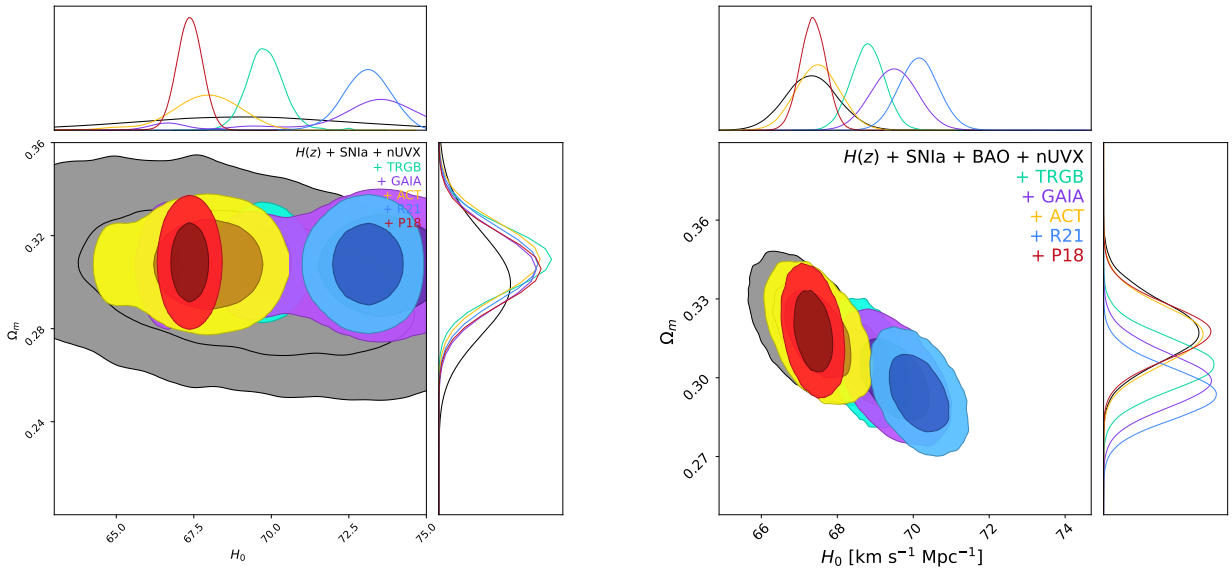


(a) (b)

Figure 4.3: C.L posterior results for the combinations *(a)* $H(z)$ and SNIa Pantheon compilation with the QSO nUVX sample, and *(b)* the combination with the BAO sample. The shadowed regions correspond to $1\sigma$ and $2\sigma$, respectively. We use the color code blue for R21 prior, purple for GAIA, red for P18, green for F20, and yellow for ACT. Additionally, the model that was tested with flat prior is represented in black color.

Finally, using the QSO nUVX sample gives interesting results that can be seen in Table 4.3 and in both figures 4.3. In the baseline $H(z)$ + SNIa + nUVX without any prior, $H_0 = 69.0^{+3.6}_{-3.5}$ km s$^{-1}$ Mpc$^{-1}$ clearly shows a diminution in the Hubble tension up to $3\sigma$, but with a higher uncertainty. In

this combination, the highest $H_0$ estimation occurs using the GD3 prior $H_0 = 73.5^{+2.2}_{-2.0}$, along with the lowest estimation of the fractional matter density $\Omega_m = 0.307 \pm 0.012$. this is in concordance with the R21 prior and as we have seen before, the expected result using a late-time $H_0$ estimation as a prior. However, using P18 and ACT result in the lowest $H_0$ estimation and the highest $\Omega_m$ values as $H_0 = 67.4 \pm 0.4$ km s$^{-1}$ Mpc$^{-1}$ for P18. The use of the BAO sample as mentioned above results in the diminution of the estimation of $H_0$, and in this case the highest estimation is the one obtained using the R21 prior as $H_0 = 70.2 \pm 0.5$ km s$^{-1}$ Mpc$^{-1}$, and the lowest estimation of $\Omega_m = 0.308 \pm 0.011$. The GD3 prior gives a lower estimation due to the larger uncertainty in the prior. The prior F20, as in the previous samples, tends to maintain an intermediate estimate between the previous P18 and R21 as $H_0 = 68.8^{+0.5}_{-0.4}$ km s$^{-1}$ Mpc$^{-1}$. In this sample, the additional parameter $\beta'$ seems to be exhibiting an almost constant behavior between $\beta' = -11$ and $\beta' = -12$, as is the zero-point flux for this quasar sample.

In the case of the ΛCDM model, as seen in the Tables 4.1, 4.2, 4.3 the value of the $\chi^2_{\rm min}$ is low and close to the dataset size. For the combination of $H(z)$ and SNIa the value is lower than the combination using the BAO results with a consistent result independently from the prior used. On the contrary, the use of the xA sample appears to add dispersion in the calculation of $\chi^2_{\rm min}$ as the numerical value is higher than the dataset size. This is not present in the nUVX analyses where the $\chi^2_{\rm min}$ is closer to the dataset size, and consistent independently from the prior imposed.

## 4.3 Power law model

For the power law model $f_1(T)$, the results are quite similar to those obtained for the ΛCDM model. The use of BAO measurements influences the results in a lower value $H_0$. In this direction, using the combinations with $H(z)$, SNIa and BAO measurements without any prior we obtain a result of $H_0 = 67.8^{+0.9}_{-1.0}$ km s$^{-1}$ Mpc$^{-1}$, which is consistent also with the P18 prior, and a free parameter from this model gives $b_1 = -0.06^{+0.12}_{-0.17}$, which is near to $b_1 = 0$. This case recovers the standard cosmological model ΛCDM. This is in contrast to the case using only $H(z)$ and SNIa where $b_1 = -0.41^{+0.59}_{-0.61}$, this result deviates from the ΛCDM model but still is at $2\sigma$ C.L from within the observations. Regarding the use of priors, the late universe measurements from R21 and GD3 result in a model closer to ΛCDM using the combination without BAO. While the introduction of the BAO sample results in deviations from the standard model with more than $2\sigma$, that is $b_1 = -0.52^{+0.16}_{-0.21}$ for R21, and $b_1 = -0.46^{+0.17}_{-0.20}$ for GD3. For the early universe inferences of $H_0$, e.g. P18 and ACT, the combination of $H(z)$, SNIa with BAO measurements results in $b_1 \to 0$ at $2\sigma$ with $b_1 = -0.05^{+0.10}_{-0.11}$ for P18 prior, and $b_1 = -0.09^{+0.12}_{-0.15}$ for ACT prior.

| Data set | $H_0$ [km s$^{-1}$ Mpc$^{-1}$] | $\Omega_m$ | $b_1$ | $M$ | $\chi^2_{\rm min}$ |
|---|---|---|---|---|---|
| $H(z)$ + SNIa | $68.1^{+3.6}_{-4.1}$ | $0.370^{+0.051}_{-0.068}$ | $-0.41^{+0.59}_{-0.61}$ | $-19.41^{+0.11}_{-0.13}$ | 949.01 |
| & R21 | $73.0^{+0.8}_{-0.7}$ | $0.322^{+0.054}_{-0.063}$ | $-0.08^{+0.45}_{-0.52}$ | $-19.26^{+0.02}_{-0.03}$ | 950.70 |
| & P18 | $67.4 \pm 0.4$ | $0.371^{+0.042}_{-0.059}$ | $-0.42^{+0.52}_{-0.59}$ | $-19.44 \pm 0.02$ | 949.05 |
| & F20 | $69.8^{+0.5}_{-0.6}$ | $0.348^{+0.048}_{-0.056}$ | $-0.27^{+0.47}_{-0.54}$ | $-19.36 \pm 0.02$ | 949.19 |
| & GD3 | $73.8^{+0.9}_{-1.1}$ | $0.327^{+0.046}_{-0.075}$ | $-0.07^{+0.47}_{-0.49}$ | $-19.25 \pm 0.03$ | 951.15 |
| & ACT | $67.9^{+1.0}_{-1.1}$ | $0.365^{+0.045}_{-0.055}$ | $-0.32^{+0.41}_{-0.68}$ | $-19.42 \pm 0.04$ | 949.01 |
| $H(z)$ + SNIa + BAO | $67.8^{+0.9}_{-1.0}$ | $0.321^{+0.011}_{-0.013}$ | $-0.06^{+0.12}_{-0.17}$ | $-19.42 \pm 0.02$ | 959.98 |
| & R21 | $71.3 \pm 0.6$ | $0.315 \pm 0.011$ | $-0.52^{+0.16}_{-0.21}$ | $-19.34 \pm 0.02$ | 981.26 |
| & P18 | $67.4 \pm 0.4$ | $0.322^{+0.012}_{-0.013}$ | $-0.05^{+0.10}_{-0.11}$ | $-19.43 \pm 0.01$ | 960.0 |
| & F20 | $69.8^{+0.5}_{-0.6}$ | $0.343^{+0.030}_{-0.033}$ | $-0.21^{+0.24}_{-0.34}$ | $-19.36 \pm 0.02$ | 963.50 |
| & GD3 | $70.8 \pm 0.7$ | $0.315^{+0.012}_{-0.011}$ | $-0.46^{+0.17}_{-0.20}$ | $-19.35 \pm 0.02$ | 980.64 |
| & ACT | $67.9^{+0.6}_{-0.8}$ | $0.321^{+0.013}_{-0.012}$ | $-0.09^{+0.12}_{-0.15}$ | $-19.42 \pm 0.02$ | 959.99 |

Table 4.4: $f_1(T)$ model (2.17) constraints for the combinations of $H(z)$ measurements, Pantheon SNIa compilation and BAO catalogs. At the top of the table are the results without the BAO sample, while at the bottom are the results including this latter sample with different results corresponding to the priors imposed on $H_0$. The color codes are indicated in the description for each prior to consideration.

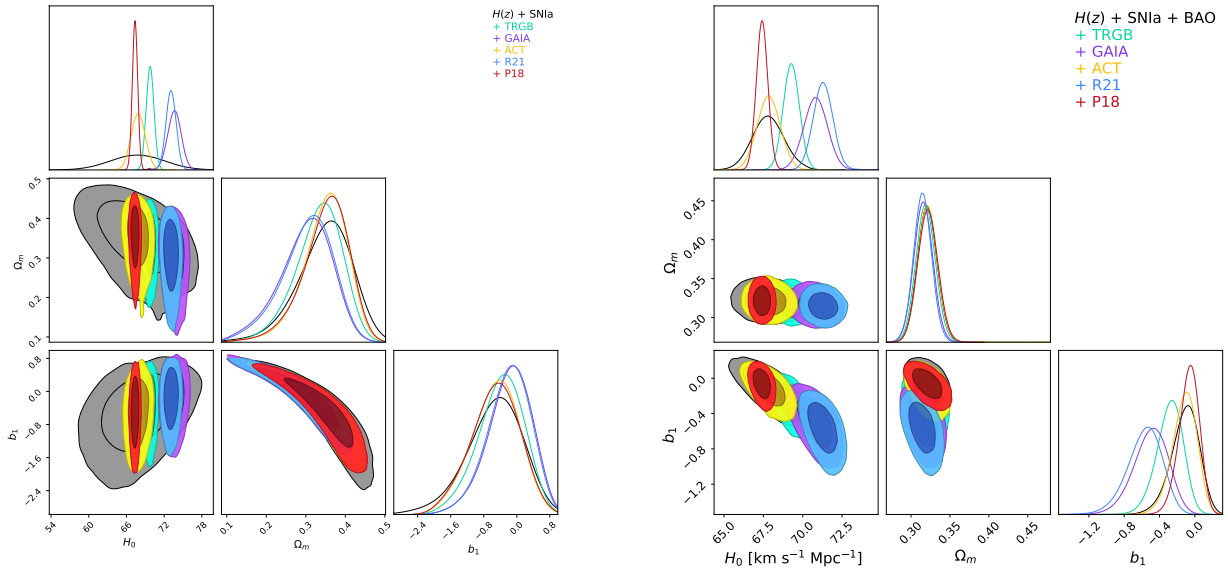


(a) (b)

Figure 4.4: C.L posterior results using $f_1(T)$ model (2.17) for the *(a)* $H(z)$ and SNIa Pantheon compilation. *(b)* Combination including the BAO sample. The shadowed regions correspond to $1\sigma$ and $2\sigma$, respectively. We use the color code blue for R21 prior, purple for GAIA, red for P18, green for F20, and yellow for ACT. Additionally, the model that was tested with flat prior is represented in black color.

| Data set | $H_0$ [km s$^{-1}$ Mpc$^{-1}$] | $\Omega_m$ | $b_1$ | $M$ | $\chi^2_{\rm min}$ |
|---|---|---|---|---|---|
| $H(z)$ + SNIa + xA | $68.1 \pm 1.0$ | $0.405^{+0.027}_{-0.028}$ | $-1.43^{+0.49}_{-0.77}$ | $-19.44 \pm 0.03$ | 2606.16 |
| & R21 | $71.4 \pm 0.6$ | $0.387^{+0.024}_{-0.026}$ | $-1.97^{+0.69}_{-0.79}$ | $-19.35 \pm 0.02$ | 2624.62 |
| & P18 | $67.5^{+0.3}_{-0.4}$ | $0.411^{+0.024}_{-0.030}$ | $-1.45^{+0.54}_{-0.69}$ | $-19.453^{+0.02}_{-0.01}$ | 2606.55 |
| & F20 | $69.4 \pm 0.5$ | $0.399^{+0.025}_{-0.027}$ | $-1.73^{+0.64}_{-0.71}$ | $-19.40 \pm 0.02$ | 2608.69 |
| & GD3 | $71.0 \pm 0.7$ | $0.389 \pm 0.025$ | $-1.88^{+0.62}_{-0.82}$ | $-19.36 \pm 0.02$ | 2624.50 |
| & ACT | $68.0 \pm 0.7$ | $0.407^{+0.026}_{-0.029}$ | $-1.58^{+0.62}_{-0.65}$ | $-19.44 \pm 0.02$ | 2606.18 |
| $H(z)$ + SNIa + BAO + xA | $68.3^{+0.8}_{-0.9}$ | $0.324^{+0.014}_{-0.013}$ | $-0.23^{+0.15}_{-0.21}$ | $-19.41 \pm 0.02$ | 2625.79 |
| & R21 | $71.0 \pm 0.6$ | $0.320 \pm 0.011$ | $-0.72^{+0.19}_{-0.26}$ | $-19.35 \pm 0.01$ | 2648.17 |
| & P18 | $67.5^{+0.3}_{-0.4}$ | $0.325^{+0.013}_{-0.012}$ | $-0.15^{+0.12}_{-0.13}$ | $-19.43 \pm 0.01$ | 2626.52 |
| & F20 | $69.3 \pm 0.5$ | $0.322^{+0.016}_{-0.014}$ | $-0.41^{+0.16}_{-0.19}$ | $-19.39 \pm 0.01$ | 2628.70 |
| & GD3 | $70.5^{+0.6}_{-0.7}$ | $0.322^{+0.011}_{-0.012}$ | $-0.65^{+0.22}_{-0.23}$ | $-19.36 \pm 0.02$ | 2646.78 |
| & ACT | $68.1 \pm 0.7$ | $0.326^{+0.011}_{-0.013}$ | $-0.23^{+0.15}_{-0.17}$ | $-19.412 \pm 0.02$ | 2625.81 |

Table 4.5: $f_1(T)$ model (2.17) constraints for the combination $H(z)$ measurements, SNIa compilation, and with both BAO surveys. We include the QSO xA sample.

Constraining this model with the xA sample has the consequence of raising the value of the fractional matter density $\Omega_m$, and lowering the $H_0$ value. For example, considering the R21 prior

we obtain $H_0 = 71.4 \pm 0.6$ km s$^{-1}$ Mpc$^{-1}$, $\Omega_m = 0.387^{+0.024}_{-0.026}$, and $b_1 = -1.97^{+0.69}_{-0.79}$. These results show a difference of more than $2\sigma$ in comparison to $\Lambda$CDM. This behavior gets relaxed when using the BAO data, from where we obtain $H_0 = 71.0 \pm 0.6$ km s$^{-1}$ Mpc$^{-1}$, $\Omega_m = 0.320 \pm 0.011$, and $b_1 = -0.72^{+0.19}_{-0.26}$ by using the R21 prior. However, these constraints still are not consistent with $\Lambda$CDM within $2\sigma$.

In the case when we select the P18 prior, with and without the BAO sample, the $H_0$ constraints are similar to the latter, and the free parameter $b_1$ approaches to $\Lambda$CDM using only the BAO data with $H_0 = 67.5^{+0.3}_{-0.4}$ km s$^{-1}$ Mpc$^{-1}$ and $b_1 = -0.15^{+0.12}_{-0.13}$. We obtain $b_1 = -1.45^{+0.54}_{-0.69}$ without this observable. Similar things happen using ACT and F20 priors, clearly being the ones using the BAO data closer to $b_1 \to 0$. All the results can be seen in both Table 4.5 and Figure 4.5.

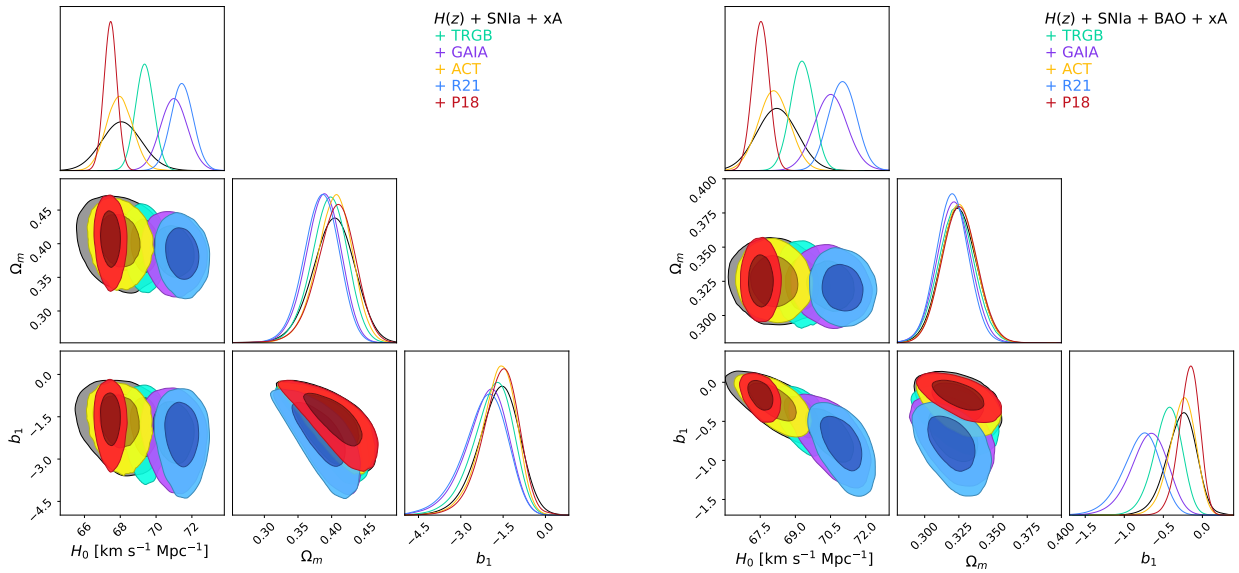


(a) (b)

Figure 4.5: C.L posterior results using the $f_1(T)$ model (2.17) for the *(a)* $H(z)$ and SNIa Pantheon compilation with the QSO xA sample, and *(b)* the combination including the BAO sample. The shadowed regions correspond to $1\sigma$ and $2\sigma$, respectively. We use the color code blue for R21 prior, purple for GAIA, red for P18, green for F20, and yellow for ACT. Additionally, the model that was tested with flat prior is represented in black color.

| Data Set | $H_0$ [km s$^{-1}$ Mpc$^{-1}$] | $\Omega_m$ | $b_1$ | $M$ | $\beta'$ | $\chi^2_{\rm min}$ |
|---|---|---|---|---|---|---|
| $H(z)$ + SNIa + nUVX | $67.2^{+4.3}_{-3.5}$ | $0.369^{+0.052}_{-0.069}$ | $-0.41^{+0.63}_{-0.64}$ | $-19.42^{+0.12}_{-0.13}$ | $-11.74^{+1.31}_{-1.82}$ | 3106.06 |
| & R21 | $73.2^{+0.6}_{-0.8}$ | $0.327^{+0.051}_{-0.067}$ | $-0.11^{+0.47}_{-0.55}$ | $-19.26^{+0.03}_{-0.02}$ | $-10.57^{+1.13}_{-1.94}$ | 3108.32 |
| & P18 | $67.5^{+0.3}_{-0.4}$ | $0.322^{+0.012}_{-0.013}$ | $-0.05 \pm 0.11$ | $-19.43 \pm 0.01$ | $-11.54^{+1.28}_{-1.84}$ | 3117.72 |
| & F20 | $69.8^{+0.5}_{-0.6}$ | $0.351^{+0.045}_{-0.062}$ | $-0.25^{+0.47}_{-0.57}$ | $-19.36 \pm 0.02$ | $-10.9^{+1.06}_{-1.99}$ | 3106.82 |
| & GD3 | $70.8 \pm 0.7$ | $0.317^{+0.010}_{-0.012}$ | $-0.45^{+0.16}_{-0.21}$ | $-19.35 \pm 0.02$ | $-11.09^{+1.42}_{-1.69}$ | 3138.27 |
| & ACT | $67.9 \pm 0.7$ | $0.321^{+0.013}_{-0.012}$ | $-0.10 \pm 0.13$ | $-19.42 \pm 0.02$ | $-10.12^{+1.14}_{-1.97}$ | 3117.61 |
| $H(z)$ + SNIa + BAO + nUVX | $67.8^{+1.0}_{-0.9}$ | $0.321 \pm 0.012$ | $-0.08^{+0.14}_{-0.15}$ | $-19.42^{+0.03}_{-0.02}$ | $-11.82^{+1.31}_{-1.80}$ | 3117.59 |
| & R21 | $71.3 \pm 0.6$ | $0.315^{+0.011}_{-0.012}$ | $-0.53^{+0.17}_{-0.20}$ | $-19.34 \pm 0.02$ | $-11.36^{+1.27}_{-1.86}$ | 3138.83 |
| & P18 | $67.4^{+0.4}_{-0.3}$ | $0.322^{+0.014}_{-0.015}$ | $-0.05^{+0.11}_{-0.13}$ | $-19.43 \pm 0.01$ | $-10.78^{+1.17}_{-1.92}$ | 3117.71 |
| & F20 | $69.3 \pm 0.5$ | $0.318^{+0.013}_{-0.011}$ | $-0.26^{+0.13}_{-0.16}$ | $-19.38 \pm 0.01$ | $-10.73^{+1.25}_{-1.92}$ | 3121.12 |
| & GD3 | $70.8 \pm 0.7$ | $0.316 \pm 0.012$ | $-0.46^{+0.18}_{-0.20}$ | $-19.35 \pm 0.02$ | $-11.01^{+1.12}_{-1.98}$ | 3138.27 |
| & ACT | $67.8 \pm 0.7$ | $0.321^{+0.012}_{-0.013}$ | $-0.10^{+0.13}_{-0.14}$ | $-19.42 \pm 0.02$ | $-10.89^{+1.15}_{-1.83}$ | 3117.67 |

Table 4.6: $f_1(T)$ model (2.17) constraints for the baseline $H(z)$ measurements, SNIa compilation, and BAO sample. We include the QSO nUVX sample.

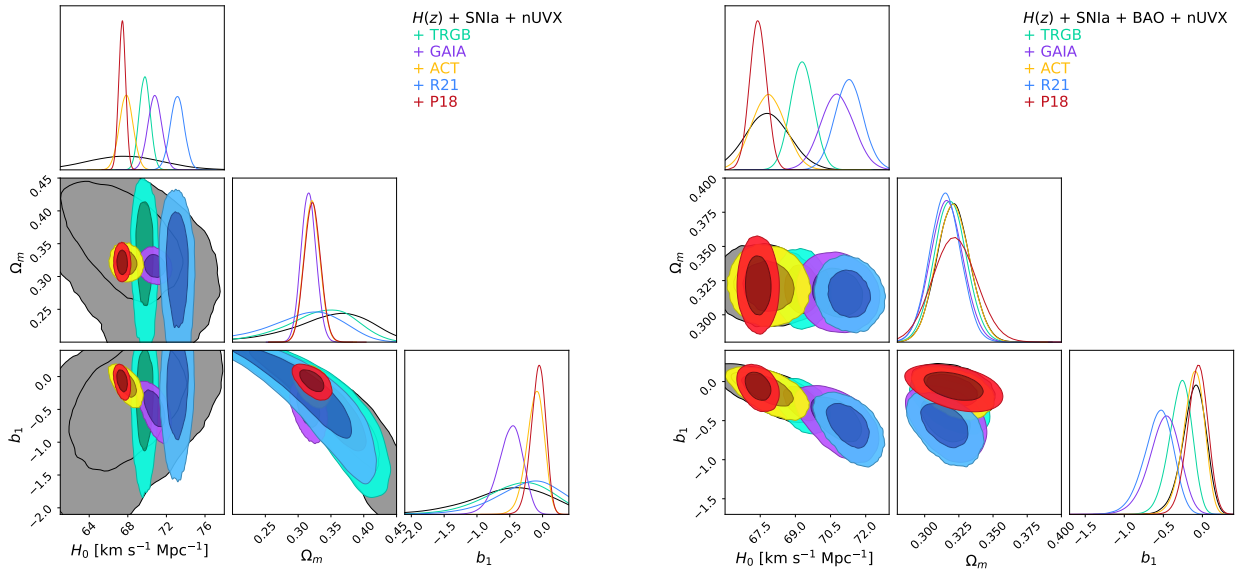


(a) (b)

Figure 4.6: C.L posterior results for the $f_1(T)$ model (2.17) for the combinations *(a)* $H(z)$ and SNIa Pantheon compilation with the QSO nUVX sample, and *(b)* the combination with the BAO sample. The shadowed regions correspond to $1\sigma$ and $2\sigma$, respectively. We use the color code blue for R21 prior, purple for GAIA, red for P18, green for F20, and yellow for ACT. Additionally, the model that was tested with flat prior is represented in black color.

The constraints using the QSO nUVX sample can be seen both in Figure 4.6 and Table 4.6. Similar to previous results, without using priors, the $H_0$ value is comparable to the one obtained by Planck Collaboration, but with a higher uncertainty $H_0 = 67.2^{+4.3}_{-3.5}$ km s$^{-1}$ Mpc$^{-1}$ without the BAO sample, and $H_0 = 67.8^{+1.0}_{-0.9}$ km s$^{-1}$ Mpc$^{-1}$ with the BAO sample, both values at $2\sigma$ from the

Planck estimation. Using R21 and GD3 priors, the estimations resemble a high $H_0$ value with a low fractional matter $\Omega_m$. This is contrary to the results using ACT and P18 priors, which result in lower values for $H_0$ and high values for $\Omega_m$. For example the highest $H_0$ value is the one obtained using the combination $H(z)$, SNIa, nUVX baseline with the R21 prior with $H_0 = 73.2^{+0.6}_{-0.8}$ km s$^{-1}$ Mpc$^{-1}$. Finally, the lowest value obtained using $H(z)$, SNIa, BAO and nUVX baseline with the P18 prior is $H_0 = 67.4^{+0.4}_{-0.3}$ km s$^{-1}$ Mpc$^{-1}$.

As done with the ΛCDM model, the Power-law model shows consistency along the datasets independently from the used prior. However the value of $\chi^2_{\rm min}$ is slightly higher than the one obtained with the Standard cosmological model for all the dataset combinations. The BAO tendency to increase the $\chi^2_{\rm min}$ value is still present in this model. The same could be said for the xA sample and the nUVX where the first sample reduces the error in the parameter estimation.

## 4.4 Linder model

For the Linder model, when $b_2 \to \infty$ we recover the standard ΛCDM model, so the results here are represented using the inverse of the free parameter, and therefore when $1/b_2 \to 0$ we recover the standard model. For the baselines, the results can be seen in Table 4.7 and in Figures 4.7.

| Data set | $H_0$ [km s$^{-1}$ Mpc$^{-1}$] | $\Omega_m$ | $1/b_2$ | $M$ | $\chi^2_{\rm min}$ |
|---|---|---|---|---|---|
| $H(z)$ + SNIa | $69.8^{+3.4}_{-3.8}$ | $0.292^{+0.029}_{-0.034}$ | $0.00^{+0.27}_{-0.00}$ | $-19.36 \pm 0.11$ | 949.41 |
| & R21 | $73.1^{+0.8}_{-0.7}$ | $0.283^{+0.030}_{-0.039}$ | $0.00^{+0.31}_{-0.00}$ | $-19.25^{+0.03}_{-0.02}$ | 950.71 |
| & P18 | $67.4 \pm 0.4$ | $0.300^{+0.024}_{-0.031}$ | $0.027^{+0.224}_{-0.024}$ | $-19.43 \pm 0.02$ | 949.66 |
| & F20 | $69.7^{+0.6}_{-0.5}$ | $0.290^{+0.029}_{-0.031}$ | $0.00^{+0.27}_{-0.00}$ | $-19.35 \pm 0.02$ | 949.45 |
| & GD3 | $73.7 \pm 1.0$ | $0.281^{+0.028}_{-0.037}$ | $0.00^{+0.34}_{-0.00}$ | $-19.24 \pm 0.03$ | 951.15 |
| & ACT | $68.0^{+1.1}_{-1.0}$ | $0.295^{+0.026}_{-0.029}$ | $0.00^{+0.25}_{-0.00}$ | $-19.41^{+0.03}_{-0.04}$ | 949.52 |
| $H(z)$ + SNIa + BAO | $68.0 \pm 0.7$ | $\left(300.6^{+8.6}_{-11.6}\right) \times 10^{-3}$ | $0.048^{+0.178}_{-0.046}$ | $-19.41 \pm 0.02$ | 961.25 |
| & R21 | $70.2 \pm 0.5$ | $\left(294.0^{+9.6}_{-10.3}\right) \times 10^{-3}$ | $0.059^{+0.059}_{-0.058}$ | $-19.35 \pm 0.2$ | 995.28 |
| & P18 | $67.4^{+0.3}_{-0.4}$ | $0.316^{+0.011}_{-0.010}$ | $0.047^{+0.107}_{-0.046}$ | $-19.42 \pm 0.01$ | 960.30 |
| & F20 | $68.9 \pm 0.4$ | $\left(296.7^{+11.0}_{-9.6}\right) \times 10^{-3}$ | $0.00^{+0.14}_{-0.00}$ | $-19.38^{+0.01}_{-0.02}$ | 964.89 |
| & GD3 | $69.4 \pm 0.5$ | $\left(294.9^{+10.3}_{-9.5}\right) \times 10^{-3}$ | $0.083^{+0.047}_{-0.081}$ | $-19.37 \pm 0.02$ | 987.31 |
| & ACT | $67.4 \pm 0.6$ | $0.323^{+0.010}_{-0.012}$ | $0.045^{+0.106}_{-0.042}$ | $-19.42 \pm 0.02$ | 961.25 |

Table 4.7: $f_2(T)$ model (2.20) constraints for the combinations of $H(z)$ measurements, Pantheon SNIa compilation and BAO catalogs. At the top of the table are the results without the BAO sample, while at the bottom are the results including this latter sample with different results corresponding to the priors imposed on $H_0$. The color codes are indicated in the description for each prior to consideration.

For this model, using $H(z)$ and SNIa baseline without prior results in constraints with a low $H_0$ value consistent with P18, but with a large error estimation and a confirmation of ΛCDM as $1/b_2 = 0.00^{+0.27}_{-0.00}$. Using R21 and GD3 priors show the largest values for $H_0$ as $H_0 = 73.1^{+0.8}_{-0.7}$ km s$^{-1}$ Mpc$^{-1}$, and $H_0 = 73.7 \pm 1.0$ km s$^{-1}$ Mpc$^{-1}$, respectively. The fractional matter density $\Omega_m$

also has the slowest values using those priors and both of them recover $1/b_2 \to 0$. Constraining the model with the F20 prior shows also a preference for the ΛCDM model as the use of P18 and ACT obtaining the lowest $H_0$ values $H_0 = 67.4 \pm 0.4$ km s$^{-1}$ Mpc$^{-1}$ and $H_0 = 68.0^{+1.1}_{-1.0}$ km s$^{-1}$ Mpc$^{-1}$, respectively. The constraints give highest matter densities as $\Omega_m = 0.300^{+0.024}_{-0.031}$ and $\Omega_m = 0.295^{+0.026}_{-0.029}$ for the those priors. As mentioned before, the use of the BAO sample modifies the $H_0$ estimations resulting in a lower value, that without a prior the combination obtains $H_0 = 68.0 \pm 0.7$ km s$^{-1}$ Mpc$^{-1}$, with a $1/b_2 = 0.048^{+0.178}_{-0.046}$ at $2\sigma$ from the confirmation of ΛCDM. Using priors results in higher $H_0$ estimates for R21 and GD3 priors. Furthermore, R21 and ACT priors estimate lower values of $H_0$ and higher $\Omega_m$ with $1/b_2$ closer to ΛCDM confirmation.

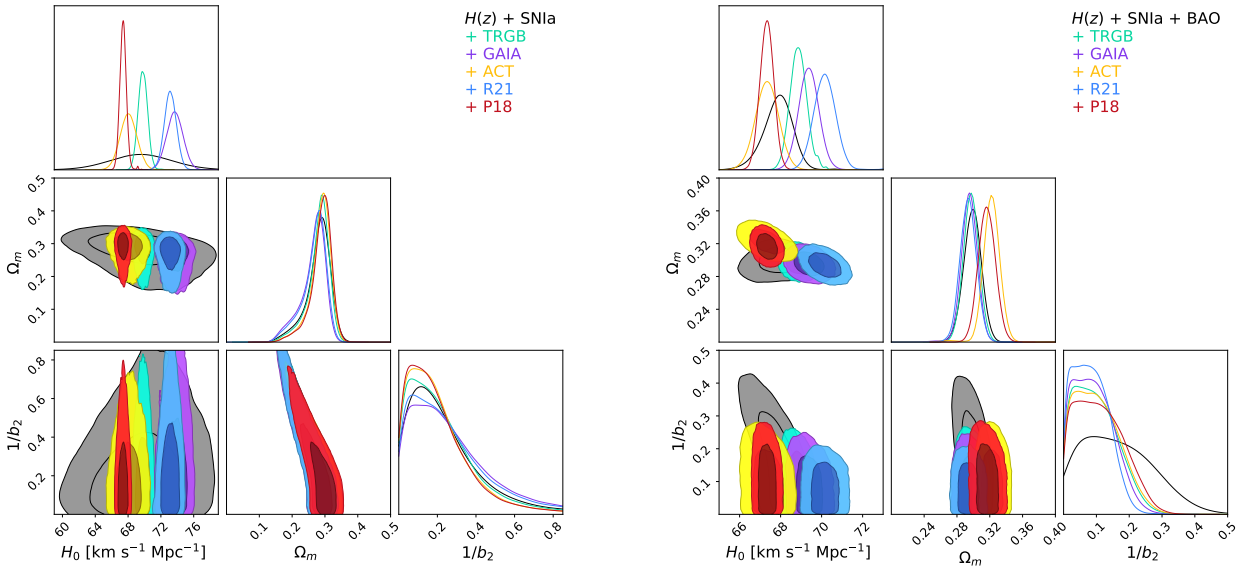


(a) (b)

Figure 4.7: C.L posterior results using $f_2(T)$ model (2.20) for the *(a)* $H(z)$ and SNIa Pantheon compilation. *(b)* Combination including the BAO sample. The shadowed regions correspond to $1\sigma$ and $2\sigma$, respectively. We use the color code blue for R21 prior, purple for GAIA, red for P18, green for F20, and yellow for ACT. Additionally, the model that was tested with flat prior is represented in black color.

| Data set | $H_0$ [km s$^{-1}$ Mpc$^{-1}$] | $\Omega_m$ | $1/b_2$ | $M$ | $\chi^2_{\rm min}$ |
|---|---|---|---|---|---|
| $H(z)$ + SNIa + xA | $67.4^{+1.0}_{-0.9}$ | $0.296 \pm 0.019$ | $0.00^{+0.15}_{-0.00}$ | $-19.43 \pm 0.03$ | 2616.99 |
| & R21 | $71.2 \pm 0.6$ | $0.264 \pm 0.019$ | $0.00^{+0.14}_{-0.00}$ | $-19.33 \pm 0.02$ | 2639.99 |
| & P18 | $67.4 \pm 0.4$ | $0.297 \pm 0.019$ | $0.094^{+0.066}_{-0.091}$ | $-19.43^{+0.01}_{-0.02}$ | 2617.00 |
| & F20 | $69.2^{+0.6}_{-0.5}$ | $0.281 \pm 0.017$ | $0.053^{+0.093}_{-0.051}$ | $-19.4 \pm 0.02$ | 2621.45 |
| & GD3 | $70.7^{+0.7}_{-0.8}$ | $0.269 \pm 0.020$ | $0.00^{+0.14}_{-0.00}$ | $-19.34 \pm 0.02$ | 2639.23 |
| & ACT | $67.7^{+0.7}_{-0.8}$ | $0.294^{+0.020}_{-0.018}$ | $0.018^{+0.141}_{-0.014}$ | $-19.42 \pm 0.02$ | 2617.09 |
| $H(z)$ + SNIa + BAO + xA | $67.9 \pm 0.5$ | $0.298^{+0.012}_{-0.011}$ | $0.025^{+0.134}_{-0.023}$ | $-19.41 \pm 0.02$ | 2628.34 |
| & R21 | $69.6 \pm 0.5$ | $0.293 \pm 0.011$ | $0.00^{+0.10}_{-0.00}$ | $-19.37^{+0.01}_{-0.02}$ | 2670.16 |
| & P18 | $67.3 \pm 0.3$ | $0.314^{+0.012}_{-0.011}$ | $0.022^{+0.107}_{-0.021}$ | $-19.43 \pm 0.01$ | 2628.27 |
| & F20 | $68.6^{+0.4}_{-0.3}$ | $\left(295.0^{+9.0}_{-9.3}\right) \times 10^{-3}$ | $0.038^{+0.087}_{-0.036}$ | $-19.39 \pm 0.01$ | 2634.83 |
| & GD3 | $69.0^{+0.5}_{-0.4}$ | $\left(293.2^{+9.1}_{-9.4}\right) \times 10^{-3}$ | $0.051^{+0.072}_{-0.050}$ | $-19.38^{+0.02}_{-0.01}$ | 2658.71 |
| & ACT | $67.9^{+0.4}_{-0.5}$ | $0.300^{+0.010}_{-0.011}$ | $0.056^{+0.107}_{-0.052}$ | $-19.42 \pm 0.02$ | 2628.34 |

Table 4.8: $f_2(T)$ model (2.20) constraints for the combination $H(z)$ measurements, SNIa compilation, and with both BAO surveys. We include the QSO xA sample.

The constraints for the $f_2(T)$ model using the QSO xA sample can be seen in Table 4.8 and in both figures in 4.8. Both results using the QSO xA sample without a prior and the BAO sample for the $H_0$ are in agreement with the Planck Collaboration results with $H_0 = 67.4^{+1.0}_{-0.9}$ km s$^{-1}$ Mpc$^{-1}$ without the BAO sample, and $H_0 = 67.9 \pm 0.5$ km s$^{-1}$ Mpc$^{-1}$ with the BAO sample. Both estimations of $b_2 \to 0$, and $\Omega_m \sim 0.29$ achieve similar results, consistent with a confirmation towards the $\Lambda$CDM model. Similar to previous results, the highest $H_0$ estimation are the ones obtained using R21 and GD3 priors without the BAO data set, and the lower values are the ones obtained with ACT and P18 priors. Using the F20 prior we obtain $H_0 \sim 69$ km s$^{-1}$ Mpc$^{-1}$, which is consistent with an intermediate value. It is important to remark that when using all the priors the value for $1/b_2$ shows a confirmation of the $\Lambda$CDM model at $2\sigma$ level, i.e. $1/b_2 \to 0$ meaning that $b_2 \to \infty$, which means that this specific model does not show a significantly different behavior from the standard cosmological model at least using these combinations with the QSO xA sample.

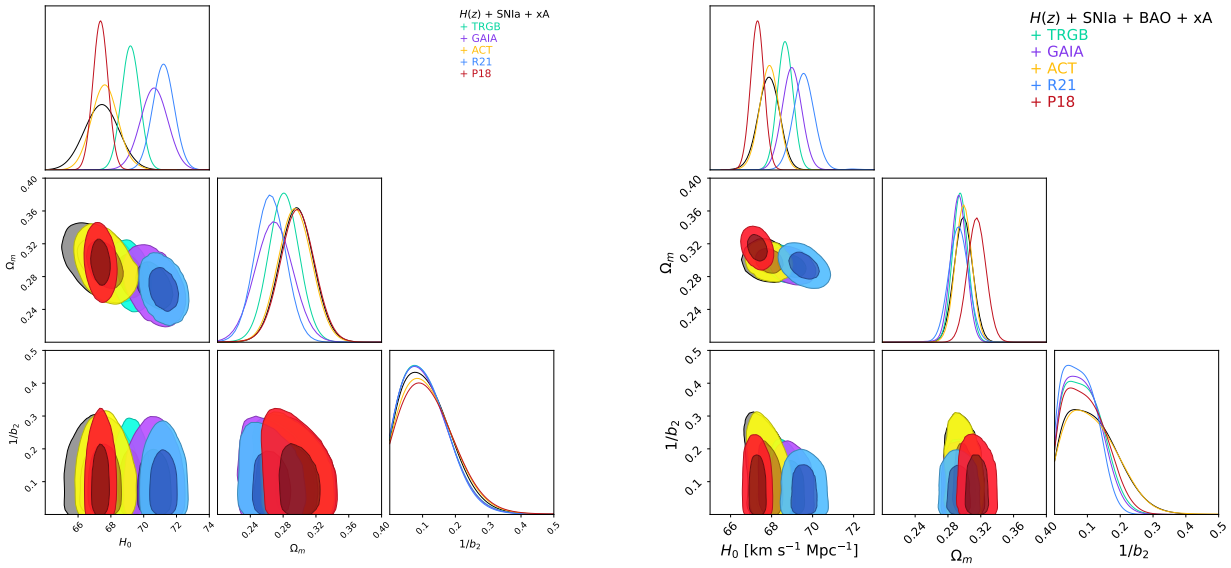


(a) (b)

Figure 4.8: C.L posterior results using the $f_2(T)$ model (2.20) for the *(a)* $H(z)$ and SNIa Pantheon compilation with the QSO xA sample, and *(b)* the combination including the BAO sample. The shadowed regions correspond to $1\sigma$ and $2\sigma$, respectively. We use the color code blue for R21 prior, purple for GAIA, red for P18, green for F20, and yellow for ACT. Additionally, the model that was tested with flat prior is represented in black color.

| Data set | $H_0$ [km s$^{-1}$ Mpc$^{-1}$] | $\Omega_m$ | $1/b_2$ | $M$ | $\beta'$ | $\chi^2_{\rm min}$ |
|---|---|---|---|---|---|---|
| $H(z)$ + SNIa + nUVX | $69.9^{+3.4}_{-3.9}$ | $0.291^{+0.031}_{-0.033}$ | $0.11^{+0.16}_{-0.11}$ | $-19.35^{+0.11}_{-0.12}$ | $-11.38^{+2.24}_{-2.98}$ | 3107.04 |
| & R21 | $73.1^{+0.8}_{-0.7}$ | $0.282^{+0.028}_{-0.035}$ | $0.00^{+0.31}_{-0.00}$ | $-19.25^{+0.02}_{-0.03}$ | $-10.73^{+1.15}_{-1.04}$ | 3108.34 |
| & P18 | $67.4 \pm 0.4$ | $0.298^{+0.026}_{-0.030}$ | $0.017^{+0.227}_{-0.014}$ | $-19.43 \pm 0.02$ | $-10.52^{+1.19}_{-1.00}$ | 3107.27 |
| & F20 | $69.8^{+0.5}_{-0.6}$ | $0.292^{+0.026}_{-0.032}$ | $0.046^{+0.231}_{-0.043}$ | $-19.35 \pm 0.02$ | $-10.12^{+1.12}_{-1.98}$ | 3107.07 |
| & GD3 | $73.7^{+1.0}_{-0.9}$ | $0.281^{+0.028}_{-0.037}$ | $0.099^{+0.238}_{-0.096}$ | $-19.24 \pm 0.03$ | $-10.90^{+1.01}_{-1.18}$ | 3107.76 |
| & ACT | $68.2^{+0.8}_{-1.2}$ | $0.297^{+0.028}_{-0.032}$ | $0.046^{+0.203}_{-0.043}$ | $-19.41^{+0.03}_{-0.04}$ | $-9.9^{+1.18}_{-1.99}$ | 3107.14 |
| $H(z)$ + SNIa + BAO + nUVX | $67.2^{+0.8}_{-0.7}$ | $0.317^{+0.013}_{-0.012}$ | $0.071^{+0.097}_{-0.070}$ | $-19.43 \pm 0.02$ | $-10.83^{+1.59}_{-1.51}$ | 3117.91 |
| & R21 | $70.2^{+0.5}_{-0.6}$ | $(294.8^{+8.9}_{-10.9}) \times 10^{-3}$ | $0.025^{+0.092}_{-0.024}$ | $-19.35 \pm 0.02$ | $-10.85^{+1.02}_{-1.26}$ | 3152.89 |
| & P18 | $67.3 \pm 0.3$ | $0.317^{+0.011}_{-0.010}$ | $0.030^{+0.126}_{-0.029}$ | $-19.43 \pm 0.01$ | $-10.52^{+1.15}_{-1.01}$ | 3117.91 |
| & F20 | $68.8^{+0.4}_{-0.5}$ | $0.305 \pm 0.010$ | $0.075^{+0.052}_{-0.074}$ | $-19.39 \pm 0.01$ | $-10.13^{+1.11}_{-1.98}$ | 3125.64 |
| & GD3 | $69.4 \pm 0.6$ | $0.300^{+0.010}_{-0.011}$ | $0.054^{+0.075}_{-0.052}$ | $-19.37 \pm 0.02$ | $-10.34^{+1.14}_{-1.96}$ | 3148.19 |
| & ACT | $67.5 \pm 0.6$ | $0.316 \pm 0.011$ | $0.055^{+0.102}_{-0.054}$ | $-19.42 \pm 0.02$ | $-10.34^{+1.17}_{-1.96}$ | 3118.12 |

Table 4.9: $f_2(T)$ model (2.20) constraints for the baseline $H(z)$ measurements, SNIa compilation, and BAO sample. We include the QSO nUVX sample.

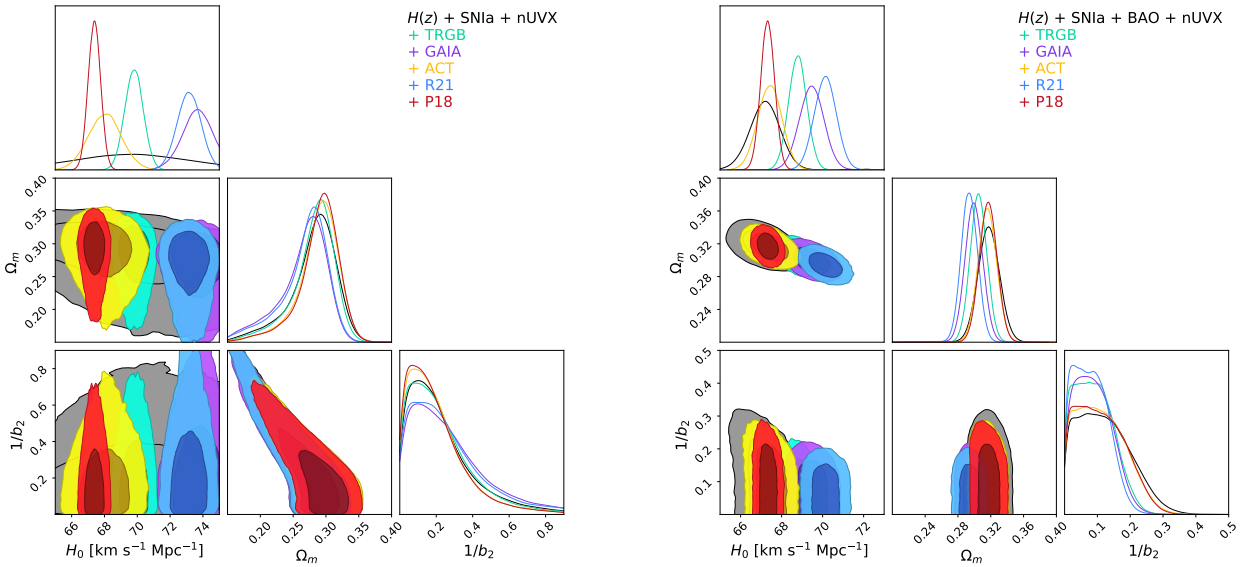


Figure 4.9: C.L posterior results for the $f_2(T)$ model (2.20) for the combinations *(a)* $H(z)$ and SNIa Pantheon compilation with the QSO nUVX sample, and *(b)* the combination with the BAO sample. The shadowed regions correspond to $1\sigma$ and $2\sigma$, respectively. We use the color code blue for R21 prior, purple for GAIA, red for P18, green for F20, and yellow for ACT. Additionally, the model that was tested with flat prior is represented in black color.

The constraints using the QSO nUVX sample have similar behavior to the previous combinations of data sets. As for all the priors, the free parameter $1/b_2 \to 0$, meaning that we have a confirmation for the ΛCDM model. This combination of data does not show a significant deviation from the standard model.

Regarding $H_0$, as shown before with other data set combinations, the results using BAO sets give lower values for this Hubble parameter. Using SNIa and $H(z)$ with the QSO nUVX sample results in a higher value for it. For example, without the BAO sample and using the GD3 prior $H_0 = 73.7^{+1.0}_{-0.9}$ km s$^{-1}$ Mpc$^{-1}$, being the highest value in this baseline which corresponds to $\Omega_m = 0.281^{+0.028}_{-0.037}$. The lowest $H_0$ value corresponds to the one obtained using all the data sets including the BAO sample and the P18 prior $H_0 = 67.3 \pm 0.3$ km s$^{-1}$ Mpc$^{-1}$. This corresponds to the highest fractional matter density $\Omega_m = 0.317^{+0.011}_{-0.010}$. All the results can be explored in Figure 4.9 and Table 4.9.

Similar to the ΛCDM case, in the Linder model we have consistency in the datasets used independently from the prior used. The lowest $\chi^2_{\rm min}$ is the one using only the $H(z)$ and SNIa datasets while, similar to the previous models, the xA sample increases the value. Altough the xA sample also increases the accuracy in the parameter estimation. The nUVX sample is the contrary, reduces the $\chi^2_{\rm min}$ but increases the inaccuracy in the parameter determination.

## 4.5 Modified Linder model

For the baselines described, the results are shown in Figure 4.10 and Table 4.10. We can recover the ΛCDM model in this case when $1/b_3 \to 0$, and all the combinations with the priors obtain the respective confirmation for this standard scenario.

| Data set | $H_0$ [km s$^{-1}$ Mpc$^{-1}$] | $\Omega_m$ | $1/b_3$ | $M$ | $\chi^2_{\rm min}$ |
|---|---|---|---|---|---|
| $H(z)$ + SNIa | $69.5^{+3.5}_{-3.7}$ | $0.294^{+0.024}_{-0.022}$ | $0.015^{+0.130}_{-0.014}$ | $-19.37 \pm 0.11$ | 949.41 |
| & R21 | $73.1 \pm 0.8$ | $0.286^{+0.024}_{-0.023}$ | $0.059^{+0.090}_{-0.058}$ | $-19.26 \pm 0.03$ | 950.71 |
| & P18 | $67.4 \pm 0.4$ | $0.302^{+0.019}_{-0.022}$ | $0.00^{+0.14}_{-0.00}$ | $-19.43 \pm 0.02$ | 949.65 |
| & F20 | $69.8^{+0.6}_{-0.5}$ | $0.294^{+0.021}_{-0.020}$ | $0.00^{+0.14}_{-0.00}$ | $-19.36 \pm 0.02$ | 949.45 |
| & GD3 | $73.7 \pm 1.0$ | $0.285^{+0.022}_{-0.020}$ | $0.050^{+0.106}_{-0.049}$ | $-19.235 \pm 0.03$ | 951.15 |
| & ACT | $67.7^{+1.2}_{-0.7}$ | $0.299^{+0.023}_{-0.024}$ | $0.00^{+0.014}_{-0.00}$ | $-19.41 \pm 0.04$ | 949.51 |
| $H(z)$ + SNIa + BAO | $68.1^{+0.5}_{-0.6}$ | $0.300^{+0.012}_{-0.011}$ | $0.093^{+0.053}_{-0.091}$ | $-19.41 \pm 0.02$ | 960.24 |
| & R21 | $70.2^{+0.5}_{-0.6}$ | $0.294^{+0.011}_{-0.010}$ | $0.001^{+0.091}_{-0.000}$ | $-19.35 \pm 0.02$ | 995.28 |
| & P18 | $67.3^{+0.3}_{-0.4}$ | $0.318 \pm 0.010$ | $0.030^{+0.087}_{-0.029}$ | $-19.42 \pm 0.01$ | 960.30 |
| & F20 | $68.8^{+0.5}_{-0.4}$ | $\left(305.5^{+9.8}_{-10.6}\right) \times 10^{-3}$ | $\left(7.3^{+95.6}_{-6.2}\right) \times 10^{-3}$ | $-19.38^{+0.01}_{-0.02}$ | 968.02 |
| & GD3 | $69.4 \pm 0.5$ | $\left(294.8^{+10.9}_{-9.7}\right) \times 10^{-3}$ | $0.062^{+0.042}_{-0.061}$ | $-19.37 \pm 0.02$ | 987.32 |
| & ACT | $67.4^{+0.5}_{-0.6}$ | $\left(322.3^{+9.9}_{-9.8}\right) \times 10^{-3}$ | $0.077^{+0.037}_{-0.076}$ | $-19.42 \pm 0.02$ | 961.25 |

Table 4.10: $f_3(T)$ model (2.23) constraints for the combinations of $H(z)$ measurements, Pantheon SNIa compilation and BAO catalogs. At the top of the table are the results without the BAO sample, while at the bottom are the results including this latter sample with different results corresponding to the priors imposed on $H_0$. The color codes are indicated in the description for each prior to consideration.

Without priors, the constraints for this model using the baseline combination get $H_0 = 69.5^{+3.5}_{-3.7}$ km s$^{-1}$ Mpc$^{-1}$, that is in concordance with Planck values, however, with a higher error estimation. Using the BAO sample we obtain $H_0 = 68.1^{+0.5}_{-0.6}$ km s$^{-1}$ Mpc$^{-1}$. When using priors, the higher estimation for the Hubble constant is $H_0 = 73.7 \pm 1.0$ km s$^{-1}$ Mpc$^{-1}$ using the GD3 prior and without the BAO data set. This corresponds to a lower fractional matter density $\Omega_m = 0.285^{+0.022}_{-0.020}$. The lower estimation using the P18 prior with the BAO data set estimates $H_0 = 67.3^{+0.3}_{-0.4}$ km s$^{-1}$ Mpc$^{-1}$ with $\Omega_m = 0.318 \pm 0.010$. With other priors, we obtain intermediate values maintaining the behavior in which the BAO data reduces the value of $H_0$ similar to the previous cases.

Using the QSO xA sample we obtain different results but maintain the same trend when using the BAO data, meaning that the value of $H_0$ still gets lower. r In this case, $H_0 = 67.2 \pm 0.6$ km s$^{-1}$ Mpc$^{-1}$ is the lowest value and corresponds to $\Omega_m = 0.317^{+0.011}_{-0.012}$, which is the highest estimation for the matter fraction. On the other way around, the highest $H_0 = 71.2 \pm 0.6$ km s$^{-1}$ Mpc$^{-1}$ corresponds to the lowest $\Omega_m = 0.286^{+0.024}_{-0.023}$. With other priors, we obtain $1/b_3 \to 0$, which confirms ΛCDM. This can be seen in Figure 4.10 and Table 4.10.

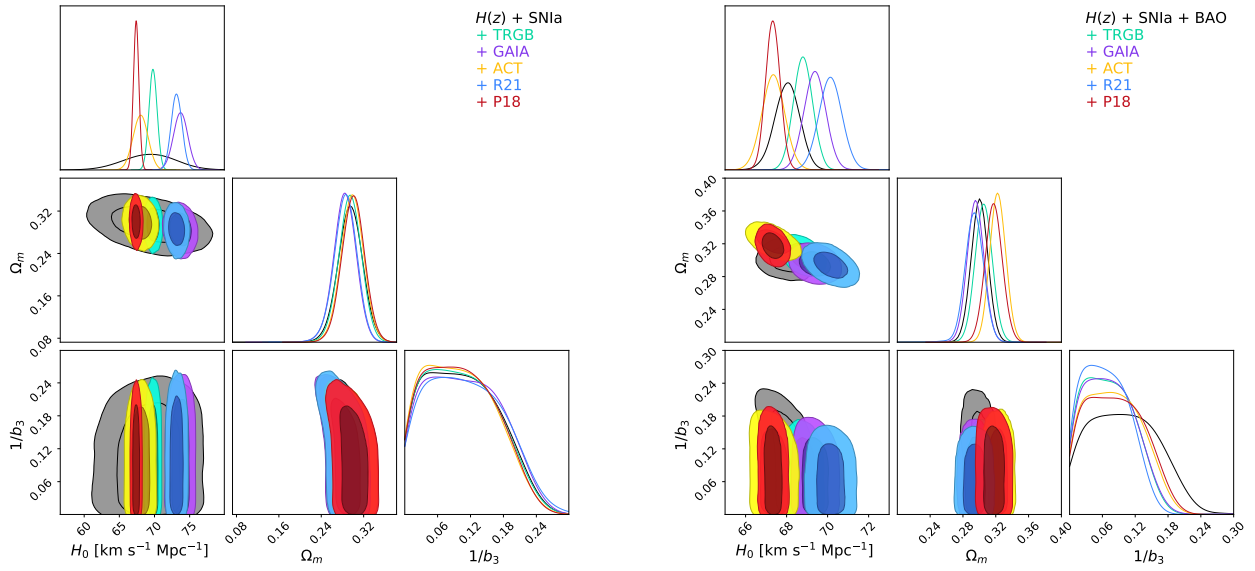


(a) (b)

Figure 4.10: C.L posterior results using $f_3(T)$ model (2.23) for the *(a)* $H(z)$ and SNIa Pantheon compilation. *(b)* Combination including the BAO sample. The shadowed regions correspond to $1\sigma$ and $2\sigma$, respectively. We use the color code blue for R21 prior, purple for GAIA, red for P18, green for F20, and yellow for ACT. Additionally, the model that was tested with flat prior is represented in black color.

| Data set | $H_0$ [km s$^{-1}$ Mpc$^{-1}$] | $\Omega_m$ | $1/b_3$ | $M$ | $\chi^2_{\rm min}$ |
|---|---|---|---|---|---|
| $H(z)$ + SNIa + xA | $67.4 \pm 1.0$ | $0.297^{+0.020}_{-0.018}$ | $\left(6.9^{+108.4}_{-6.1}\right) \times 10^{-3}$ | $-19.43 \pm 0.03$ | 2616.99 |
| & R21 | $71.2 \pm 0.6$ | $0.265^{+0.015}_{-0.017}$ | $0.028^{+0.077}_{-0.028}$ | $-19.33 \pm 0.02$ | 2639.99 |
| & P18 | $67.4^{+0.3}_{-0.4}$ | $0.299^{+0.017}_{-0.020}$ | $0.033^{+0.088}_{-0.032}$ | $-19.43 \pm 0.02$ | 2617.00 |
| & F20 | $69.2 \pm 0.5$ | $0.281^{+0.017}_{-0.016}$ | $0.083^{+0.030}_{-0.082}$ | $-19.38 \pm 0.02$ | 2621.45 |
| & GD3 | $70.7 \pm 0.7$ | $0.269^{+0.018}_{-0.016}$ | $0.055^{+0.051}_{-0.055}$ | $-19.34 \pm 0.02$ | 2639.22 |
| & ACT | $67.7^{+0.6}_{-0.8}$ | $0.294^{+0.024}_{-0.021}$ | $0.032^{+0.079}_{-0.031}$ | $-19.42^{+0.02}_{-0.03}$ | 2617.09 |
| $H(z)$ + SNIa + BAO + xA | $67.2 \pm 0.6$ | $0.317^{+0.011}_{-0.012}$ | $0.000^{+0.099}_{-0.000}$ | $-19.429^{+0.017}_{-0.019}$ | 2628.24 |
| & R21 | $69.6 \pm 0.5$ | $\left(293.0^{+10.1}_{-9.7}\right) \times 10^{-3}$ | $0.052^{+0.043}_{-0.051}$ | $-19.37 \pm 0.02$ | 2670.17 |
| & P18 | $67.3 \pm 0.3$ | $0.315^{+0.011}_{-0.010}$ | $0.064^{+0.044}_{-0.063}$ | $-19.43 \pm 0.01$ | 2628.27 |
| & F20 | $68.6^{+0.4}_{-0.5}$ | $0.302^{+0.012}_{-0.011}$ | $0.038^{+0.062}_{-0.037}$ | $-19.39 \pm 0.01$ | 2638.32 |
| & GD3 | $68.9^{+0.5}_{-0.6}$ | $\left(298.9^{+10.7}_{-10.0}\right) \times 10^{-3}$ | $0.008^{+0.076}_{-0.007}$ | $-19.38 \pm 0.02$ | 2662.63 |
| & ACT | $67.4 \pm 0.5$ | $\left(313.9^{+11.3}_{-9.9}\right) \times 10^{-3}$ | $0.078^{+0.031}_{-0.077}$ | $-19.43 \pm 0.02$ | 2628.54 |

Table 4.11: $f_3(T)$ model (2.23) constraints for the combination $H(z)$ measurements, SNIa compilation, and with both BAO surveys. We include the QSO xA sample.

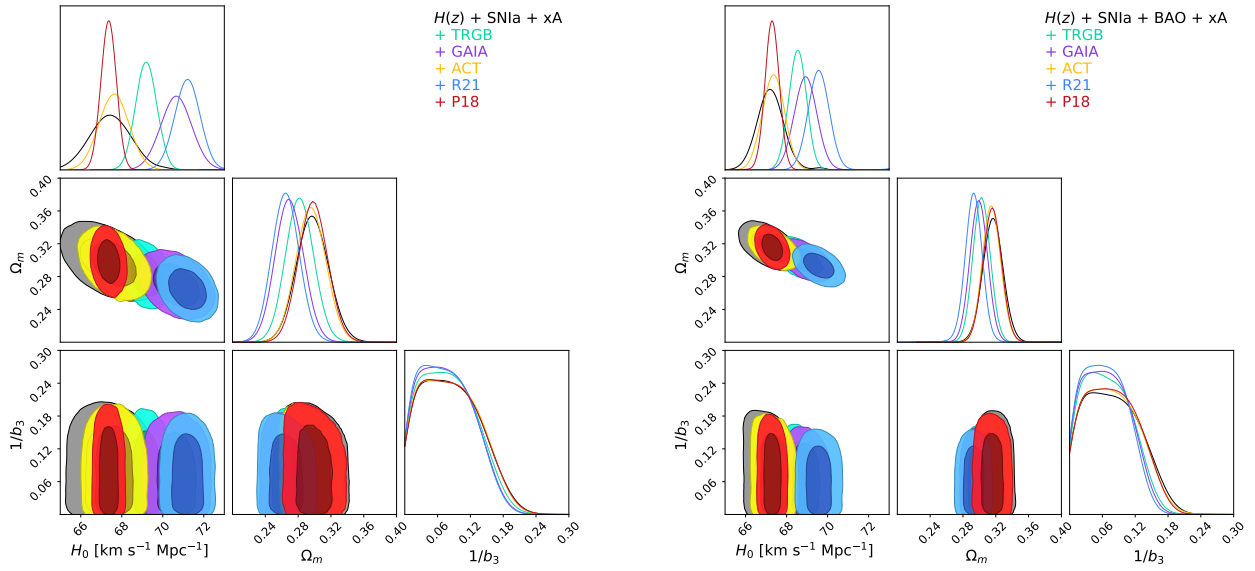


(a) (b)

Figure 4.11: C.L posterior results using the $f_3(T)$ model (2.23) for the *(a)* $H(z)$ and SNIa Pantheon compilation with the QSO xA sample, and *(b)* the combination including the BAO sample. The shadowed regions correspond to $1\sigma$ and $2\sigma$, respectively. We use the color code blue for R21 prior, purple for GAIA, red for P18, green for F20, and yellow for ACT. Additionally, the model that was tested with flat prior is represented in black color.

| Data set | $H_0$ [km s$^{-1}$ Mpc$^{-1}$] | $\Omega_m$ | $1/b_3$ | $M$ | $\beta'$ | $\chi^2_{\rm min}$ |
|---|---|---|---|---|---|---|
| $H(z)$ + SNIa + nUVX | $69.8^{+3.0}_{-4.2}$ | $0.296^{+0.022}_{-0.023}$ | $0.00^{+0.14}_{-0.00}$ | $-19.36^{+0.10}_{-0.12}$ | $-12.64^{+0.14}_{-0.73}$ | 3107.02 |
| & R21 | $73.2^{+0.7}_{-0.8}$ | $0.288^{+0.019}_{-0.021}$ | $0.059^{+0.090}_{-0.058}$ | $-19.27 \pm 0.02$ | $-12.21^{+0.13}_{-0.70}$ | 3108.34 |
| & P18 | $67.4 \pm 0.4$ | $0.301^{+0.021}_{-0.022}$ | $0.021^{+0.124}_{-0.020}$ | $-19.43 \pm 0.02$ | $-12.62^{+0.61}_{-0.53}$ | 3107.26 |
| & F20 | $69.8 \pm 0.6$ | $0.295 \pm 0.021$ | $0.077^{+0.065}_{-0.076}$ | $-19.36 \pm 0.02$ | $-12.51^{+0.66}_{-0.49}$ | 3107.06 |
| & GD3 | $73.8^{+0.9}_{-1.1}$ | $0.285 \pm 0.021$ | $0.018^{+0.133}_{-0.017}$ | $-19.24 \pm 0.03$ | $-12.63^{+0.48}_{-0.63}$ | 3108.77 |
| & ACT | $68.0 \pm 1.0$ | $0.299^{+0.021}_{-0.022}$ | $0.00^{+0.14}_{-0.00}$ | $-19.41 \pm 0.03$ | $-12.52^{+0.68}_{-0.47}$ | 3107.14 |
| $H(z)$ + SNIa + BAO + nUVX | $67.3^{+0.6}_{-0.8}$ | $0.318 \pm 0.012$ | $0.061^{+0.058}_{-0.060}$ | $-19.43 \pm 0.02$ | $-11.48^{+0.19}_{-0.11}$ | 3117.91 |
| & R21 | $70.1 \pm 0.2$ | $0.294 \pm 0.010$ | $0.067^{+0.032}_{-0.066}$ | $-19.39 \pm 0.02$ | $-12.61^{+0.45}_{-0.73}$ | 3152.90 |
| & P18 | $67.3^{+0.4}_{-0.3}$ | $0.318 \pm 0.012$ | $0.00^{+0.12}_{-0.00}$ | $-19.43 \pm 0.01$ | $-11.39^{+0.77}_{-0.36}$ | 3117.92 |
| & F20 | $68.8 \pm 0.4$ | $0.304^{+0.012}_{-0.011}$ | $0.020^{+0.085}_{-0.018}$ | $-19.39^{+0.02}_{-0.01}$ | $-11.77^{+0.77}_{-0.32}$ | 3125.63 |
| & GD3 | $69.5 \pm 0.6$ | $0.299^{+0.011}_{-0.010}$ | $0.018^{+0.079}_{-0.018}$ | $-19.37 \pm 0.02$ | $-11.37^{+0.88}_{-0.62}$ | 3148.20 |
| & ACT | $67.4^{+0.6}_{-0.5}$ | $0.316 \pm 0.011$ | $0.00^{+0.12}_{-0.00}$ | $-19.42 \pm 0.02$ | $-11.45^{+0.11}_{-0.10}$ | 3118.11 |

Table 4.12: $f_3(T)$ model (2.23) constraints for the baseline $H(z)$ measurements, SNIa compilation, and BAO sample. We include the QSO nUVX sample.

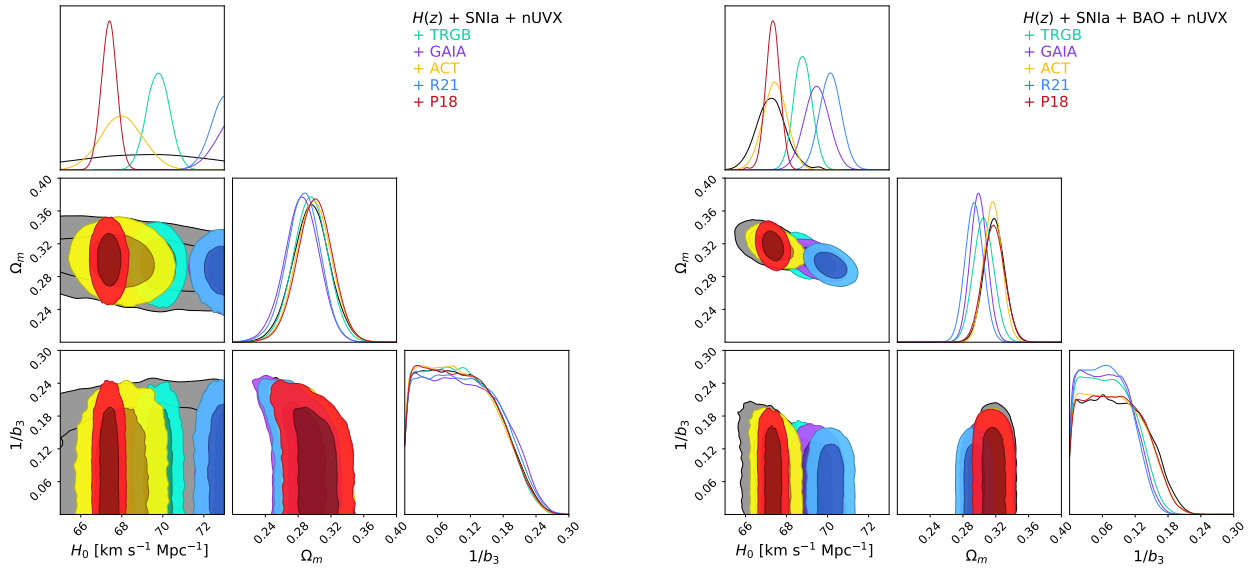


Figure 4.12: C.L posterior results for the $f_3(T)$ model (2.23) for the combinations *(a)* $H(z)$ and SNIa Pantheon compilation with the QSO nUVX sample, and *(b)* the combination with the BAO sample. The shadowed regions correspond to $1\sigma$ and $2\sigma$, respectively. We use the color code blue for R21 prior, purple for GAIA, red for P18, green for F20, and yellow for ACT. Additionally, the model that was tested with flat prior is represented in black color.

Using the QSO nUVX sample, a confirmation for ΛCDM again happens for each of the prior considered at least at $2\sigma$ level. With this baseline the highest $H_0$ estimation is obtained using the R21 prior without the BAO sample $H_0 = 73.2^{+0.7}_{-0.8}$ km s$^{-1}$ Mpc$^{-1}$, with the lowest estimation of $\Omega_m = 0.288^{+0.019}_{-0.021}$. Finally, the lowest estimation is $H_0 = 67.3^{+0.4}_{-0.3}$ km s$^{-1}$ Mpc$^{-1}$ with $\Omega_m = 0.318 \pm 0.012$.

For the Modified Linder model, the trend in the datasets continues being $H(z)$ and SNIa the lower $\chi^2_{\rm min}$ determination. The introduction of sample xA enables smaller parameter estimation errors as seen in Table 4.11. However, the $\chi^2_{\rm min}$ estimation is higher due to the high dispersion of the data obtained for the sample. This is in contrast to the nUVX sample, where parameter estimation contains a higher error determination but the $\chi^2_{\rm min}$ is significantly smaller. Again, in this model, in overall the $\chi^2_{\rm min}$ is slighly higher than the one obtained with ΛCDM.

## 4.6 Logarithmic Model

$f_4(T)$ has the same free parameters as the ΛCDM model, therefore we do not have a confirmation bias in this analysis. Using the $H(z)$ and SNIa baseline, the constraints show a diminution for the $H_0$ tension up to $2\sigma$, but with a higher error estimation and a fractional matter estimation lower than the one predicted with other cosmological models. This results gives $\Omega_m = 0.202^{+0.014}_{-0.019}$. All the constraints using both priors priors obtain $\Omega_m \sim 0.2$ with their respective value of $H_0$ close to the imposed prior. Additionally, using the BAO sample we estimate low $H_0$ estimations, e.g. including the R21 prior we obtain $H_0 = 68.2 \pm 0.6$ km s$^{-1}$ Mpc$^{-1}$ consistent with the P18 prior.

The same happens to the GD3 prior to obtaining a $H_0$ even lower than the one reported by the Planck Collaboration. With the P18 prior we obtain a low value $H_0 = 66.4^{+0.4}_{-0.3}$ km s$^{-1}$ Mpc$^{-1}$ with a matter density of approximately $\Omega_m \sim 0.27$. The complete results are reported in Table 4.13 and Figure 4.13.

| Data Set | $H_0$ [km s$^{-1}$ Mpc$^{-1}$] | $\Omega_m$ | $M$ | $\chi^2_{\text{min}}$ |
|---|---|---|---|---|
| $H(z)$ + SNeIa | $70.1^{+3.9}_{-3.3}$ | $0.202^{+0.014}_{-0.019}$ | $-19.30^{+0.08}_{-0.13}$ | 951.61 |
| & R21 | $73.2^{+0.7}_{-0.8}$ | $0.195^{+0.016}_{-0.015}$ | $-19.25^{+0.03}_{-0.02}$ | 952.17 |
| & P18 | $67.4 \pm 0.4$ | $0.205 \pm 0.016$ | $-19.42^{+0.01}_{-0.02}$ | 952.41 |
| & F20 | $69.8^{+0.6}_{-0.5}$ | $0.200^{+0.016}_{-0.015}$ | $-19.35 \pm 0.02$ | 951.66 |
| & GD3 | $73.9^{+0.9}_{-1.0}$ | $0.194^{+0.016}_{-0.014}$ | $-19.23 \pm 0.03$ | 952.47 |
| & ACT | $68.0^{+1.1}_{-1.0}$ | $0.203^{+0.017}_{-0.016}$ | $-19.40^{+0.04}_{-0.03}$ | 952.12 |
| $H(z)$ + SNeIa + BAO | $64.8 \pm 0.5$ | $\left(264.0^{+9.7}_{-9.9}\right) \times 10^{-3}$ | $-19.48 \pm 0.02$ | 974.34 |
| & R21 | $68.2 \pm 0.6$ | $\left(258.6^{+10.3}_{-8.6}\right) \times 10^{-3}$ | $-19.37 \pm 0.02$ | 1088.61 |
| & P18 | $66.4^{+0.4}_{-0.3}$ | $\left(273.8^{+8.8}_{-10.6}\right) \times 10^{-3}$ | $-19.42 \pm 0.01$ | 1018.55 |
| & F20 | $67.4^{+0.4}_{-0.5}$ | $\left(265.3^{+10.2}_{-8.8}\right) \times 10^{-3}$ | $-19.39 \pm 0.01$ | 1044.32 |
| & GD3 | $66.2^{+0.6}_{-0.5}$ | $\left(289.9^{+9.3}_{-8.8}\right) \times 10^{-3}$ | $-19.42 \pm 0.02$ | 1087.61 |
| & ACT | $64.9^{+0.5}_{-0.7}$ | $\left(284.4^{+12.0}_{-9.1}\right) \times 10^{-3}$ | $-19.47 \pm 0.02$ | 1006.92 |

Table 4.13: $f_4(T)$ model (2.26) constraints for the combinations of $H(z)$ measurements, Pantheon SNIa compilation and BAO catalogs. At the top of the table are the results without the BAO sample, while at the bottom are the results including this latter sample with different results corresponding to the priors imposed on $H_0$. The color codes are indicated in the description for each prior to consideration.

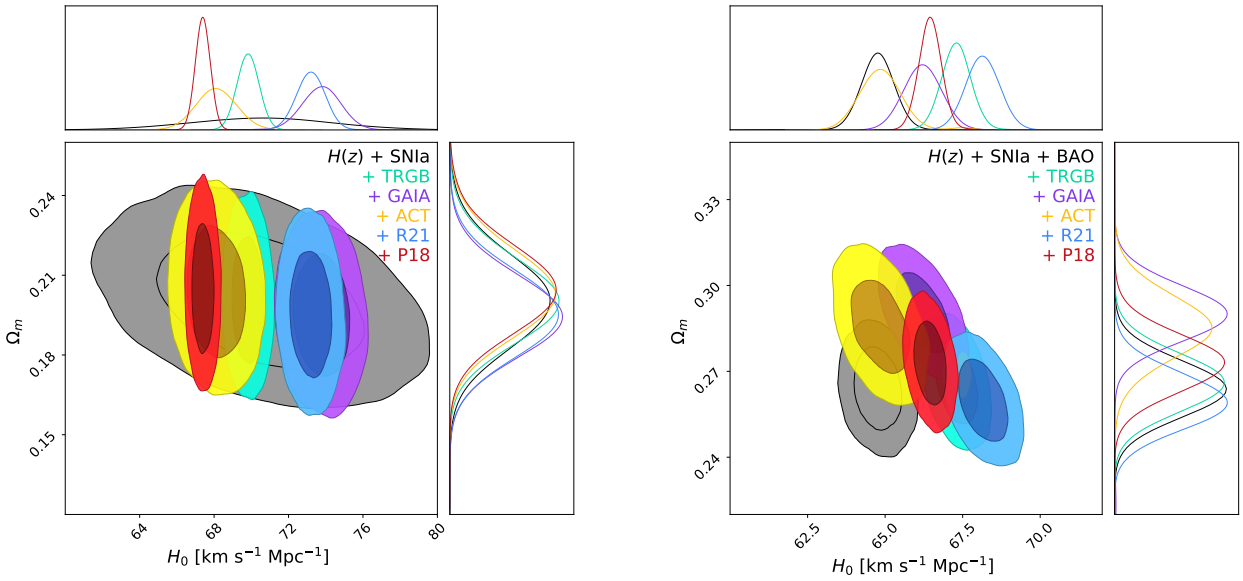


(a) (b)

Figure 4.13: C.L posterior results using $f_4(T)$ model (2.26) for the *(a)* $H(z)$ and SNIa Pantheon compilation. *(b)* Combination including the BAO sample. The shadowed regions correspond to $1\sigma$ and $2\sigma$, respectively. We use the color code blue for R21 prior, purple for GAIA, red for P18, green for F20, and yellow for ACT. Additionally, the model that was tested with flat prior is represented in black color.

Using the QSO xA sample we reduce the value $H_0 = 67.3 \pm 1.0$ km s$^{-1}$ Mpc$^{-1}$ with the $H(z)$ and SNIa baseline. We obtain $H_0 = 64.2 \pm 0.6$ km s$^{-1}$ Mpc$^{-1}$ when including the BAO sample. This also has the impact of raising the fractional matter density estimation to $\Omega_m = 0.291^{+0.011}_{-0.013}$ closer to the obtained using the ΛCDM model and larger than the one obtained without the BAO sample with $\Omega_m = 0.201^{+0.017}_{-0.014}$. The lowest $\Omega_m$ estimation is obtained using the R21 prior with the $H(z)$ and SNIa baseline, which shares also the biggest $H_0$ value with $\Omega_m = 0.175^{+0.012}_{-0.013}$ and $H_0 = 71.1^{+0.7}_{-0.5}$ km s$^{-1}$ Mpc$^{-1}$.

In this model, the use of the BAO sample in the entire baselines has the impact of lowering the value of $H_0$ and raising the estimation of $\Omega_m$, as for all the results independently of the prior, $\Omega_m \sim 0.26$ and a low value of $H_0$ as seen in $H_0 = 65.0 \pm 0.5$ km s$^{-1}$ Mpc$^{-1}$ using, e.g. the ACT prior.

| Data Set | $H_0$ [km s$^{-1}$ Mpc$^{-1}$] | $\Omega_m$ | $M$ | $\chi^2_{\rm min}$ |
|---|---|---|---|---|
| $H(z)$ + SNIa + xA | $67.3 \pm 1.0$ | $0.201^{+0.017}_{-0.014}$ | $-19.43 \pm 0.03$ | 2627.82 |
| & R21 | $71.1^{+0.7}_{-0.5}$ | $0.175^{+0.012}_{-0.013}$ | $-19.32 \pm 0.02$ | 2652.04 |
| & P18 | $67.4 \pm 0.4$ | $0.202^{+0.014}_{-0.013}$ | $-19.42 \pm 0.01$ | 2627.82 |
| & F20 | $69.1 \pm 0.5$ | $0.188^{+0.014}_{-0.012}$ | $-19.375 \pm 0.02$ | 2632.91 |
| & GD3 | $70.6^{+0.7}_{-0.8}$ | $0.178^{+0.014}_{-0.013}$ | $-19.34 \pm 0.02$ | 2651.11 |
| & ACT | $67.5^{+0.8}_{-0.7}$ | $0.199^{+0.016}_{-0.013}$ | $-19.42 \pm 0.02$ | 2628.01 |
| $H(z)$ + SNIa + BAO + xA | $64.2 \pm 0.6$ | $0.291^{+0.011}_{-0.013}$ | $-19.49 \pm 0.02$ | 2675.19 |
| & R21 | $67.6 \pm 0.5$ | $\left(257.7^{+9.1}_{-10.0}\right) \times 10^{-3}$ | $-19.39 \pm 0.02$ | 2772.13 |
| & P18 | $66.4^{+0.3}_{-0.4}$ | $\left(269.0^{+9.7}_{-8.9}\right) \times 10^{-3}$ | $-19.42 \pm 0.01$ | 2697.35 |
| & F20 | $67.0 \pm 0.4$ | $\left(262.7^{+9.6}_{-9.0}\right) \times 10^{-3}$ | $-19.41 \pm 0.01$ | 2725.01 |
| & GD3 | $66.5^{+0.6}_{-0.5}$ | $0.267 \pm 0.010$ | $-19.42 \pm 0.02$ | 2748.71 |
| & ACT | $65.0 \pm 0.5$ | $0.282^{+0.011}_{-0.010}$ | $-19.46 \pm 0.02$ | 2684.88 |

Table 4.14: $f_4(T)$ model (2.26) constraints for the combination $H(z)$ measurements, SNIa compilation, and with both BAO surveys. We include the QSO xA sample.

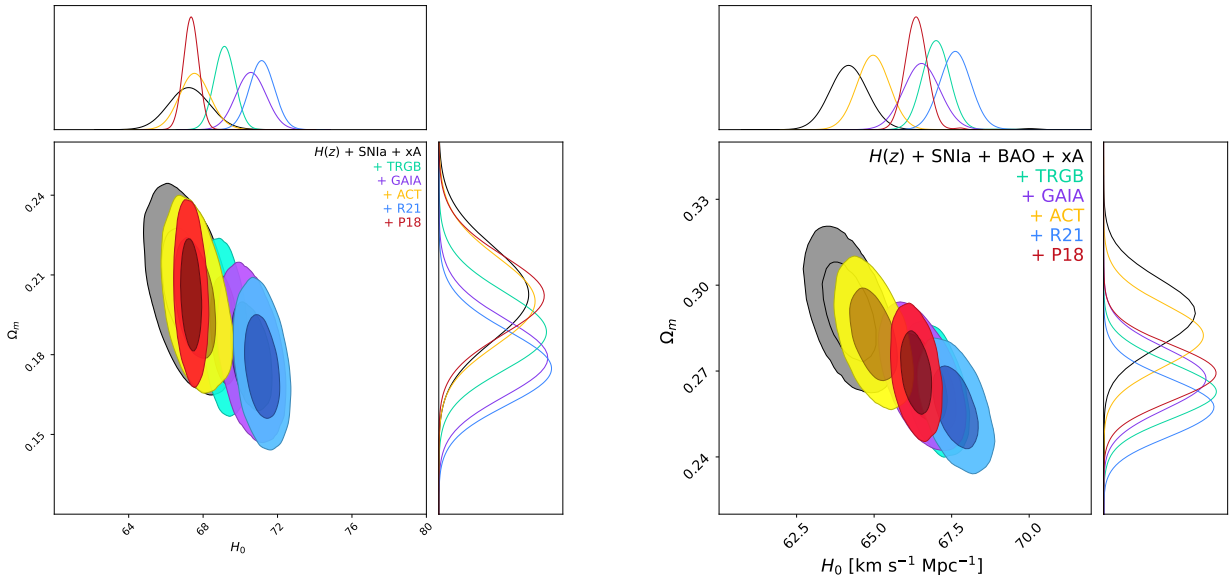


(a) (b)

Figure 4.14: C.L posterior results using the $f_4(T)$ model (2.26) for the *(a)* $H(z)$ and SNIa Pantheon compilation with the QSO xA sample, and *(b)* the combination including the BAO sample. The shadowed regions correspond to $1\sigma$ and $2\sigma$, respectively. We use the color code blue for R21 prior, purple for GAIA, red for P18, green for F20, and yellow for ACT. Additionally, the model that was tested with flat prior is represented in black color..

| Data Set | $H_0$ [km s$^{-1}$ Mpc$^{-1}$] | $\Omega_m$ | $M$ | $\beta'$ | $\chi^2_{\rm min}$ |
|---|---|---|---|---|---|
| $H(z)$ + SNIa + nUVX | $71.4^{+2.4}_{-2.0}$ | $\left(196.3^{+6.5}_{-6.1}\right) \times 10^{-3}$ | $-19.31 \pm 0.03$ | $-10.7^{+8.5}_{-7.2}$ | 3404.16 |
| & R21 | $73.3^{+0.7}_{-0.8}$ | $(197.3 \pm 2.7) \times 10^{-3}$ | $-19.25 \pm 0.02$ | $-10.7^{+0.7}_{-0.9}$ | 3405.16 |
| & P18 | $67.4 \pm 0.4$ | $\left(198.0^{+6.3}_{-6.4}\right) \times 10^{-3}$ | $-19.43 \pm 0.01$ | $-11.3^{+0.9}_{-0.6}$ | 3405.14 |
| & F20 | $69.8^{+0.5}_{-0.6}$ | $\left(1972.1^{+8.7}_{-9.3}\right) \times 10^{-4}$ | $-19.35 \pm 0.02$ | $-10.8^{+0.7}_{-0.8}$ | 3408.23 |
| & GD3 | $73.8^{+0.9}_{-1.0}$ | $\left(195.9^{+3.0}_{-0.0}\right) \times 10^{-3}$ | $-19.23 \pm 0.03$ | $-10.4^{+0.7}_{-0.9}$ | 3405.06 |
| & ACT | $68.2^{+0.9}_{-1.2}$ | $\left(197.6^{+4.5}_{-5.3}\right) \times 10^{-3}$ | $-19.40^{+0.03}_{-0.04}$ | $-10.9 \pm 0.8$ | 3407.80 |
| $H(z)$ + SNIa + BAO + nUVX | $63.7 \pm 0.7$ | $0.295 \pm 0.012$ | $-19.50 \pm 0.02$ | $-10.79^{+1.61}_{-1.87}$ | 3153.12 |
| & R21 | $68.2^{+0.5}_{-0.6}$ | $(260.0 \pm 9.5) \times 10^{-3}$ | $-19.37 \pm 0.02$ | $-10.7^{+1.25}_{-1.24}$ | 3246.22 |
| & P18 | $66.5^{+0.3}_{-0.4}$ | $\left(272.9^{+9.2}_{-9.5}\right) \times 10^{-3}$ | $-19.42 \pm 0.01$ | $-10.65^{+1.52}_{-1.87}$ | 3176.16 |
| & F20 | $67.3^{+0.5}_{-0.4}$ | $\left(266.5^{+9.8}_{-10.3}\right) \times 10^{-3}$ | $-19.39 \pm 0.02$ | $-11.12^{+1.67}_{-1.75}$ | 3201.93 |
| & GD3 | $66.9 \pm 0.6$ | $\left(268.9^{+10.2}_{-9.6}\right) \times 10^{-3}$ | $-19.40 \pm 0.02$ | $-10.24^{+1.62}_{-1.71}$ | 3226.86 |
| & ACT | $64.8^{+0.6}_{-0.5}$ | $0.285^{+0.011}_{-0.010}$ | $-19.46 \pm 0.02$ | $-12.11^{+1.86}_{-1.50}$ | 3164.54 |

Table 4.15: $f_4(T)$ model (2.26) constraints for the baseline $H(z)$ measurements, SNIa compilation, and BAO sample. We include the QSO nUVX sample.

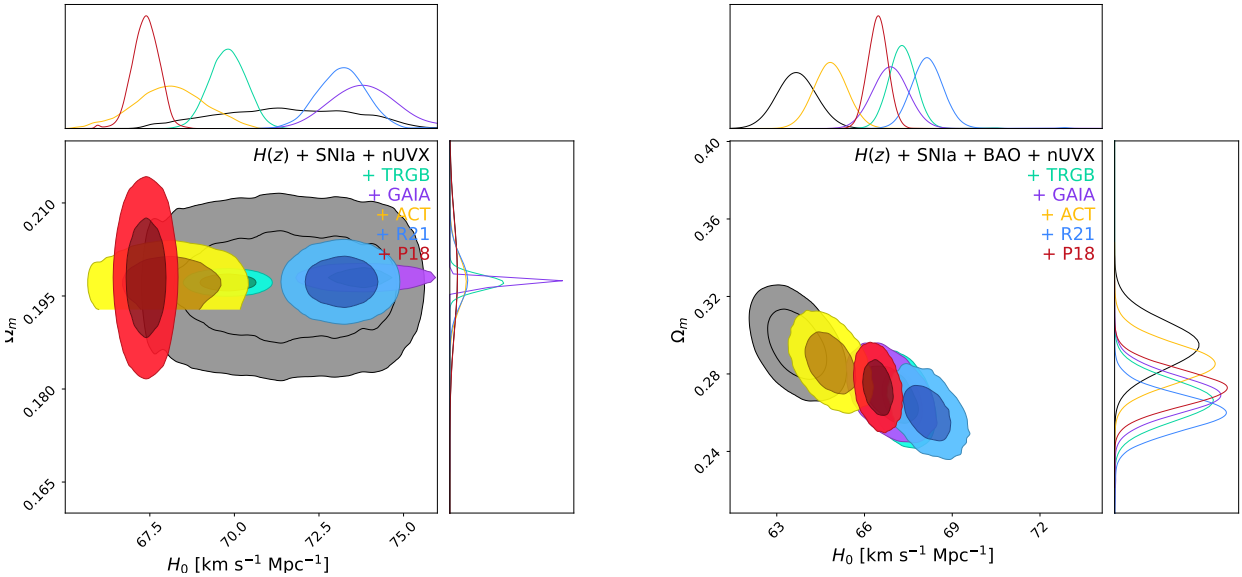


(a) (b)

Figure 4.15: C.L posterior results for the $f_4(T)$ model (2.26) for the combinations *(a)* $H(z)$ and SNIa Pantheon compilation with the QSO nUVX sample, and *(b)* the combination with the BAO sample. The shadowed regions correspond to $1\sigma$ and $2\sigma$, respectively. We use the color code blue for R21 prior, purple for GAIA, red for P18, green for F20, and yellow for ACT. Additionally, the model that was tested with flat prior is represented in black color.

Using the QSO nUVX sample, the constraints for this model have a similar impact to the QSO xA sample. Using $H(z)$ and SNIa baseline, we obtain a value of $H_0 = 71.4^{+2.4}_{-2.0}$ km s$^{-1}$ Mpc$^{-1}$ that reduces the tension but with a large uncertainty. With the other priors, we have similar effects

in comparison to previous models as the R21 and GD3 priors tend to have the larger $H_0$ value estimations and both the ACT and P18 priors tend to have the lowest. For the F20 prior we have an intermediate value around $H_0 = 70$ km s$^{-1}$ Mpc$^{-1}$

Considering the BAO sample makes the fractional matter density grow up to $\Omega_m \lesssim 0.3$ for all the applied priors and reduces the value of $H_0$ down to $H_0 = 64.8^{+0.6}_{-0.5}$ km s$^{-1}$ Mpc$^{-1}$ using the ACT prior and being the highest value with the R21 prior $H_0 = 68.2^{+0.5}_{-0.6}$ km s$^{-1}$ Mpc$^{-1}$.

In the Logarithmic model the estimation of the $\chi^2_{\rm min}$ value is crucial since we lack a set of values that allow us to directly contrast the results with the ΛCDM model. In this scenario, the values are higher than those of the standard cosmological model. However, for all combinations of data, the parameter estimation is smaller which is expected for a model with less free parameters than the previous. The remaining trends persist for both BAO, which increases the numerical value of $\chi^2_{\rm min}$, and for the xA and nUVX samples, maintaining their behavior where better parameter estimation does not necessarily imply a better $\chi^2_{\rm min}$.

## 4.7 General remarks

On one hand, using local baselines provides a raising on the value of $H_0$ which tends to prefer a lower value of $\Omega_m$ to preserve the quantity $\Omega_m h^2$, i.e. the geometric degeneracy (Abdalla et al., 2022). Several facts on these constraints are present in all combinations between the local catalogs including the Quasar samples.

Using SNIa and $H(z)$ measurements was not sufficient to estimate the value of $H_0$ as the error estimation is bigger than the one obtained with other measurements.

This error estimation is consistent with literature as there is a degeneracy present in the $H_0 - M$ parameter space for SNIa compilation (Riess et al., 2021b). This degeneracy is a product of the estimations of the distance modulus as $\mu = m - M$ which will act as a zero-point calibration (Bargiacchi et al., 2022). One of the ways to avoid this problem is to leave some fixed value for the absolute magnitude $M$ with the implication of already assuming an $H_0$ value and therefore a preferred cosmology.

On the other hand, we notice that the reason why we chose to analyze the baseline without the BAO sample is because the latter is a cosmology-dependent catalog, therefore, the conversion from angles and redshifts to distances in the calculations or through the assumptions of fiducial cosmology creates a baseline that can be used to fit the model, but not localize a deviation from the model used as a prior. In this line of thought, the estimation of the Hubble parameter $H(z)$, and the angular diameter distance $D_A(z)$, for the BAO sample needs the radial distance $dr_{||} = c\delta z/H(z)$, and the transverse distance $dr_\perp = (1+z)D_A\theta$ (with $\theta = \frac{(1+z)r_s}{D_A(z)}$. From these relations the measured angular scale of the sound horizon at the drag epoch depends on the cosmological assumption made (Perivolaropoulos and Skara, 2022; Abdalla et al., 2022). However, the problem with the determination of these parameters and the physical quantities from BAO measurements (see Sec.3.4) is that this observable prefers values setting at early cosmic times, so the distance at the drag epoch has an existing issue known as the $H_0 - r_s(z_d)$ tension, which impacts our estimations of the Hubble constant $H_0$. In our analysis of all the cosmological models discussed, we notice that the estimation of the $H_0$ is always lower using the BAO sample. Furthermore, in the literature $H_0 - r_s(z_d)$ is considered as a combined parameter in the triplet $H_0 - r_s(z_d) - \Omega_m$ (L'Huillier and Shafieloo, 2017; Abdalla et al., 2022). Knowing these data characteristics is now

clear that the trend about $H_0$ using the BAO catalogs in all models and baseline, is biased through the calculation of $r_s(z_d)$. This highly depends on the chosen values for $\Omega_{\gamma,0}h^2$ and $\Omega_{b,0}h^2$.

The first step for testing the different models was to use the flat priors in $H_0$, inducing that the data chooses the preferred $H_0$ without a bias introduced using the prior.

Using the flat prior is clear that both SNIa, $H(z)$ measurements and QSO nUVX sample have the biggest error determination for the Hubble constant $H_0$. This is interesting as using nUVX with both $f_2(T)$ and $f_3(T)$ models the sample seems to be alleviating the $H_0$ tension to $2\sigma$. On the contrary, using the QSO xA sample results in low $H_0$ values in agreement with the Planck 2018 estimations (Aghanim et al., 2020b) for all the tested models. The results can be found in Figure 4.16.

Regarding the aforementioned issues of the $H_0$ estimation is that we decided to introduce Gaussian priors to constrain the rest of the parameter space allowing us to seek any possible influence from the Hubble tension. We consider five different priors reported in the literature shown in section 4.1.

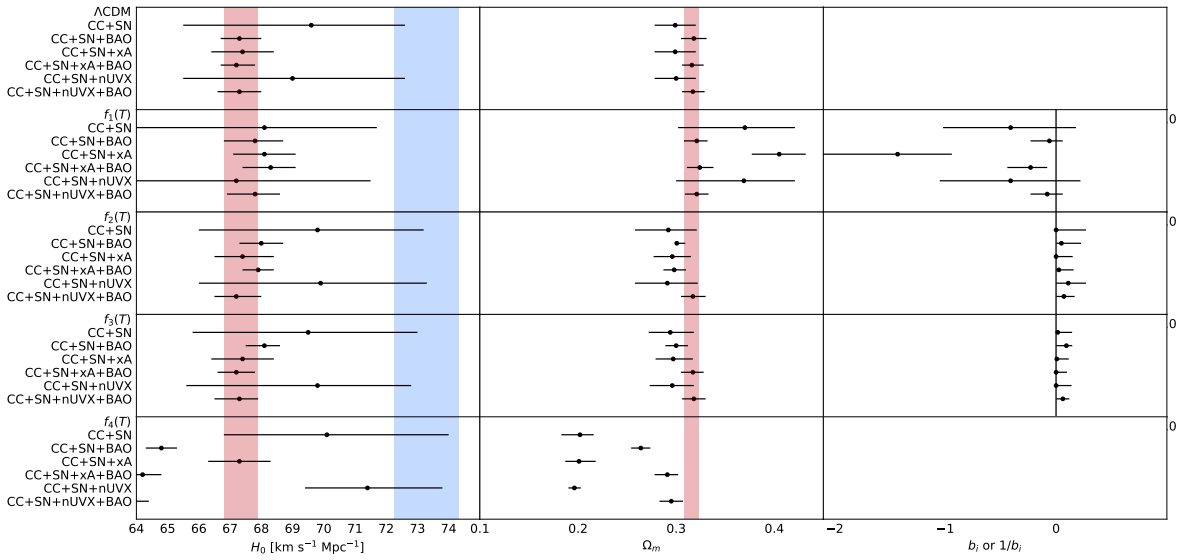


Figure 4.16: Whisker plot for the flat $H_0$ priors. The highlighted vertical C.L represents the R21 prior (blue) and the P18 prior (red). The black solid line in $f_1(T)$, $f_2(T)$ and $f_3(T)$ represents the value in which the free parameter $b_i$ or $1/b_i$ in the different models reproduces the ΛCDM model behavior. CC refers to $H(z)$ measurements and SN refers to the SNIa Pantheon catalog.

The results from the R21 (Riess et al., 2022) prior are shown in figure 4.17 where is clear that using $H(z)$ measurements, SNeIa, and the nUVX sample the value of $H_0$ adopted is the imposed by the prior.

This is in contrast with the results obtained with the QSO xA sample and BAO results that reduce the $H_0$ value to a closer to the estimations of Planck 2018 (Aghanim et al., 2020b). Here is interesting to notice that the usage of BAO and QSO xA obtain values for the free parameter that represent a deviation from the ΛCDM model of more than $2\sigma$ for the $f_1(T)$ model. The rest

of the combination of the different datasets mimic the behavior of ΛCDM model as $1/b_i \approx 0$ at $2\sigma$ level.

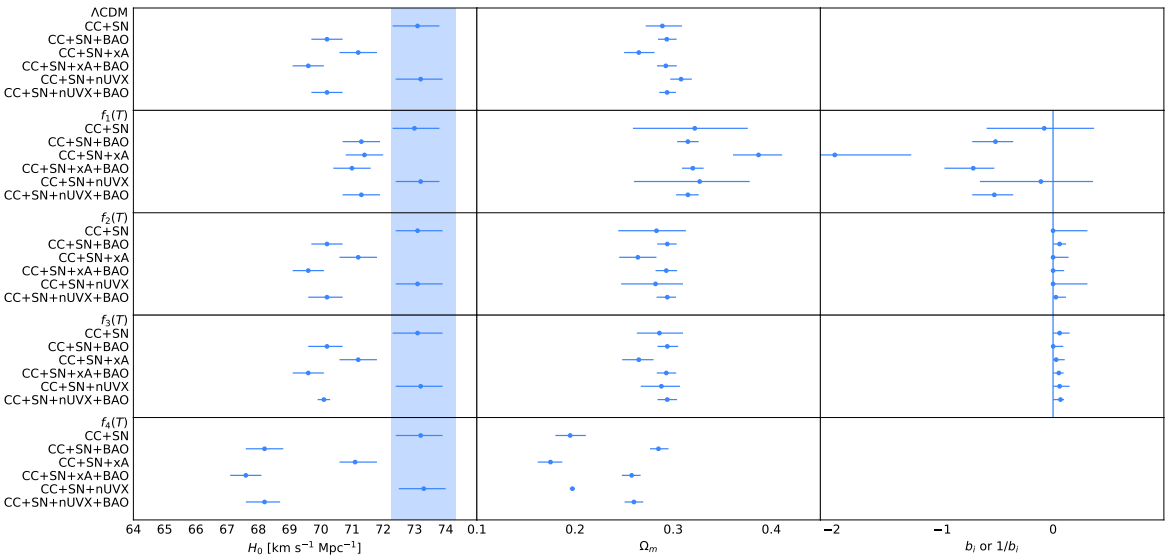


Figure 4.17: Whisker plot for the R21 $H_0$ priors. The blue line in $f_1(T)$, $f_2(T)$ and $f_3(T)$ represents the value in which the free parameter $b_i$ or $1/b_i$ in the different models reproduces the ΛCDM model behavior. CC refers to $H(z)$ measurements and SN refers to the SNIa Pantheon catalog.

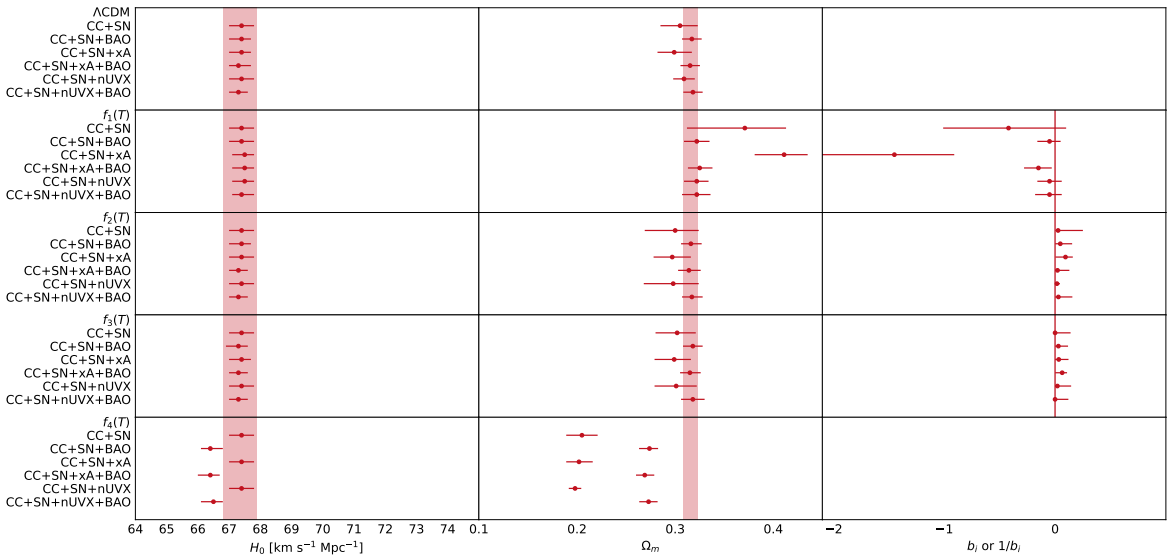


Figure 4.18: Whisker plot for the P18 $H_0$ priors. The red line in $f_1(T)$, $f_2(T)$ and $f_3(T)$ represents the value in which the free parameter $b_i$ or $1/b_i$ in the different models reproduces the ΛCDM model behavior. CC refers to $H(z)$ measurements and SN refers to the SNIa Pantheon catalog.

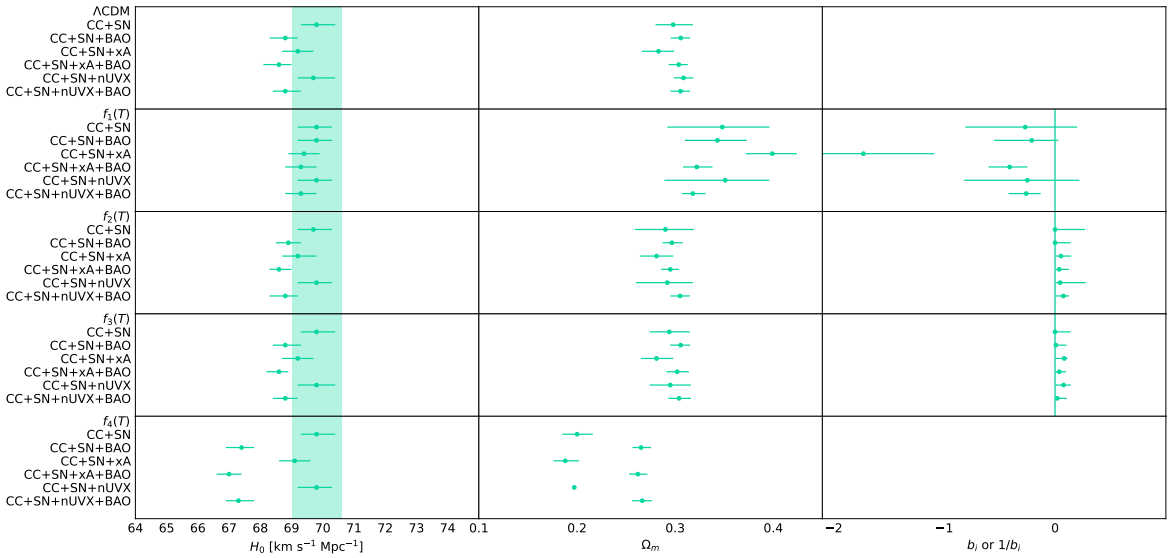


Figure 4.19: Whisker plot for the F20 $H_0$ priors. The red line in $f_1(T)$, $f_2(T)$ and $f_3(T)$ represents the value in which the free parameter $b_i$ or $1/b_i$ in the different models reproduces the ΛCDM model behavior. CC refers to $H(z)$ measurements and SN refers to the SNIa Pantheon catalog.

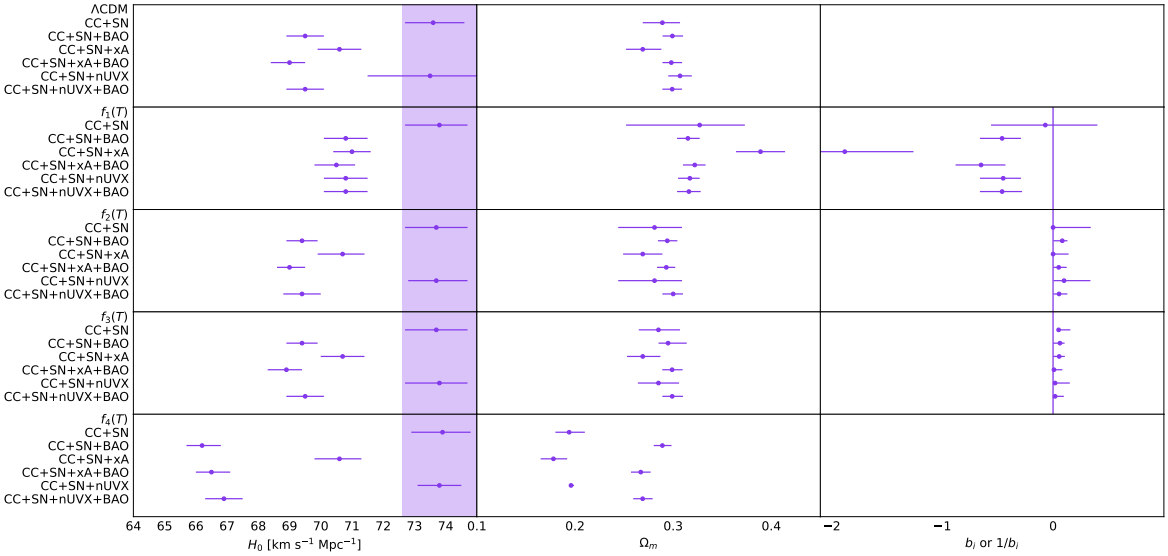


Figure 4.20: Whisker plot for the GAIA $H_0$ priors. The purple line in $f_1(T)$, $f_2(T)$ and $f_3(T)$ represents the value in which the free parameter $b_i$ or $1/b_i$ in the different models reproduces the $\Lambda$CDM model behavior. CC refers to $H(z)$ measurements and SN refers to the SNIa Pantheon catalog.

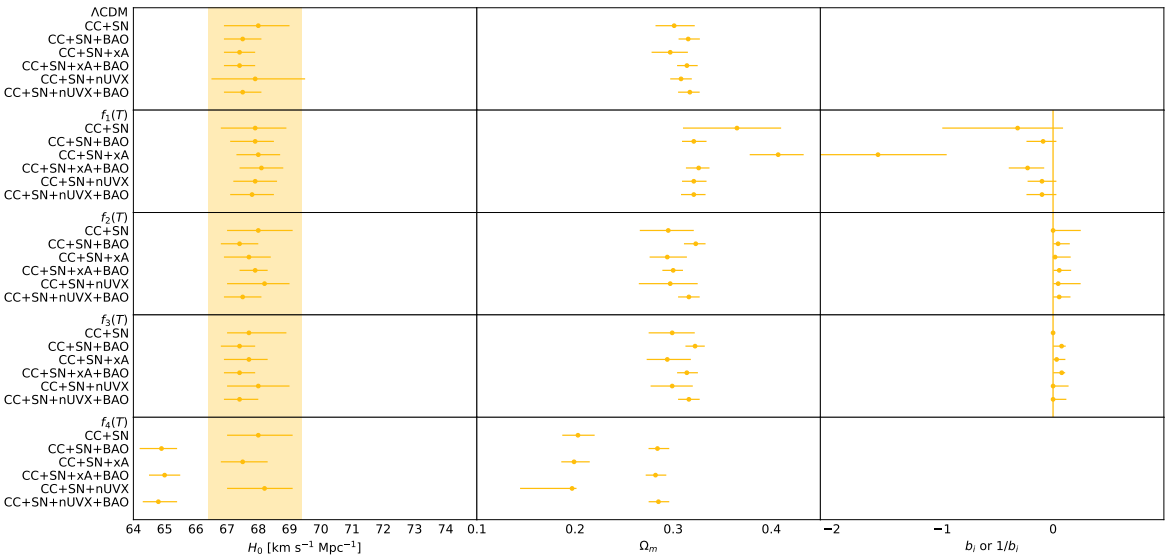


Figure 4.21: Whisker plot for the ACT $H_0$ priors. The yellow line in $f_1(T)$, $f_2(T)$ and $f_3(T)$ represents the value in which the free parameter $b_i$ or $1/b_i$ in the different models reproduces the ΛCDM model behavior. CC refers to $H(z)$ measurements and SN refers to the SNIa Pantheon catalog.

The P18 prior results are shown in Figure 4.18, where is clear that the value preferred for $H_0$ is the one imposed by the prior for every model and dataset combination. It is important to note that the estimations for the fractional matter density $\Omega_m \approx 0.2$ for $f_4(T)$ model, while the rest of the parameters behave as ΛCDM at $2\sigma$. The only noted deviation is present using the combination $H(z)$, SNIa, and QSO xA sample with $f_2(T)$ model where more than a $2\sigma$ deviations are found for the free parameter $1/b_2$.

The rest of the priors imposed on the parameters are shown in Figures 4.19, 4.21, and 4.20.

# Chapter 5

# Conclusions

In this thesis we introduced the General Relativity and the standard cosmology in Chapter 1, including a description of the quantities involved in the theory, the mathematical formalism and we perform a summary in the state-of-the-art about the cosmological tensions 1.1.2. This allowed us to introduce the concept of extensions and modifications on the gravitational theory 1.2. We discussed in detail the TEGR approach introducing the cosmological viable $f(T)$ models 2. In Chapter 3 we revisited the employed cosmological observations to constraint the cosmological parameters for the $f(T)$ models including the two Quasar samples. Finally in Chapter 4 we presented the results for the constraints in those viable $f(T)$ models.

So, in this Thesis, we perform statistical analyses with two new samples of Quasars with different detection methods to standardize types of AGNs. Along with the standard local observables, such as SNIa and $H(z)$ measurements, we found new constraints for $f(T)$ viable cosmologies at higher redshifts, showing notable deviations from the ΛCDM model and relaxing the tension on $H_0$.

The xA sample of Quasars (Marziani and Sulentic, 2014; Negrete et al., 2018; Dultzin et al., 2020) is based on a spectroscopic approach to identify objects whose emission from accretion from near the black hole is very close to the Eddington luminosity limit, allowing us to use them as standard candle using various cosmological model-independent assertions. This sample is composed of 220 data points consisting of redshift and distance modulus $\mu$ determined using the black hole mass-luminosity relation, the hydrogen ionizing photons, and the hydrogen number density. The focus of the nUVX sample (Lusso et al., 2020), on the other hand, is the non-linear relationship between the ultraviolet emission at 2500 A and the X-ray flux measured at 2 keV to obtain the luminous distance independently of the cosmological model and allow us to achieve a redshift of up to $z \sim 7$, that may be the result of the X-ray emission of the corona of the accretion disk (Risaliti et al., 2023) although at the time of writing it is still considered an empirical relationship for which an explanation is still being sought. nUVX consists of 2422 data points consisting of fluxes for X-ray and UV from which the luminosity distance is calculated. These two different samples of Quasars were treated independently to make a comparison between the two distance calculation methodologies.

These two data samples have previously been used in the literature only to test dark energy parameterisations and to test curvature models (Bargiacchi et al., 2022) and the vanilla ΛCDM. This work is the first time that Quasar samples are used for extended gravity analyses.

In this work, we presented the constraints on TEGR $f(T)$ models by adding these two new

Quasar observables. Although this work was carried out in an attempt to constraint the free parameter from the different teleparallel $f(T)$ models, it was clear that almost every combination of probes and priors returned the confirmation for ΛCDM at least for the early values of $H_0$, especially for the xA sample, where for almost every used prior deviates from ΛCDM in more than $2\sigma$ but in the rest of the models and priors had the impact of lowering the $H_0$ value.

In the direction of the Hubble tension, some results could be indicators that the usage of more local distance measurements of this kind may reduce the value of $H_0$ as a result and therefore reduce the tension down to $2\sigma$. This can be seen most clearly by looking at the results for prior P18 shown in figure 4.18 where almost all the combinations of data sets return the expected $H_0$ value with all the models. However, this is not a conclusive result since both the BAO data and it could be that some cosmological model-dependent element is hidden within the assumptions for generating the Quasar samples and is therefore preferring values close to the $H_0$ of the standard Planck cosmology.

This is why we consider the results shown in works such as Bargiacchi et al. (2022) to be biased since they assume a fixed value of $H_0 = 70$ with which cosmology already has a value it will prefer, so introducing different models involving curvature or dark energy parameterisations will tend to lead to deviations if complete freedom in the fit is not allowed. This is why the nUVX sample was included allowing the $H_0$ value to vary in the parameter space, thus allowing us to contrast the results obtained above at least for standard cosmology.

Within the conducted analysis for this thesis, it is important to exhibit that the two Quasar samples show a notable dispersion when compared to other cosmological tests, such as SNIa. This is because, for the xA sample, the physical process behind the construction of the luminous distance measurement is reasonably well understood (Marziani and Sulentic, 2014). However, for the nUVX sample, reasons for the existence of the relationship between X-ray and UV emission as a measurement of the coronal gas in the accretion disk region are still under consideration (Signorini et al., 2023). Hence, a comprehensive understanding of the physical processes that led to the mentioned relations in the selected AGN samples is crucial to continue employing them in cosmology.

Efforts have been made to reduce the dispersion in the xA sample, as documented in (Negrete et al., 2018), where corrections for object orientation are used to address potential effects on distance estimation influenced by dust obscuration.

As a perspective for this work, looking now to perform the perturbative calculations to be able to use other CMB-based data sets such as Planck (Aghanim et al., 2020b) or ACT (Aiola et al., 2020) that allow a more complete fit and that comply with covering all possible data sets from both the early and late Universe is essential for further progress in teleparallel gravity, incorporating this calculation in existing computational codes that allow us to perform the necessary analyses. This work could also be extended to more models of gravity extensions either within TEGR itself or in other approaches presented previously in the text. In addition to this, the incorporation of new data sets such as the updated SNeIa Pantheon+ sample (Riess et al., 2021b), that is necessary to keep fit with the state-of-the-art cosmology probes. Within this update of the data, it would also be interesting to incorporate new Quasar data of the same type of processing as that carried out to obtain the xA sample and an eventual update of the nUVX sample. Finally, another proposed data set from AGNs could be the use of distance estimation using the reverberation mapping technique (Watson et al., 2011) that is also a model-independent distance estimator.

# Appendices

# Appendix A

# On the $H(z)$ covariance matrix

The standard usage of the $H(z)$ measurements in precision cosmology is to incorporate the systematical error band in the calculation of the $\chi^2$. This means that the usual way is:

$$\chi^2 = \sum_i^N \left[ \frac{(H(z_i, \Theta) - H_i)^2}{\sigma_H^2} \right], \tag{A.1}$$

where $\sigma_H$ is the systematical error, $H(z_i, \Theta)$ are the calculated Hubble function for every redshift and $H_i$ are the observations reported, in addition $N$ is the total number of the observations. The not-so-recent novelty we are introducing in this work is the usage of the covariance matrix for this measurement given by Moresco et al. (2020). This means that the new $\chi^2$ that we will use is given as (3.4) and this has important effects on the posteriors obtained for the cosmological tested models. The covariance matrix is expressed as:

$$\mathrm{Cov}_{ij} = \mathrm{Cov}_{ij}^{\mathrm{stat}} + \mathrm{Cov}_{ij}^{\mathrm{young}} + \mathrm{Cov}_{ij}^{\mathrm{model}} + \mathrm{Cov}_{ij}^{\mathrm{met}}; \tag{A.2}$$

where the different contributions of the statistical errors are informed through the upper indexes including the statistical error, the young component contamination, the stellar metallicity determination error, and the dependence on the chosen model for evolution determination. The model part can be decomposed in the error including the Stellar Formation History (SFH), the Initial Mass function, and both the stellar library and the stellar synthetic characteristics (Moresco et al., 2020). This means that using the full covariance matrix will give us a better approximation for the true errors of the $H(z)$ measurements. The prize to pay is that this matrix will result in more uncertainty than the original method because it takes account in the different systematic errors for the methods and simulations needed.

In figure A.1 the effect of introducing the new likelihood compared to the previous one is observed for the $\Lambda$CDM model, where both $H_0$ and $\Omega_m$ are estimated with less certainty, which is an expected result. In figure A.2 the effect is also shown when both the $H(z)$ and SNe measurements are included in the analyses, where a correlation between the $H_0$ and $\Omega_m$ begins to occur and can be the explanation between the light correlation between the same two parameters in the analyses in the text.

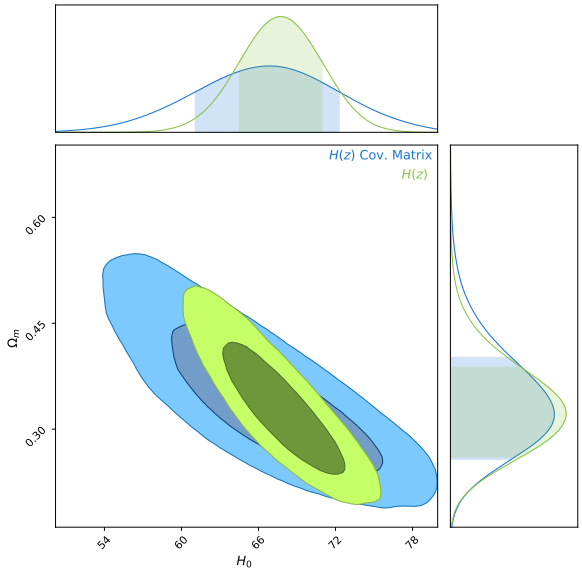


Figure A.1: Comparison between the usage of the full covariance matrix for the $H(z)$ measurements (blue) and the use of only the statistical error in the diagonal (green).

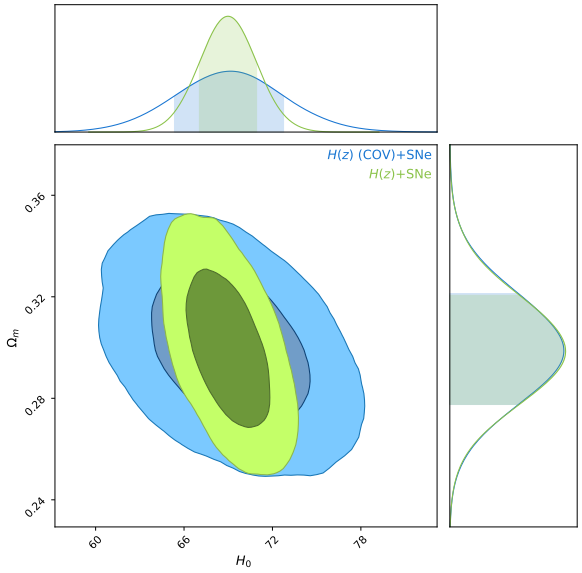


Figure A.2: Comparison between the usage of the full covariance matrix for the $H(z)$ measurements adding also the SNe data set (blue) and the use of only the statistical error in the diagonal with the SNe data set (green).

# Bibliography


[1] B. P. Abbott et al. Observation of Gravitational Waves from a Binary Black Hole Merger. *Phys. Rev. Lett.*, 116(6):061102, 2016. doi:10.1103/PhysRevLett.116.061102.

[2] B. P. Abbott et al. A gravitational-wave standard siren measurement of the Hubble constant. *Nature*, 551(7678):85–88, 2017a. doi:10.1038/nature24471.

[3] B. P. Abbott et al. GW170817: Observation of Gravitational Waves from a Binary Neutron Star Inspiral. *Phys. Rev. Lett.*, 119(16):161101, 2017b. doi:10.1103/PhysRevLett.119.161101.

[4] Elcio Abdalla et al. Cosmology intertwined: A review of the particle physics, astrophysics, and cosmology associated with the cosmological tensions and anomalies. *JHEAp*, 34:49–211, 2022. doi:10.1016/j.jheap.2022.04.002.

[5] Nakul Aggarwal, Ali Pourmand, Fatimah Shojai, and Harish Parthasarathy. Constraining Generalized Chaplygin Gas in Non-Minimally Coupled $f(Q)$ Cosmology using Quasars and $H(z)$ Data. 12 2022.

[6] N. Aghanim, Y. Akrami, F. Arroja, M. Ashdown, J. Aumont, C. Baccigalupi, M. Ballardini, A. J. Banday, R. B. Barreiro, and et al. Planck2018 results i. *Astronomy & Astrophysics*, 641:A1, Sep 2020a. ISSN 1432-0746. doi:10.1051/0004-6361/201833880. URL http://dx.doi.org/10.1051/0004-6361/201833880.

[7] N. Aghanim, Y. Akrami, M. Ashdown, J. Aumont, C. Baccigalupi, M. Ballardini, A. J. Banday, R. B. Barreiro, N. Bartolo, and et al. Planck 2018 results. *Astronomy and Astrophysics*, 641:A6, Sep 2020b. ISSN 1432-0746. doi:10.1051/0004-6361/201833910. URL http://dx.doi.org/10.1051/0004-6361/201833910.

[8] Simone Aiola et al. The Atacama Cosmology Telescope: DR4 Maps and Cosmological Parameters. *JCAP*, 12:047, 2020. doi:10.1088/1475-7516/2020/12/047.

[9] Andoni Aizpuru, Rubén Arjona, and Savvas Nesseris. Machine learning improved fits of the sound horizon at the baryon drag epoch. *Phys. Rev. D*, 104(4):043521, 2021. doi:10.1103/PhysRevD.104.043521.

[10] Kazunori Akiyama et al. First M87 Event Horizon Telescope Results. I. The Shadow of the Supermassive Black Hole. *Astrophys. J. Lett.*, 875:L1, 2019. doi:10.3847/2041-8213/ab0ec7.

[11] Kazunori Akiyama et al. First Sagittarius A* Event Horizon Telescope Results. I. The Shadow of the Supermassive Black Hole in the Center of the Milky Way. *Astrophys. J. Lett.*, 930(2):L12, 2022. doi:10.3847/2041-8213/ac6674.

[12] Yashar Akrami et al. *Modified Gravity and Cosmology: An Update by the CANTATA Network*. Springer, 2021. ISBN 978-3-030-83714-3, 978-3-030-83717-4, 978-3-030-83715-0. doi:10.1007/978-3-030-83715-0.

[13] Shadab Alam et al. The clustering of galaxies in the completed SDSS-III Baryon Oscillation Spectroscopic Survey: cosmological analysis of the DR12 galaxy sample. *Mon. Not. Roy. Astron. Soc.*, 470(3):2617–2652, 2017. doi:10.1093/mnras/stx721.

[14] Shadab Alam et al. Completed SDSS-IV extended Baryon Oscillation Spectroscopic Survey: Cosmological implications from two decades of spectroscopic surveys at the Apache Point Observatory. *Phys. Rev. D*, 103(8):083533, 2021. doi:10.1103/PhysRevD.103.083533.

[15] Ruben Aldrovandi and José Geraldo Pereira. *Teleparallel Gravity: An Introduction*. Springer, 2013. ISBN 978-94-007-5142-2, 978-94-007-5143-9. doi:10.1007/978-94-007-5143-9.

[16] Pablo M. Maldonado Alonso, Celia Escamilla-Rivera, and Rodrigo Sandoval-Orozco. Constraining dark energy cosmologies with spatial curvature using Supernovae JWST forecasting. 9 2023.

[17] Luca Amendola and Shinji Tsujikawa. *Dark Energy: Theory and Observations*. ial xn–3ug : xn–2ug Cambridge University Press, Cambridge, England, UK, June 2010. ISBN 978-0-52151600-6. URL https://www.amazon.com.mx/Dark-Energy-Observations-Luca-Amendola/dp/0521516005.

[18] A. Arbey and F. Mahmoudi. Dark matter and the early Universe: a review. *Prog. Part. Nucl. Phys.*, 119:103865, 2021. doi:10.1016/j.ppnp.2021.103865.

[19] Marika Asgari et al. KiDS-1000 Cosmology: Cosmic shear constraints and comparison between two point statistics. *Astron. Astrophys.*, 645:A104, 2021. doi:10.1051/0004-6361/202039070.

[20] Sebastian Bahamonde, Konstantinos F. Dialektopoulos, Celia Escamilla-Rivera, Gabriel Farrugia, Viktor Gakis, Martin Hendry, Manuel Hohmann, Jackson Levi Said, Jurgen Mifsud, and Eleonora Di Valentino. Teleparallel gravity: From theory to cosmology, 2021.

[21] Michael L. Balogh, S. L. Morris, H. K. C. Yee, R. G. Carlberg, and E. Ellingson. Differential galaxy evolution in cluster and field galaxies at z=0.3. *Astrophys. J.*, 527:54–79, 1999. doi:10.1086/308056.

[22] Kazuharu Bamba, Chao-Qiang Geng, Chung-Chi Lee, and Ling-Wei Luo. Equation of state for dark energy in $f(T)$ gravity. *JCAP*, 01:021, 2011. doi:10.1088/1475-7516/2011/01/021.

[23] Eduardo Banados et al. An 800-million-solar-mass black hole in a significantly neutral Universe at redshift 7.5. *Nature*, 553(7689):473–476, 2018. doi:10.1038/nature25180.

[24] Eduardo Banados et al. The Discovery of a Highly Accreting, Radio-loud Quasar at $z = 6.82$. *Astrophys. J.*, 909(1):80, 2021. doi:10.3847/1538-4357/abe239.

[25] G. Bargiacchi, M. Benetti, S. Capozziello, E. Lusso, G. Risaliti, and M. Signorini. Quasar cosmology: dark energy evolution and spatial curvature. *Mon. Not. Roy. Astron. Soc.*, 515 (2):1795–1806, 2022. doi:10.1093/mnras/stac1941.

[26] G. Bargiacchi, M. G. Dainotti, S. Nagataki, and S. Capozziello. Gamma-Ray Bursts, Quasars, Baryonic Acoustic Oscillations, and Supernovae Ia: new statistical insights and cosmological constraints. 3 2023. doi:10.1093/mnras/stad763.

[27] Bruno J. Barros, Tiago Barreiro, Tomi Koivisto, and Nelson J. Nunes. Testing $F(Q)$ gravity with redshift space distortions. *Phys. Dark Univ.*, 30:100616, 2020. doi:10.1016/j.dark.2020.100616.

[28] Bruce A. Bassett and Renee Hlozek. Baryon Acoustic Oscillations. *Dark energy: observational and theoretical approaches*, 10 2009.

[29] Daniel Baumann. *Cosmology*. ial xn–3ug : xn–2ug Cambridge University Press, Cambridge, England, UK, August 2022. ISBN 978-1-10883807-8. URL https://www.amazon.com/-/es/Daniel-Baumann/dp/1108838073.

[30] Volker Beckmann and Chris R. Shrader. *Active Galactic Nuclei*. Wiley, 2012.

[31] Enis Belgacem, Yves Dirian, Andreas Finke, Stefano Foffa, and Michele Maggiore. Gravity in the infrared and effective nonlocal models. *JCAP*, 04:010, 2020. doi:10.1088/1475-7516/2020/04/010.

[32] Gabriel R. Bengochea and Rafael Ferraro. Dark torsion as the cosmic speed-up. *Phys. Rev. D*, 79:124019, 2009. doi:10.1103/PhysRevD.79.124019.

[33] C. L. Bennett, D. Larson, J. L. Weiland, N. Jarosik, G. Hinshaw, N. Odegard, K. M. Smith, R. S. Hill, B. Gold, M. Halpern, and et al. Nine-year wilkinson microwave anisotropy probe ( wmap ) observations: Final maps and results. *The Astrophysical Journal Supplement Series*, 208(2):20, Sep 2013. ISSN 1538-4365. doi:10.1088/0067-0049/208/2/20. URL http://dx.doi.org/10.1088/0067-0049/208/2/20.

[34] Jose Luis Bernal, Licia Verde, and Adam G. Riess. The trouble with $H_0$. *JCAP*, 10:019, 2016. doi:10.1088/1475-7516/2016/10/019.

[35] Florian Beutler, Chris Blake, Matthew Colless, D. Heath Jones, Lister Staveley-Smith, Lachlan Campbell, Quentin Parker, Will Saunders, and Fred Watson. The 6dF Galaxy Survey: baryon acoustic oscillations and the local Hubble constant. *Monthly Notices of the Royal Astronomical Society*, 416(4):3017–3032, 2011. doi:10.1111/j.1365-2966.2011.19250.x.

[36] C. Brans and R. H. Dicke. Mach's principle and a relativistic theory of gravitation. *Phys. Rev.*, 124:925–935, Nov 1961. doi:10.1103/PhysRev.124.925. URL https://link.aps.org/doi/10.1103/PhysRev.124.925.

[37] Rebecca Briffa, Celia Escamilla-Rivera, Jackson Said Levi, Jurgen Mifsud, and Nathan Lee Pullicino. Impact of $H_0$ priors on $f(T)$ late time cosmology. *Eur. Phys. J. Plus*, 137(5):532, 2022. doi:10.1140/epjp/s13360-022-02725-4.

[38] Rebecca Briffa, Celia Escamilla-Rivera, Jackson Levi Said, and Jurgen Mifsud. Constraints on f(T) cosmology with Pantheon+. *Mon. Not. Roy. Astron. Soc.*, 522(4):6024–6034, 2023a. doi:10.1093/mnras/stad1384.

[39] Rebecca Briffa, Celia Escamilla-Rivera, Jackson Levi Said, and Jurgen Mifsud. Growth of structures using redshift space distortion in $f(T)$ Cosmology. 10 2023b.

[40] Anthony GA Brown, Antonella Vallenari, T Prusti, JHJ De Bruijne, C Babusiaux, M Biermann, OL Creevey, DW Evans, L Eyer, A Hutton, et al. Gaia early data release 3-summary of the contents and survey properties. *Astronomy & Astrophysics*, 649:A1, 2021.

[41] Yi-Fu Cai, Salvatore Capozziello, Mariafelicia De Laurentis, and Emmanuel N. Saridakis. f(T) teleparallel gravity and cosmology. *Rept. Prog. Phys.*, 79(10):106901, 2016. doi:10.1088/0034-4885/79/10/106901.

[42] Salvatore Capozziello and Mariafelicia De Laurentis. Extended Theories of Gravity. *Phys. Rept.*, 509:167–321, 2011. doi:10.1016/j.physrep.2011.09.003.

[43] Zu-Cheng Chen, You Wu, and Hao Wei. Post-Newtonian Approximation of Teleparallel Gravity Coupled with a Scalar Field. *Nucl. Phys. B*, 894:422–438, 2015. doi:10.1016/j.nuclphysb.2015.03.012.

[44] Michel Chevallier and David Polarski. Accelerating universes with scaling dark matter. *Int. J. Mod. Phys. D*, 10:213–224, 2001. doi:10.1142/S0218271801000822.

[45] Timothy Clifton, Pedro G. Ferreira, Antonio Padilla, and Constantinos Skordis. Modified Gravity and Cosmology. *Phys. Rept.*, 513:1–189, 2012. doi:10.1016/j.physrep.2012.01.001.

[46] S. Contarini et al. Euclid: Cosmological forecasts from the void size function. *Astron. Astrophys.*, 667:A162, 2022. doi:10.1051/0004-6361/202244095.

[47] Richard H. Cyburt, Brian D. Fields, Keith A. Olive, and Tsung-Han Yeh. Big Bang Nucleosynthesis: 2015. *Rev. Mod. Phys.*, 88:015004, 2016. doi:10.1103/RevModPhys.88.015004.

[48] Rocco D'Agostino and Rafael C. Nunes. Measurements of $H_0$ in modified gravity theories: The role of lensed quasars in the late-time Universe. *Phys. Rev. D*, 101(10):103505, 2020. doi:10.1103/PhysRevD.101.103505.

[49] Maria Giovanna Dainotti, Giada Bargiacchi, Aleksander Łukasz Lenart, Shigehiro Nagataki, and Salvatore Capozziello. Quasars: Standard Candles up to z = 7.5 with the Precision of Supernovae Ia. *Astrophys. J.*, 950(1):45, 2023. doi:10.3847/1538-4357/accea0.

[50] Kyle S. Dawson, David J. Schlegel, Christopher P. Ahn, Scott F. Anderson, É ric Aubourg, Stephen Bailey, Robert H. Barkhouser, Julian E. Bautista, Alessandra Beifiori, Andreas A. Berlind, Vaishali Bhardwaj, Dmitry Bizyaev, Cullen H. Blake, Michael R. Blanton, Michael Blomqvist, Adam S. Bolton, Arnaud Borde, Jo Bovy, W. N. Brandt, Howard Brewington, Jon Brinkmann, Peter J. Brown, Joel R. Brownstein, Kevin Bundy, N. G. Busca, William Carithers, Aurelio R. Carnero, Michael A. Carr, Yanmei Chen, Johan Comparat, Natalia Connolly, Frances Cope, Rupert A. C. Croft, Antonio J. Cuesta, Luiz N.

da Costa, James R. A. Davenport, Timothée Delubac, Roland de Putter, Saurav Dhital, Anne Ealet, Garrett L. Ebelke, Daniel J. Eisenstein, S. Escoffier, Xiaohui Fan, N. Filiz Ak, Hayley Finley, Andreu Font-Ribera, R. Génova-Santos, James E. Gunn, Hong Guo, Daryl Haggard, Patrick B. Hall, Jean-Christophe Hamilton, Ben Harris, David W. Harris, Shirley Ho, David W. Hogg, Diana Holder, Klaus Honscheid, Joe Huehnerhoff, Beatrice Jordan, Wendell P. Jordan, Guinevere Kauffmann, Eyal A. Kazin, David Kirkby, Mark A. Klaene, Jean-Paul Kneib, Jean-Marc Le Goff, Khee-Gan Lee, Daniel C. Long, Craig P. Loomis, Britt Lundgren, Robert H. Lupton, Marcio A. G. Maia, Martin Makler, Elena Malanushenko, Viktor Malanushenko, Rachel Mandelbaum, Marc Manera, Claudia Maraston, Daniel Margala, Karen L. Masters, Cameron K. McBride, Patrick McDonald, Ian D. McGreer, Richard G. McMahon, Olga Mena, Jordi Miralda-Escudé, Antonio D. Montero-Dorta, Francesco Montesano, Demitri Muna, Adam D. Myers, Tracy Naugle, Robert C. Nichol, Pasquier Noterdaeme, Sebastián E. Nuza, Matthew D. Olmstead, Audrey Oravetz, Daniel J. Oravetz, Russell Owen, Nikhil Padmanabhan, Nathalie Palanque-Delabrouille, Kaike Pan, John K. Parejko, Isabelle Pâris, Will J. Percival, Ismael Pérez-Fournon, Ignasi Pérez-Ràfols, Patrick Petitjean, Robert Pfaffenberger, Janine Pforr, Matthew M. Pieri, Francisco Prada, Adrian M. Price-Whelan, M. Jordan Raddick, Rafael Rebolo, James Rich, Gordon T. Richards, Constance M. Rockosi, Natalie A. Roe, Ashley J. Ross, Nicholas P. Ross, Graziano Rossi, J. A. Rubiño-Martin, Lado Samushia, Ariel G. Sánchez, Conor Sayres, Sarah J. Schmidt, Donald P. Schneider, C. G. Scóccola, Hee-Jong Seo, Alaina Shelden, Erin Sheldon, Yue Shen, Yiping Shu, Anže Slosar, Stephen A. Smee, Stephanie A. Snedden, Fritz Stauffer, Oliver Steele, Michael A. Strauss, Alina Streblyanska, Nao Suzuki, Molly E. C. Swanson, Tomer Tal, Masayuki Tanaka, Daniel Thomas, Jeremy L. Tinker, Rita Tojeiro, Christy A. Tremonti, M. Vargas Magaña, Licia Verde, Matteo Viel, David A. Wake, Mike Watson, Benjamin A. Weaver, David H. Weinberg, Benjamin J. Weiner, Andrew A. West, Martin White, W. M. Wood-Vasey, Christophe Yeche, Idit Zehavi, Gong-Bo Zhao, and Zheng Zheng. THE BARYON OSCILLATION SPECTROSCOPIC SURVEY OF SDSS-III. *The Astronomical Journal*, 145(1):10, dec 2012. doi:10.1088/0004-6256/145/1/10. URL https://doi.org/10.1088%2F0004-6256%2F145%2F1%2F10.

[51] V. C. de Andrade, L. C. T. Guillen, and J. G. Pereira. Teleparallel spin connection. *Phys. Rev. D*, 64:027502, 2001. doi:10.1103/PhysRevD.64.027502.

[52] Eleonora Di Valentino, Olga Mena, Supriya Pan, Luca Visinelli, Weiqiang Yang, Alessandro Melchiorri, David F Mota, Adam G Riess, and Joseph Silk. In the realm of the hubble tension—a review of solutions *. *Classical and Quantum Gravity*, 38(15):153001, Jul 2021a. ISSN 1361-6382. doi:10.1088/1361-6382/ac086d. URL http://dx.doi.org/10.1088/1361-6382/ac086d.

[53] Eleonora Di Valentino et al. Snowmass2021 - Letter of interest cosmology intertwined IV: The age of the universe and its curvature. *Astropart. Phys.*, 131:102607, 2021b. doi:10.1016/j.astropartphys.2021.102607.

[54] Eleonora Di Valentino et al. Snowmass2021 - Letter of interest cosmology intertwined II: The hubble constant tension. *Astropart. Phys.*, 131:102605, 2021c. doi:10.1016/j.astropartphys.2021.102605.

[55] Scott Dodelson. *Modern cosmology: anisotropies and inhomogeneities in the universe*. Academic, 2002.

[56] Shen-Shi Du, Jun-Jie Wei, Zhi-Qiang You, Zu-Cheng Chen, Zong-Hong Zhu, and En-Wei Liang. Model-independent determination of H0 and ΩK, 0 using time-delay galaxy lenses and gamma-ray bursts. *Mon. Not. Roy. Astron. Soc.*, 521(4):4963–4975, 2023. doi:10.1093/mnras/stad696.

[57] Deborah Dultzin, Paola Marziani, J. A. de Diego, C. A. Negrete, Ascensión Del Olmo, Mary L. Martínez-Aldama, Mauro D'Onofrio, Edi Bon, Natasa Bon, and Giovanna M. Stirpe. Extreme quasars as distance indicators in cosmology. *Frontiers in Astronomy and Space Sciences*, 6:80, January 2020. doi:10.3389/fspas.2019.00080.

[58] K. El Bourakadi, B. Asfour, Z. Sakhi, Z. M. Bennai, and Taoufik Ouali. Primordial black holes and gravitational waves in teleparallel Gravity. *Eur. Phys. J. C*, 82(9):792, 2022. doi:10.1140/epjc/s10052-022-10762-7.

[59] Celia Escamilla-Rivera. Precision cosmology in modified and extended theories of gravity: An insightful test. *Astron. Nachr.*, 342(1-2):63–68, 2021. doi:10.1002/ASNA.202113882.

[60] Celia Escamilla-Rivera and Rubén Torres Castillejos. H0 Tension on the Light of Supermassive Black Hole Shadows Data. *Universe*, 9(1):14, 2023. doi:10.3390/universe9010014.

[61] Celia Escamilla Rivera and Carlo Vecchyo. *Cosmología De Precisión. Trazando La Forma Y Evolución Del Universo*. Prensas de Ciencias UNAM. ISBN: 978-607-30-6850-5, 2023.

[62] Celia Escamilla-Rivera, Ruth Lazkoz, Vincenzo Salzano, and Irene Sendra. Tension between SN and BAO: current status and future forecasts. *JCAP*, 09:003, 2011. doi:10.1088/1475-7516/2011/09/003.

[63] Celia Escamilla-Rivera, Geovanny A. Rave-Franco, and Jackson Levi Said. f(T, B) Cosmography for High Redshifts. *Universe*, 7(11):441, 2021. doi:10.3390/universe7110441.

[64] Valerio Faraoni and Salvatore Capozziello. *Beyond Einstein Gravity: A Survey of Gravitational Theories for Cosmology and Astrophysics*. Springer, Dordrecht, 2011. ISBN 978-94-007-0164-9, 978-94-007-0165-6. doi:10.1007/978-94-007-0165-6.

[65] Rafael Ferraro and Franco Fiorini. On Born-Infeld Gravity in Weitzenbock spacetime. *Phys. Rev. D*, 78:124019, 2008. doi:10.1103/PhysRevD.78.124019.

[66] Andrew Finch and Jackson Levi Said. Galactic Rotation Dynamics in f(T) gravity. *Eur. Phys. J. C*, 78(7):560, 2018. doi:10.1140/epjc/s10052-018-6028-1.

[67] Daniel Foreman-Mackey, David W Hogg, Dustin Lang, and Jonathan Goodman. emcee: the mcmc hammer. *Publications of the Astronomical Society of the Pacific*, 125(925):306, 2013.

[68] Wendy L. Freedman, Barry F. Madore, Victoria Scowcroft, Chris Burns, Andy Monson, S. Eric Persson, Mark Seibert, and Jane Rigby. CARNEGIE HUBBLE PROGRAM: A MID-INFRARED CALIBRATION OF THE HUBBLE CONSTANT. *The Astrophysical Journal*,

758(1):24, sep 2012. doi:10.1088/0004-637x/758/1/24. URL https://doi.org/10.1088/0004-637x/758/1/24.

[69] Wendy L. Freedman, Barry F. Madore, Taylor Hoyt, In Sung Jang, Rachael Beaton, Myung Gyoon Lee, Andrew Monson, Jill Neeley, and Jeffrey Rich. Calibration of the Tip of the Red Giant Branch (TRGB). 2 2020. doi:10.3847/1538-4357/ab7339.

[70] Alexey Golovnev. The geometrical meaning of the Weitzenböck connection. 2 2023. doi:10.1142/S0219887823502195.

[71] Alan H. Guth. Inflationary universe: A possible solution to the horizon and flatness problems. *Phys. Rev. D*, 23:347–356, Jan 1981. doi:10.1103/PhysRevD.23.347. URL https://link.aps.org/doi/10.1103/PhysRevD.23.347.

[72] Mahmoud Hashim, Waleed El Hanafy, Alexey Golovnev, and Amr A. El-Zant. Toward a concordance teleparallel cosmology. Part I. Background dynamics. *JCAP*, 07:052, 2021a. doi:10.1088/1475-7516/2021/07/052.

[73] Mahmoud Hashim, Amr A. El-Zant, Waleed El Hanafy, and Alexey Golovnev. Toward a concordance teleparallel cosmology. Part II. Linear perturbation. *JCAP*, 07:053, 2021b. doi:10.1088/1475-7516/2021/07/053.

[74] S. R. Hinton. ChainConsumer. *The Journal of Open Source Software*, 1:00045, August 2016. doi:10.21105/joss.00045.

[75] M. P. Hobson. *Bayesian Methods in Cosmology*. Cambridge University Press, 2009.

[76] David W. Hogg. Distance measures in cosmology, 2000.

[77] Manuel Hohmann. Teleparallel gravity. 7 2022.

[78] Caroline D. Huang, Adam G. Riess, Wenlong Yuan, Lucas M. Macri, Nadia L. Zakamska, Stefano Casertano, Patricia A. Whitelock, Samantha L. Hoffmann, Alexei V. Filippenko, and Daniel Scolnic. Hubble Space Telescope Observations of Mira Variables in the Type Ia Supernova Host NGC 1559: An Alternative Candle to Measure the Hubble Constant. 8 2019. doi:10.3847/1538-4357/ab5dbd.

[79] Lorenzo Iorio and Emmanuel N. Saridakis. Solar system constraints on f(T) gravity. *Mon. Not. Roy. Astron. Soc.*, 427:1555, 2012. doi:10.1111/j.1365-2966.2012.21995.x.

[80] Lorenzo Iorio, Ninfa Radicella, and Matteo Luca Ruggiero. Constraining f(T) gravity in the Solar System. *JCAP*, 08:021, 2015. doi:10.1088/1475-7516/2015/08/021.

[81] Mikhail M. Ivanov, Marko Simonović, and Matias Zaldarriaga. Cosmological Parameters from the BOSS Galaxy Power Spectrum. *JCAP*, 05:042, 2020. doi:10.1088/1475-7516/2020/05/042.

[82] G. Jelic-Cizmek et al. Euclid Preparation. TBD. Impact of magnification on spectroscopic galaxy clustering. 11 2023.

[83] Raul Jimenez and Abraham Loeb. Constraining cosmological parameters based on relative galaxy ages. *The Astrophysical Journal*, 573(1):37–42, Jul 2002. ISSN 1538-4357. doi:10.1086/340549. URL http://dx.doi.org/10.1086/340549.

[84] B J T Jones. *Precision cosmology : the first half million years*. Cambridge University Press, 2017.

[85] D Heath Jones, Mike A Read, Will Saunders, Matthew Colless, Tom Jarrett, Quentin A Parker, Anthony P Fairall, Thomas Mauch, Elaine M Sadler, Fred G Watson, et al. The 6df galaxy survey: final redshift release (dr3) and southern large-scale structures. *Monthly Notices of the Royal Astronomical Society*, 399(2):683–698, 2009.

[86] Kimet Jusufi, Salvatore Capozziello, Sebastian Bahamonde, and Mubasher Jamil. Testing Born–Infeld f(T) teleparallel gravity through Sgr A$^\star$ observations. *Eur. Phys. J. C*, 82(11): 1018, 2022. doi:10.1140/epjc/s10052-022-10971-0.

[87] Marc Kamionkowski and Ely D. Kovetz. The Quest for B Modes from Inflationary Gravitational Waves. *Ann. Rev. Astron. Astrophys.*, 54:227–269, 2016. doi:10.1146/annurev-astro-081915-023433.

[88] Daniel Kasen and S. E. Woosley. On the origin of the type ia supernova width-luminosity relation. *The Astrophysical Journal*, 656(2):661, feb 2007. doi:10.1086/510375. URL https://dx.doi.org/10.1086/510375.

[89] Narayan Khadka, Michal Zajaček, Raj Prince, Swayamtrupta Panda, Bożena Czerny, Mary Loli Martínez-Aldama, Vikram Kumar Jaiswal, and Bharat Ratra. Quasar UV/X-ray relation luminosity distances are shorter than reverberation-measured radius–luminosity relation luminosity distances. *Mon. Not. Roy. Astron. Soc.*, 522(1):1247–1264, 2023. doi:10.1093/mnras/stad1040.

[90] Ehsan Kourkchi, R. Brent Tully, Gagandeep S. Anand, Helene M. Courtois, Alexandra Dupuy, James D. Neill, Luca Rizzi, and Mark Seibert. Cosmicflows-4: The Calibration of Optical and Infrared Tully–Fisher Relations. *Astrophys. J.*, 896(1):3, 2020. doi:10.3847/1538-4357/ab901c.

[91] Kevin Krisciunas. The usefulness of type ia supernovae for cosmology - a personal review, 2012.

[92] Ruth Lazkoz, Francisco S. N. Lobo, María Ortiz-Baños, and Vincenzo Salzano. Observational constraints of $f(Q)$ gravity. *Phys. Rev. D*, 100(10):104027, 2019. doi:10.1103/PhysRevD.100.104027.

[93] Antony Lewis. GetDist: a Python package for analysing Monte Carlo samples. 10 2019.

[94] Benjamin L'Huillier and Arman Shafieloo. Model-independent test of the FLRW metric, the flatness of the Universe, and non-local measurement of $H_0 r_\mathrm{d}$. *JCAP*, 01:015, 2017. doi:10.1088/1475-7516/2017/01/015.

[95] Andrew R. Liddle. Statistical methods for cosmological parameter selection and estimation. *Ann. Rev. Nucl. Part. Sci.*, 59:95–114, 2009. doi:10.1146/annurev.nucl.010909.083706.

[96] Eric V. Linder. Einstein's Other Gravity and the Acceleration of the Universe. *Phys. Rev. D*, 81:127301, 2010. doi:10.1103/PhysRevD.81.127301. [Erratum: Phys.Rev.D 82, 109902 (2010)].

[97] Mario Livio and Paolo Mazzali. On the Progenitors of Type Ia Supernovae. *Phys. Rept.*, 736:1–23, 2018. doi:10.1016/j.physrep.2018.02.002.

[98] E. Lusso, E. Piedipalumbo, G. Risaliti, M. Paolillo, S. Bisogni, E. Nardini, and L. Amati. Tension with the flat ΛCDM model from a high-redshift Hubble diagram of supernovae, quasars, and gamma-ray bursts. *Astron. Astrophys.*, 628:L4, 2019. doi:10.1051/0004-6361/201936223.

[99] E. Lusso et al. Quasars as standard candles III. Validation of a new sample for cosmological studies. *Astron. Astrophys.*, 642:A150, 2020. doi:10.1051/0004-6361/202038899.

[100] Juan Magaña, Mario H Amante, Miguel A Garcia-Aspeitia, and V Motta. The cardassian expansion revisited: constraints from updated hubble parameter measurements and type ia supernova data. *Monthly Notices of the Royal Astronomical Society*, 476(1):1036–1049, Feb 2018. ISSN 1365-2966. doi:10.1093/mnras/sty260. URL http://dx.doi.org/10.1093/mnras/sty260.

[101] J. W. Maluf. The teleparallel equivalent of general relativity. *Annalen Phys.*, 525:339–357, 2013. doi:10.1002/andp.201200272.

[102] Sanjay Mandal, Deng Wang, and P. K. Sahoo. Cosmography in $f(Q)$ gravity. *Phys. Rev. D*, 102:124029, 2020. doi:10.1103/PhysRevD.102.124029.

[103] Paola Marziani and Jack W. Sulentic. Highly Accreting Quasars: Sample Definition and Possible Cosmological Implications. *Mon. Not. Roy. Astron. Soc.*, 442(2):1211–1229, 2014. doi:10.1093/mnras/stu951.

[104] Paola Marziani, Deborah Dultzin, Jack W. Sulentic, Ascensión Del Olmo, C. A. Negrete, Mary L. Martínez-Aldama, Mauro D'Onofrio, Edi Bon, Natasa Bon, and Giovanna M. Stirpe. A main sequence for quasars. *Frontiers in Astronomy and Space Sciences*, 5:6, March 2018. doi:10.3389/fspas.2018.00006.

[105] S. Mendoza, X. Hernandez, J. C. Hidalgo, and T. Bernal. A natural approach to extended Newtonian gravity: tests and predictions across astrophysical scales. *Mon. Not. Roy. Astron. Soc.*, 411:226–234, 2011. doi:10.1111/j.1365-2966.2010.17685.x.

[106] M.-L. Menzel, A. Merloni, A. Georgakakis, M. Salvato, E. Aubourg, W. N. Brandt, M. Brusa, J. Buchner, T. Dwelly, K. Nandra, I. Pâris, P. Petitjean, and A. Schwope. A spectroscopic survey of X-ray-selected AGNs in the northern XMM-XXL field. *Monthly Notices of the Royal Astronomical Society*, 457(1):110–132, 01 2016. ISSN 0035-8711. doi:10.1093/mnras/stv2749. URL https://doi.org/10.1093/mnras/stv2749.

[107] Charles W Misner, Kip S Thorne, John Archibald Wheeler, and David I Kaiser. *Gravitation*. Princeton University Press, 2017.

[108] M Moresco, A Cimatti, R Jimenez, L Pozzetti, G Zamorani, M Bolzonella, J Dunlop, F Lamareille, M Mignoli, H Pearce, P Rosati, D Stern, L Verde, E Zucca, C.M Carollo, T Contini, J.-P Kneib, O. Le Fè vre, S.J Lilly, V Mainieri, A Renzini, M Scodeggio, I Balestra, R Gobat, R McLure, S Bardelli, A Bongiorno, K Caputi, O Cucciati, S. de la Torre, L. de Ravel, P Franzetti, B Garilli, A Iovino, P Kampczyk, C Knobel, K Kovač, J.-F. Le Borgne, V. Le Brun, C Maier, R Pelló, Y Peng, E Perez-Montero, V Presotto, J.D Silverman, M Tanaka, L.A.M Tasca, L Tresse, D Vergani, O Almaini, L Barnes, R Bordoloi, E Bradshaw, A Cappi, R Chuter, M Cirasuolo, G Coppa, C Diener, S Foucaud, W Hartley, M Kamionkowski, A.M Koekemoer, C López-Sanjuan, H.J McCracken, P Nair, P Oesch, A Stanford, and N Welikala. Improved constraints on the expansion rate of the universe up to $z \sim 1.1$ from the spectroscopic evolution of cosmic chronometers. *Journal of Cosmology and Astroparticle Physics*, 2012(08):006–006, aug 2012. doi:10.1088/1475-7516/2012/08/006. URL https://doi.org/10.1088%2F1475-7516%2F2012%2F08%2F006.

[109] Michele Moresco, Lucia Pozzetti, Andrea Cimatti, Raul Jimenez, Claudia Maraston, Licia Verde, Daniel Thomas, Annalisa Citro, Rita Tojeiro, and David Wilkinson. A 6% measurement of the Hubble parameter at $z \sim 0.45$: direct evidence of the epoch of cosmic re-acceleration. *JCAP*, 05:014, 2016. doi:10.1088/1475-7516/2016/05/014.

[110] Michele Moresco, Raul Jimenez, Licia Verde, Lucia Pozzetti, Andrea Cimatti, and Annalisa Citro. Setting the Stage for Cosmic Chronometers. I. Assessing the Impact of Young Stellar Populations on Hubble Parameter Measurements. *Astrophys. J.*, 868(2):84, 2018. doi:10.3847/1538-4357/aae829.

[111] Michele Moresco, Raul Jimenez, Licia Verde, Andrea Cimatti, and Lucia Pozzetti. Setting the Stage for Cosmic Chronometers. II. Impact of Stellar Population Synthesis Models Systematics and Full Covariance Matrix. *Astrophys. J.*, 898(1):82, 2020. doi:10.3847/1538-4357/ab9eb0.

[112] Edvard Mortsell, Ariel Goobar, Joel Johansson, and Suhail Dhawan. Sensitivity of the Hubble Constant Determination to Cepheid Calibration. *Astrophys. J.*, 933(2):212, 2022. doi:10.3847/1538-4357/ac756e.

[113] Cristian Zamora Munõz and Celia Escamilla-Rivera. Inverse Cosmography: testing the effectiveness of cosmographic polynomials using machine learning. *JCAP*, 12:007, 2020. doi:10.1088/1475-7516/2020/12/007.

[114] N. Myrzakulov, M. Koussour, Alnadhief H. A. Alfedeel, and E. I. Hassan. Constraining the $f(R,T) = R + 2\lambda T$ cosmological model using recent observational data. 8 2023. doi:10.1088/1674-1137/acf2fa.

[115] José Antonio Nájera, Carlos Aráoz Alvarado, and Celia Escamilla-Rivera. Constraints on f(Q) logarithmic model using gravitational wave standard sirens. *Mon. Not. Roy. Astron. Soc.*, 524(4):5280–5290, 2023. doi:10.1093/mnras/stad2180.

[116] CA Negrete, D Dultzin, Paola Marziani, D Esparza, Jack W Sulentic, A del Olmo, ML Martínez-Aldama, A García López, M D'Onofrio, N Bon, et al. Highly accreting quasars: The sdss low-redshift catalog. *Astronomy & Astrophysics*, 620:A118, 2018.

[117] S. Nesseris, S. Basilakos, E. N. Saridakis, and L. Perivolaropoulos. Viable $f(T)$ models are practically indistinguishable from ΛCDM. *Phys. Rev. D*, 88:103010, 2013. doi:10.1103/PhysRevD.88.103010.

[118] Hagai Netzer. Revisiting the unified model of active galactic nuclei. *Annual Review of Astronomy and Astrophysics*, 53:365–408, 2015.

[119] C. Ngeow and S. Kanbur. The Hubble Constant from Type Ia Supernova Calibrated with the Linear and Non-Linear Cepheid Period-Luminosity Relation. *Astrophys. J. Lett.*, 642: L29–L32, 2006. doi:10.1086/504478.

[120] S. Nojiri, S. D. Odintsov, and V. K. Oikonomou. Modified Gravity Theories on a Nutshell: Inflation, Bounce and Late-time Evolution. *Phys. Rept.*, 692:1–104, 2017. doi:10.1016/j.physrep.2017.06.001.

[121] Rafael C. Nunes. Structure formation in $f(T)$ gravity and a solution for $H_0$ tension. *JCAP*, 05:052, 2018. doi:10.1088/1475-7516/2018/05/052.

[122] P. Padovani et al. Active galactic nuclei: what's in a name? *Astron. Astrophys. Rev.*, 25(1): 2, 2017. doi:10.1007/s00159-017-0102-9.

[123] Shuyang Pan, Miaoxin Liu, Jaime Forero-Romero, Cristiano G. Sabiu, Zhigang Li, Haitao Miao, and Xiao-Dong Li. Cosmological parameter estimation from large-scale structure deep learning. *Sci. China Phys. Mech. Astron.*, 63(11):110412, 2020. doi:10.1007/s11433-020-1586-3.

[124] Isabelle Pâris et al. The Sloan Digital Sky Survey Quasar Catalog: Fourteenth data release. *Astron. Astrophys.*, 613:A51, 2018. doi:10.1051/0004-6361/201732445.

[125] Leandros Perivolaropoulos and Foteini Skara. Challenges for ΛCDM: An update. *New Astron. Rev.*, 95:101659, 2022. doi:10.1016/j.newar.2022.101659.

[126] Bradley M. Peterson. *An Introduction to Active Galactic Nuclei*. Harvard, 1997.

[127] Bradley M. Peterson, Ignaz Wanders, Keith Horne, Stefan Collier, Tal Alexander, Shai Kaspi, and Dan Maoz. On uncertainties in cross-correlation lags and the reality of wavelength-dependent continuum lags in active galactic nuclei. *Publ. Astron. Soc. Pac.*, 110:660, 1998. doi:10.1086/316177.

[128] Oliver H. E. Philcox and Mikhail M. Ivanov. BOSS DR12 full-shape cosmology: ΛCDM constraints from the large-scale galaxy power spectrum and bispectrum monopole. *Phys. Rev. D*, 105(4):043517, 2022. doi:10.1103/PhysRevD.105.043517.

[129] M. M. Phillips. The Absolute Magnitudes of Type IA Supernovae. *Astrophysical Journal Letters*, 413:L105, August 1993. doi:10.1086/186970.

[130] Vivian Poulin, José Luis Bernal, Ely D. Kovetz, and Marc Kamionkowski. Sigma-8 tension is a drag. *Phys. Rev. D*, 107(12):123538, 2023. doi:10.1103/PhysRevD.107.123538.

[131] Sami Raatikainen and Syksy Rasanen. Higgs inflation and teleparallel gravity. *JCAP*, 12: 021, 2019. doi:10.1088/1475-7516/2019/12/021.

[132] Mauricio Reyes and Celia Escamilla-Rivera. On the Degeneracy between f$\sigma_8$ Tension and Its Gaussian Process Forecasting. *Universe*, 8(8):394, 2022. doi:10.3390/universe8080394.

[133] Adam G. Riess and Louise Breuval. The Local Value of $H_0$. 8 2023.

[134] Adam G. Riess, Alexei V. Filippenko, Peter Challis, Alejandro Clocchiatti, Alan Diercks, Peter M. Garnavich, Ron L. Gilliland, Craig J. Hogan, Saurabh Jha, Robert P. Kirshner, and et al. Observational evidence from supernovae for an accelerating universe and a cosmological constant. *The Astronomical Journal*, 116(3):1009–1038, Sep 1998. ISSN 0004-6256. doi:10.1086/300499. URL http://dx.doi.org/10.1086/300499.

[135] Adam G. Riess, Stefano Casertano, Wenlong Yuan, Lucas M. Macri, and Dan Scolnic. Large magellanic cloud cepheid standards provide a 1% foundation for the determination of the hubble constant and stronger evidence for physics beyond $\lambda$cdm. *The Astrophysical Journal*, 876(1):85, May 2019. ISSN 1538-4357. doi:10.3847/1538-4357/ab1422. URL http://dx.doi.org/10.3847/1538-4357/ab1422.

[136] Adam G. Riess, Stefano Casertano, Wenlong Yuan, J. Bradley Bowers, Lucas Macri, Joel C. Zinn, and Dan Scolnic. Cosmic distances calibrated to 1% precision with gaia edr3 parallaxes and hubble space telescope photometry of 75 milky way cepheids confirm tension with $\lambda$cdm. *The Astrophysical Journal*, 908(1):L6, Feb 2021a. ISSN 2041-8213. doi:10.3847/2041-8213/abdbaf. URL http://dx.doi.org/10.3847/2041-8213/abdbaf.

[137] Adam G. Riess, Wenlong Yuan, Lucas M. Macri, Dan Scolnic, Dillon Brout, Stefano Casertano, David O. Jones, Yukei Murakami, Louise Breuval, Thomas G. Brink, Alexei V. Filippenko, Samantha Hoffmann, Saurabh W. Jha, W. D'arcy Kenworthy, John Mackenty, Benjamin E. Stahl, and Weikang Zheng. A comprehensive measurement of the local value of the hubble constant with 1 km/s/mpc uncertainty from the hubble space telescope and the sh0es team, 2021b.

[138] Adam G. Riess, Gagandeep S. Anand, Wenlong Yuan, Stefano Casertano, Andrew Dolphin, Lucas M. Macri, Louise Breuval, Dan Scolnic, Marshall Perrin, and Richard I. Anderson. Crowded No More: The Accuracy of the Hubble Constant Tested with High Resolution Observations of Cepheids by JWST. 7 2023.

[139] Adam G. Riess et al. Milky Way Cepheid Standards for Measuring Cosmic Distances and Application to Gaia DR2: Implications for the Hubble Constant. *Astrophys. J.*, 861(2):126, 2018. doi:10.3847/1538-4357/aac82e.

[140] Adam G. Riess et al. A Comprehensive Measurement of the Local Value of the Hubble Constant with 1 km s$^{-1}$ Mpc$^{-1}$ Uncertainty from the Hubble Space Telescope and the SH0ES Team. *Astrophys. J. Lett.*, 934(1):L7, 2022. doi:10.3847/2041-8213/ac5c5b.

[141] Guido Risaliti, Elisabeta Lusso, Emanuele Nardini, Giada Bargiacchi, Susanna Bisogni, Andrea Sacchi, Matilde Signorini, and Bartolomeo Trefoloni. Quasars as high-redshift standard candles. 4 2023. doi:10.1002/asna.20230054.

[142] Ashley J. Ross, Lado Samushia, Cullan Howlett, Will J. Percival, Angela Burden, and Marc Manera. The clustering of the SDSS DR7 main Galaxy sample – I. A 4 per cent distance measure at $z = 0.15$. *Mon. Not. Roy. Astron. Soc.*, 449(1):835–847, 2015. doi:10.1093/mnras/stv154.

[143] Rodrigo Sandoval-Orozco and Celia Escamilla-Rivera. Cosmological piecewise functions to treat the local Hubble tension. *Eur. Phys. J. Plus*, 137(7):819, 2022. doi:10.1140/epjp/s13360-022-02973-4.

[144] Rodrigo Sandoval-Orozco, Celia Escamilla-Rivera, Rebecca Briffa, and Jackson Levi Said. $f(T)$ cosmology in the regime of quasar observations. 9 2023.

[145] Bernard Schutz. *A First Course in General Relativity*. Cambridge University Press, 2009.

[146] D. M. Scolnic, D. O. Jones, A. Rest, Y. C. Pan, R. Chornock, R. J. Foley, M. E. Huber, R. Kessler, G. Narayan, A. G. Riess, and et al. The complete light-curve sample of spectroscopically confirmed sne ia from pan-starrs1 and cosmological constraints from the combined pantheon sample. *The Astrophysical Journal*, 859(2):101, May 2018. ISSN 1538-4357. doi:10.3847/1538-4357/aab9bb. URL http://dx.doi.org/10.3847/1538-4357/aab9bb.

[147] S. Shankaranarayanan and Joseph P. Johnson. Modified theories of gravity: Why, how and what? *Gen. Rel. Grav.*, 54(5):44, 2022. doi:10.1007/s10714-022-02927-2.

[148] Jiaming Shi. Cosmological constraints in covariant $f(Q)$ gravity with different connections. 7 2023.

[149] Matilde Signorini, Guido Risaliti, Elisabeta Lusso, Emanuele Nardini, Giada Bargiacchi, Andrea Sacchi, and Bartolomeo Trefoloni. Quasars as standard candles - IV. Analysis of the X-ray and UV indicators of the disc-corona relation. *Astron. Astrophys.*, 676:A143, 2023. doi:10.1051/0004-6361/202346104.

[150] Joan Solà Peracaula, Adria Gomez-Valent, Javier de Cruz Pérez, and Cristian Moreno-Pulido. Brans–Dicke Gravity with a Cosmological Constant Smoothes Out ΛCDM Tensions. *Astrophys. J. Lett.*, 886(1):L6, 2019. doi:10.3847/2041-8213/ab53e9.

[151] Jordan Stevens, Hasti Khoraminezhad, and Shun Saito. Constraining the spatial curvature with cosmic expansion history in a cosmological model with a non-standard sound horizon. *JCAP*, 07:046, 2023. doi:10.1088/1475-7516/2023/07/046.

[152] S. H. Suyu et al. H0LiCOW – I. H0 Lenses in COSMOGRAIL's Wellspring: program overview. *Mon. Not. Roy. Astron. Soc.*, 468(3):2590–2604, 2017. doi:10.1093/mnras/stx483.

[153] R. Tripp and D. Branch. Determination of the hubble constant using a two-parameter luminosity correction for type ia supernovae. *Astrophys. J.*, 525:209–214, 1999. doi:10.1086/307883.

[154] Roberto Trotta. Bayesian Methods in Cosmology. 1 2017.

[155] Shinji Tsujikawa. Quintessence: A Review. *Class. Quant. Grav.*, 30:214003, 2013. doi:10.1088/0264-9381/30/21/214003.

[156] Alexander Unzicker and Timothy Case. Translation of einstein's attempt of a unified field theory with teleparallelism. *arXiv preprint physics/0503046*, 2005.

[157] A Vallenari, AGA Brown, and T Prusti. Gaia data release 3. summary of the content and survey properties. *Astronomy & Astrophysics*, 2022.

[158] Deng Wang and David Mota. Can $f(T)$ gravity resolve the $H_0$ tension? *Phys. Rev. D*, 102 (6):063530, 2020. doi:10.1103/PhysRevD.102.063530.

[159] Ke Wang and Qing-Guo Huang. Implications for cosmology from Ground-based Cosmic Microwave Background observations. *JCAP*, 06:045, 2020. doi:10.1088/1475-7516/2020/06/045.

[160] D Watson, KD Denney, Marianne Vestergaard, and Tamara Maree Davis. A new cosmological distance measure using active galactic nuclei. *The Astrophysical Journal Letters*, 740(2):L49, 2011.

[161] N. A. Webb et al. The XMM-Newton serendipitous survey IX. The fourth XMM-Newton serendipitous source catalogue. *Astron. Astrophys.*, 641:A136, 2020. doi:10.1051/0004-6361/201937353.

[162] David H Weinberg, Michael J Mortonson, Daniel J Eisenstein, Christopher Hirata, Adam G Riess, and Eduardo Rozo. Observational probes of cosmic acceleration. *Physics reports*, 530 (2):87–255, 2013.

[163] Steven Weinberg. *Cosmology*. ial xn–3ug : xn–2ug Oxford University Press, Oxford, England, UK, April 2008. ISBN 978-0-19852682-7. URL https://www.amazon.com/-/es/Steven-Weinberg/dp/0198526822.

[164] Maciek Wielgus et al. Monitoring the Morphology of M87* in 2009-2017 with the Event Horizon Telescope. *Astrophys. J.*, 901(1):67, 2020. doi:10.3847/1538-4357/abac0d.

[165] Nahliel Wygoda, Yonatan Elbaz, and Boaz Katz. Type Ia supernovae have two physical width–luminosity relations and they favour sub-Chandrasekhar and direct collision models – I. Bolometric. *Monthly Notices of the Royal Astronomical Society*, 484(3):3941–3950, 01 2019. ISSN 0035-8711. doi:10.1093/mnras/stz145. URL https://doi.org/10.1093/mnras/stz145.

[166] Donald G. York et al. The Sloan Digital Sky Survey: Technical Summary. *Astron. J.*, 120: 1579–1587, 2000. doi:10.1086/301513.

[167] Jian-Chen Zhang, Kang Jiao, and Tong-Jie Zhang. Model-independent measurement of the Hubble Constant and the absolute magnitude of Type Ia Supernovae. *ePrint*, 1 2021.

[168] Xue Zhang and Qing-Guo Huang. Constraints on $H_0$ from WMAP and BAO Measurements. *Commun. Theor. Phys.*, 71(7):826–830, 2019. doi:10.1088/0253-6102/71/7/826.

[169] Gong-Bo Zhao et al. The clustering of the SDSS-IV extended Baryon Oscillation Spectroscopic Survey DR14 quasar sample: a tomographic measurement of cosmic structure growth and expansion rate based on optimal redshift weights. *Mon. Not. Roy. Astron. Soc.*, 482(3): 3497–3513, 2019. doi:10.1093/mnras/sty2845.